

1-1-2013

A Numerical Study Of The Effects Of Overhangs On The Wind-Driven Rain Wetting Of Building Facades

Seyed S. Mohaddes Foroushani
Ryerson University

Follow this and additional works at: <http://digitalcommons.ryerson.ca/dissertations>

 Part of the [Mechanical Engineering Commons](#)

Recommended Citation

Mohaddes Foroushani, Seyed S., "A Numerical Study Of The Effects Of Overhangs On The Wind-Driven Rain Wetting Of Building Facades" (2013). *Theses and dissertations*. Paper 2081.

This Thesis is brought to you for free and open access by Digital Commons @ Ryerson. It has been accepted for inclusion in Theses and dissertations by an authorized administrator of Digital Commons @ Ryerson. For more information, please contact bcameron@ryerson.ca.

A NUMERICAL STUDY OF THE EFFECTS OF OVERHANGS ON THE WIND-DRIVEN RAIN WETTING OF BUILDING FACADES

by

Seyed Sepehr Mohaddes Foroushani

B.Sc., University of Tehran, 2011

A thesis

presented to Ryerson University

in partial fulfillment of the

requirements for the degree of

Master of Applied Science

in the Program of

Mechanical Engineering

Toronto, Ontario, Canada, 2013

© Seyed Sepehr Mohaddes Foroushani 2013

Author's Declaration

I hereby declare that I am the sole author of this thesis. This is a true copy of the thesis, including any required final revisions, as accepted by my examiners.

I authorize Ryerson University to lend this thesis to other institutions or individuals for the purpose of scholarly research.

I further authorize Ryerson University to reproduce this thesis by photocopying or by other means, in total or in part, at the request of other institutions or individuals for the purpose of scholarly research.

I understand that my thesis may be made electronically available to the public.

A NUMERICAL STUDY OF THE EFFECTS OF OVERHANGS ON THE WIND-DRIVEN RAIN WETTING OF BUILDING FACADES

Seyed Sepehr Mohaddes Foroushani

Master of Applied Science, 2013
Mechanical Engineering, Ryerson University

Abstract

Roof overhangs are used traditionally to reduce the amount of rainwater that is deposited on building facades by wind. This thesis investigates the effects of overhangs on the wind-driven rain (WDR) wetting of facades, which have not been studied in detail before, using CFD-based numerical simulation. The commercial CFD package ANSYS FLUENT is used to solve the multiphase flow of wind and rain around buildings. A MATLAB code is developed to post-process the CFD results and calculate the WDR parameters. The numerical scheme is validated by comparison to previously published results and field measurements. Roof overhangs are shown to be effective in protecting facades from WDR, especially at upper parts. This protection is highly dependent upon the overhang size, wind speed, wind direction and the building geometry, but is slightly affected by the rainfall intensity. Physical explanations are presented for the observations and a new global measure of the effectiveness of overhangs is introduced.

Acknowledgements

The author would like to acknowledge his supervisors, Dr. D. Naylor and Dr. H. Ge, gratefully for their invaluable support and continuous guidance during this project that made its successful completion possible.

The author would also like to express appreciation to the financial support from the Natural Sciences and Engineering Research Council of Canada, the NEWBuildS network, FP Innovations and Ryerson University.

Table of Contents

AUTHOR’S DECLARATION.....	ii
ABSTRACT.....	iii
ACKNOWLEDGEMENTS.....	iv
TABLE OF CONTENTS.....	v
LIST OF TABLES.....	viii
LIST OF FIGURES.....	ix
NOMENCLATURE.....	xiii
CHAPTER 1 - Introduction.....	1
1.1. Hygrothermal Analysis of Building Envelopes.....	2
1.2. Wind-Driven Rain.....	4
1.2.1. WDR Parameters.....	5
1.2.2. Experimental Methods.....	7
1.2.3. Semi-Empirical Methods.....	10
1.2.4. Numerical Methods.....	12
1.3. Literature Review of Numerical Simulation of WDR.....	13
1.4. Scope.....	25
CHAPTER 2 - Numerical Simulation of Wind-Driven Rain.....	26
2.1. Particle Laden Turbulence.....	26
2.2. Numerical Simulation of Wind Flow.....	28
2.2.1. Governing Equations.....	28
2.2.2. Modeling Turbulence.....	28
2.2.3. Computational Domain.....	30
2.2.4. Boundary Conditions.....	30
2.2.5. Numerical Solution.....	32
2.3. Numerical Simulation of Rain.....	33

2.3.1. Governing Equations.....	33
2.3.2. Integration Time Step.....	34
2.3.3. Boundary Conditions	35
2.3.4. Raindrop Drag Law.....	36
2.3.5. Raindrop Size Distribution.....	38
2.3.6. Turbulent Dispersion of Raindrops.....	39
2.4. Numerical Simulation of Rain	39
2.4.1. Catch Ratio.....	40
2.4.2. Computational Methods for Area Calculations	41
CHAPTER 3 - Verification, Validation & Accuracy	44
3.1. Verification	44
3.2. Validation	44
3.2.1. Validation of The Numerical Solution of Wind Flow	44
3.2.2. Validation of Catch Ratio Calculations.....	47
3.3. Sources of Error	52
3.3.1. Discretization Error	53
3.3.2. Iterative Convergence Error	57
3.3.3. Modeling Errors.....	57
CHAPTER 4 – Results & Discussion.....	60
4.1. The Cubic Building.....	60
4.1.1. Catch Ratio Contours	62
4.1.2. Effectiveness Index	71
4.1.3. Discussion.....	76
4.2. The Cassier Building.....	90
4.2.1. Catch Ratio Contours	91
4.2.2. Effectiveness Index	93
4.2.3. Discussion.....	96
CHAPTER 5 - Conclusions & Recommendations	100

5.1. Conclusions	100
5.2. Recommendations For Future Work	102
5.2.1. Other Building Geometries.....	102
5.2.2. Pitched Overhangs	103
5.2.3. Transient Wind and Rain.....	103
5.2.4. Different Turbulence Models	103
5.2.5. Eulerian Tracking of the Raindrops	103
5.2.6. The WDR Database and Generalized Integrated Codes.....	104
APPENDIX A - Volume & Mass Fractions of WDR.....	105
APPENDIX B - Number & Location of Particle Injections	
In Discrete Phase Modeling of Rain	108
APPENDIX C - Details of the Validation Study Based on Field Measurements.....	113
REFERENCES	118

List of Tables

4.1	Computational Domain Size & Discretization for the Cubic Building	61
4.2	Summary of Boundary Conditions for the Cubic Building	61
4.3	The Percentage of WDR on Different Parts of the Windward Facade of the Cubic Building with No Overhang	72
4.4	Area-Averaged Catch Ratio Values Without and with the 60 cm Overhang under Different Wind Angles ($U_{10}=5$ m/s, $R_h=5$ mm/Hr)	76
4.5	Computational Domain Size & Discretization for the Cassier Building	90
C1	Hourly Averaged Wind and Rain Data Used in the Validation Study	115
C2	Catch Ratio Values Calculated Based on Field Measurements (Cassier Building)	116
C3	Computational Domain Size & Discretization for the Cassier Building	116

List of Figures

1.1	Rainfall and WDR Gauges	8
2.1	Regimes of Interaction between Particles and the Flow	27
2.2	Schematic of the Computational Domain	30
2.3	Comparison of Different Drag Laws for High Raindrop Reynolds Numbers	37
2.4	Reference and Vertical Wetted Areas	40
2.5	Typical Distribution of Raindrops on A Cell on the Facade	42
2.6	Areas Formed By Extremum Rectangle and Convex Hull Methods	43
3.1	Flow Patterns around Buildings	45
3.2	Side Views of the Wind Velocity Vector Field	46
3.3	Pressure Distribution on the Building Predicted By CFD	47
3.4	Schematic of the Cubic Building	48
3.5	Catch Ratio vs. Rainfall Intensity at Top Corner of the Windward Facade of the Cubic Building ($U_{10}=10$ m/s)	49
3.6	Catch Ratio vs. Rainfall Intensity at the Top Center Point of the Windward Facade of the Cubic Building ($U_{10}=10$ m/s)	50
3.7	Catch Ratio Contours on the Windward Facade	51
3.8	Catch Ratio Values along the South-East Edge of the Cassier Building ($U_{10}=4.5$ m/s, $R_h=2.3$ mm/hr)	52
3.9	Horizontal Velocity Magnitude along a Horizontal and a Vertical Line Upstream of the Cubic Building ($U_{10}=5$ m/s)	54
3.10	Distribution of 1 mm Raindrops near the Centerline of the Windward Facade of the Cubic Building, Calculated at Different Grid Levels ($U_{10}=5$ m/s)	55
3.11	Velocity Magnitude Profile along a Vertical Line on the 45° Plane, 5 m Upstream of the Cassier Building ($U_{10}=5$ m/s)	56
4.1	Schematic of the Cubic Building, Isometric and Top Views	61

4.2	Catch Ratio Contours on the Windward Facade of Cubic Building with Different Overhangs under a Normal Wind ($\theta=0^\circ$, $U_{10}=5$ m/s, $R_h=5$ mm/hr)	65
4.3	Catch Ratio Contours on the Windward Facade of Cubic Building with Different Overhangs under an Oblique Wind ($\theta=45^\circ$, $U_{10}=5$ m/s, $R_h=5$ mm/hr)	66
4.4	Catch Ratio Contours on the Windward Facade under Different Rainfall Intensities, without and with the 60 cm Overhang ($\theta=0^\circ$, $U_{10}=5$ m/s)	67
4.5	Catch Ratio Contours on the Windward Facade under Different Wind Speeds, without and with the 60 cm Overhang ($\theta=0^\circ$, $R_h=5$ mm/hr)	68
4.6A	Catch Ratio Contours on the Windward Facade without and with the 60 cm Overhang under Normal and 30° Winds ($U_{10}=5$ m/s, $R_h=5$ mm/hr)	69
4.6B	Catch Ratio Contours on the Windward Facade without and with the 60 cm Overhang under 45° and 60° Winds ($U_{10}=5$ m/s, $R_h=5$ mm/hr)	70
4.7	Effectiveness Index Calculation Areas on the Windward Facade of the Cubic Building	71
4.8	Effectiveness Index of Different Overhangs over Different Portions of the Windward Facade of the Cubic Building ($\theta=0^\circ$, $U_{10}=5$ m/s & $R_h=5$ mm/hr)	73
4.9	Effectiveness Index of the 60 cm Overhang over Different Portions of the Windward Facade of the Cubic Building under Different Rainfall Intensities ($\theta=0^\circ$, $U_{10}=5$ m/s)	74
4.10	Effectiveness Index of the 60 cm Overhang over Different Portions of the Windward Facade of the Cubic Building under Different Wind Speeds ($\theta=0^\circ$, $R_h=5$ mm/hr)	74
4.11	Effectiveness Index of the 60 cm Overhangs Over Different Portions of the Windward Facade of the Cubic Building under Different Wind Angles ($U_{10}=5$ m/s & $R_h=5$ mm/hr)	75
4.12	Raindrop Trajectories ($\theta=0^\circ$, $U_{10}=5$ m/s)	78
4.13	Distribution of Small and Large Raindrops on the Windward Facade of the Cubic Building without and with the 60 cm Overhang under a Normal Wind ($\theta=0^\circ$, $U_{10}=5$ m/s)	79
4.14	Distribution of Small and Large Raindrops on the Windward Facade of the Cubic Building without and with the 60 cm Overhang under An Oblique Wind ($\theta=45^\circ$, $U_{10}=5$ m/s)	81

4.15	Specific Catch Ratio Contours on the Windward Facade of the Cubic Building without and with the 60 cm Overhang ($\theta=0^\circ$, $U_{10}=5$ m/s)	82
4.16	Distribution of Catch Ratio on the Windward Facade of the Cubic Building without and with the 60 cm Overhang ($\theta=0^\circ$, $U_{10}=5$ m/s, $R_h=5$ mm/hr)	83
4.17	Effects of a 30 cm Overhang on 0.5 mm and 3 mm Raindrops under Normal Wind with Different Speeds	84
4.18	Projected Area beneath the Overhang under High and Low Speed Winds	86
4.19	Distribution of Small and Large Raindrops on the Windward Facade of the Cubic Building without an Overhang under Two Oblique Winds	88
4.20	Schematic of the Cassier Building (Top View)	90
4.21	Catch Ratio Contours on the North Facade of the Cassier Building under Different Rainfall Intensities, without and with the 90 cm Overhang ($\theta=0^\circ$, $U_{10}=5$ m/s)	92
4.22	Catch Ratio Contours on the East Facade of the Cassier Building under Different Rainfall Intensities, without and with the 90 cm Overhang ($\theta=90^\circ$, $U_{10}=5$ m/s)	93
4.23	Effectiveness Index Calculation Areas on the North and East Facades of the Cassier Building	94
4.24	Effectiveness Index of the 90 cm Overhangs Over Different Portions of the North Facade of the Cassier Building under Different Rainfall Intensities ($\theta=0^\circ$, $U_{10}=5$ m/s)	95
4.25	Effectiveness Index of the 90 cm Overhangs Over Different Portions of the East Facade under Different Rainfall Intensities ($\theta=0^\circ$, $U_{10}=5$ m/s)	96
4.26	Distribution of Small and Large Raindrops on the North Facade of the Cassier Building without and with the 90 cm Overhang ($U_{10}=5$ m/s)	97
4.27	Distribution of Small and Large Raindrops on the East Facade of the Cassier Building without and with the 90 cm Overhang ($U_{10}=5$ m/s)	98
B1	Variation of Catch Ratio at the Center of the Cubic Building with Different Numbers of Injected Raindrops ($\theta=0^\circ$, $U_{10}=10$ m/s, $R_h=5$ mm/hr)	109
B2	Specific Catch Ratio ($d=0.5$ mm) Values at Different Locations with 10 cm Perturbation of the Injection Plane in the z-Direction ($\theta=0^\circ$, $U_{10}=10$ m/s)	110

B3	Specific Catch Ratio ($d=3$ mm) Values at Different Locations with 10 cm Perturbation of the Injection Plane in the z -Direction ($\theta=0^\circ$, $U_{10}=10$ m/s)	110
B4	Catch Ratio vs. Rainfall Intensity with 10 cm Perturbation of the Injection Plane in the z -Direction ($\theta=0^\circ$, $U_{10}=10$ m/s)	111
B5	0.5 mm Raindrops in a Cell on the Facade, Injected at Different Spacings	112
C1	The South and East Facades of the Test Building	113
C2	WDR Gauges on the Test Building	113

List of Appendices

A	Volume & Mass Fractions of WDR	105
B	Number & Location of Particle Injections in Discrete Phase Modeling of Rain	108
C	Details of the Validation Study Based on Field Measurements	113

Nomenclature

A_f	Wetted area on the façade [m ²], Raindrop frontal area [m ²]
A_h	Horizontal area [m ²]
C_D	Drag coefficient [-]
C_p	Pressure coefficient [-]
d	Raindrop diameter [mm]
F	Raindrop size cumulative density function [-]
F_D	Drag force [N]
f	Volume-based raindrop size probability density function [1/mm]
f_h	Flux-based raindrop size probability density function [1/mm]
H	Reference height [m]
h	Nominal grid size [m]
K_s	Surface roughness [m]
k	Turbulence kinetic energy [m ² /s ²]
L	Particle tracking length scale [m], Building height [m]
l	Projected height on the façade [m]
OH	Overhang width [cm]
p	Pressure [Pa]
Re_d	Particle Reynolds number [-]
R_h	Horizontal rainfall intensity [mm/hr]
R_{wdr}	WDR intensity [mm/hr]
\vec{r}	Position vector [m]
S_i	Momentum source terms [kg/m ² s ²]
t	Time [s]
U	Horizontal velocity of wind [m/s]
u_{ABL}^*	Friction velocity [m/s]
U_H	Reference wind velocity [m/s]

u_c	Continuum phase (air) velocity [m/s]
u_p	Discrete phase (raindrop) velocity [m/s]
V_t	Terminal velocity of fall of raindrops [m/s]
\forall	Volume [m ³]
x, y, z	Cartesian coordinates [m]
x_i, x_j	Cartesian coordinates [m]
y_0	Aerodynamic roughness length [m]
α	Mass fraction of WDR in air [-]
α_p	Wind profile exponent [-]
γ	Raindrop trajectory angle [°]
δ	Overhang effectiveness index [%]
ε	Turbulence dissipation rate [m ² /s ³]
η	Catch ratio [-]
$\tilde{\eta}$	Partial WDR load [%]
θ	Wind angle [°]
κ	WDR coefficient [-]
κ	Von Karman constant [-]
μ	Air viscosity [N·s/m ²]
ρ	Air density [kg/m ³]
ρ_w	Rainwater density [kg/m ³]
τ_w	Wall friction (shear stress) [N/m ²]
Φ	Volume fraction of WDR in air [-]

CHAPTER 1

Introduction

It was a rash of rainwater leaks in multi-unit residential buildings in Southern British Columbia during the early 90s that drew attention to the failures caused by moisture in buildings in Canada. In 1996, a field survey conducted by the Building Envelope Research Consortium (BERC) confirmed that, rather than moisture from construction or condensation due to air leakage, rain penetration was the main source of moisture leading to building envelope failures [1]. The field survey recognized the major concern to be the poor design details and workmanship, not the material quality or problems in maintenance [2]. One of the important findings of the BERC survey was that the walls facing the prevailing wind direction had more moisture-related problems [1]. Morris [3] has mentioned underestimation of wind-driven rain to be one of the causes of the problems in building envelopes, specifically in the regions with damp coastal weather.

It is noteworthy that, as will be discussed in a following section, wind-driven rain (WDR) studies in Europe were also initiated in the regions with similar climatic conditions. It is now well established that among different sources of moisture deposition on buildings, wind-driven rain is the most critical, especially in climates like the coastal climate of British Columbia, Canada.

The current thesis studies the use of roof overhangs to reduce WDR loads on building facades using numerical simulation. In the mentioned survey [2], the presence and width of roof overhangs have been correlated to few problems. Hazleden and Morris, in their 1999 seminal paper [1], introduced four main strategies for protecting facades from moisture-related damages. One of these strategies has been to try to “deflect” rain so that it fails to hit the wall. Roof overhangs are introduced as the primary rain deflectors.

The study of WDR, and its impact on buildings, comprises quantification of the WDR loads on facades and evaluation of the response of building envelopes to such loads. Due to the acknowledged importance of WDR in the durability evaluation of building facades and the proper design of envelopes, there have been quite a number of studies aiming at quantifying

WDR loads on building facades. However, it remains a difficult task to predict the distribution of WDR deposition on buildings accurately, especially with the consideration of design details such as overhangs.

Overhangs have been traditionally used in building design for purposes including protection against rain. Nonetheless, the protective effect of roof overhangs against wind-driven rain wetting of building facades and its relation with the overhang configuration (sizing and geometry) are not clear to the designer. Consequently, design practice has been generally based on rule-of-thumb and governed by the architectural expression. It is the objective of the present work to provide insight into the effectiveness of overhangs under different wind and rain conditions.

In this opening chapter, the hygrothermal analysis of building envelopes and its important in design is briefly introduced. Then, wind-driven rain, the main subject of this thesis, is introduced and different parameters used in the literature are defined. Different methods of studying WDR are then briefly discussed, followed by a literature review of numerical studies of WDR. The scope of the thesis is defined in the end of this chapter.

1.1. Hygrothermal Analysis of Building Envelopes

Nowadays, buildings are designed based on three main criteria, namely, health and safety of the inhabitants, energy efficiency and minimization of the environmental impacts [4]. Moisture transport through the envelope, in addition to the durability, indoor air quality and health and safety conditions, influences the energy efficiency of the envelope system too. Hygrothermal analysis, which involves the study of simultaneous heat and mass (air and water vapour) transfer through the building envelope, should be an essential part of any sustainable design that intends to meet the mentioned criteria. The many moisture-related failures of wood-frame construction in low-rise and steel-frame construction in high-rise buildings have pronounced the importance of the hygrothermal assessment of designs [5].

Utilization of different mathematical models to simulate the structural performance of the building, as well as its mechanical systems, is well established in the building industry. These models are used to analyze the performance of a system and its *subsystems* and then improve,

adjust, optimize or revise them until a design criterion is met. The building industry has started a similar approach to building enclosures [6]. The rapid changes in materials and interior building environments, together with the growth in performance expectations for both the enclosure and the building, call for development and use of practical hygrothermal analysis methods [6]. Hygrothermal analysis is usually performed to provide sufficient and appropriate information needed for [6]

- i.* understanding the enclosure response, *e.g.* whether or not condensation occurs within the envelope,
- ii.* identification of possible performance problems, *e.g.* excessive condensation, and
- iii.* quantification of heat transfer through the enclosure.

Historically, the first attempts were aimed at predicting the hygrothermal performance of individual building envelope elements, *e.g.* a curtain wall, by *uncoupling* the system not only from the interior environment, but also from the interactions of the other components with both the exterior and interior environments. Such “stand-alone” analysis of particular components has been helpful in understanding the influences of various controlling elements (vapour retarders, air barriers, building papers, etc.). However, this approach provides limited information on the overall performance of the building in terms of heat and mass transfer. Currently, durability of the building envelope is assessed using experimental and modeling techniques to predict its long-term performance under different conditions of interior and exterior loading. It is by means of this approach that comparison and ranking of wall systems based on overall hygrothermal performance is made possible [5]. Reference [6] provides a summary of various HAM (Heat, Air and Moisture transfer) analysis models that are commonly used.

As pointed out by Straube and Burnett [6], prediction of the moisture and temperature conditions inside building enclosures may turn out to be difficult mainly due to the amount of information that is usually required to analyze the hygrothermal performance of the building enclosure. For a hygrothermal performance analysis to be performed, knowledge about geometry of the enclosure (including all details), the boundary conditions, material properties (and their dependence upon temperature, moisture content, and age) and physics of combined heat, air, and moisture transport is required. WDR studies, including the present work, provide moisture boundary conditions for HAM analysis of building envelopes.

1.2. Wind-Driven Rain

The co-occurrence of wind and rain causes wind-driven rain (WDR). Wind-driven rain, also referred to as driving rain, is defined as the rain that is given a horizontal velocity component by the wind and thus, in combination with the influence of gravity, falls obliquely [7]. WDR research is important in various research areas including earth sciences, meteorology and building science. In particular, and from the building science point of view, WDR is of importance, as it is known to be the most critical source of moisture deposition on buildings, especially in climates like the coastal climate of British Columbia, Canada. Its destructive impacts on the building envelope appear in different forms such as moisture accumulation in porous materials that can lead to water penetration, moisture induced salt migration, discoloration by efflorescence, structural cracking due to thermal and moisture content gradients, and WDR impact and runoff, which are responsible for surface soiling on facades.

As pointed out by Blocken and Carmeliet [7], there are two major reasons for the persistence of the problems associated with WDR wetting of building facades. First, the growing trend of innovations in design features, building technologies and materials, while there is still a gap in the knowledge of their hygrothermal performance. Second, the lack of appropriate quantitative data for design against WDR. The large number of parameters influencing WDR loads on the building facade (building geometry, wind speed and direction, the highly turbulent behaviour of wind, rainfall intensity, raindrop size distribution, topology, etc.) makes the quantification of WDR a complicated problem. Therefore, and despite almost a century of research efforts [7], there is still a lot to be done.

WDR research consists of quantifying rain loads on building facades and consequently investigating the hygrothermal response of the envelope. For the former, which will be the focus of this work, different approaches are used, namely, measurement, semi-empirical methods and numerical simulation based on Computational Fluid Dynamics (CFD).

The first attempts in the estimation of WDR on buildings were based on measured wind flow patterns [8]. So far, measurements have been the primary tool in quantifying WDR [8]. However, according to Blocken [8], establishment of a systematic experimental approach in WDR quantification does not seem feasible. Some of the key problems with WDR measurements are

that they can easily suffer from large errors [9], that they are time-consuming and expensive, and that measurements on a particular building site would have very restricted application in other cases. These limitations motivated researchers to establish semi-empirical relationships between the quantity of WDR and the influencing climatic parameters generally available. The advantage of semi-empirical methods is their ease of use, while their main disadvantage is that they only provide rough estimations of the WDR exposure. The calculations using empirical correlations, usually involving the wind speed, the wind direction and the horizontal rainfall intensity, are only a relative indicator of the potential wind-driven rain loads on facades. The actual WDR loads on the surface are largely influenced by the building geometry and design details such as roof overhangs. The drawbacks of measurements and semi-empirical methods, together with the vast developments in CFD techniques and the computational power available to the engineer, have led the researchers to using CFD modeling for quantification of WDR loads. The introduction of CFD in WDR research, during the past twenty years, has opened new horizons in this area. A brief review of the research efforts on numerical modeling of WDR is presented in section 1.3.

1.2.1. WDR Parameters

In this section, some of the parameters and concepts that are most frequently referred to in the WDR literature are introduced.

Rain

The technical definition of rain is particulate liquid water that is formed within a cloud and falls towards the ground [10].

Rainfall Intensity

Rainfall intensity or the intensity of rainfall is defined as the total volume of rain (rainfall depth) falling during a given period to the duration of the period. Rainfall intensity is expressed in depth units per unit time, usually as millimeters per hour.

Raindrop Diameter

Raindrops do not have regular shapes¹. Therefore, the term “diameter” refers to a *nominal* size measure being equal to the diameter of a sphere with the same volume as the raindrop.

Catch Ratio

Catch ratio is defined as the ratio of the wind-driven rain intensity on vertical surfaces (R_{wdr}) to the horizontal rainfall intensity (R_{h}) [10]

$$\eta = \frac{R_{\text{wdr}}}{R_{\text{h}}} \quad (1.1)$$

Driving Rain Index

Driving Rain Index (DRI), originally proposed by Lacy [11], is defined as the product of the mean annual wind speed and the mean annual rainfall in units of area per time. Whether this is a good measure of WDR loads on the building has been a matter of controversy in the literature. For instance, reference [12] criticizes this parameter as giving no information about the occurrence of wind and rain simultaneously.

Driving Rain Factor

Driving Rain Factor (DRF) is defined based on the relation proposed by Straube [13]

$$R_{\text{wdr}} = \text{DRF} \cdot U(y) \cdot R_{\text{h}} \quad (1.2)$$

where R_{wdr} and R_{h} are the WDR and horizontal rainfall intensities respectively and $U(y)$ is the velocity of wind at some elevation y above the ground. It is shown in reference [13] that RDF is the reciprocal of the raindrops terminal velocity of fall,

$$\text{RDF} = \frac{1}{V_t(d)} \quad (1.3)$$

¹ See section 2.3.4 for more details.

Rain Admittance Factor

Rain Admittance Factor (RAF) is introduced to convert the WDR intensity on the LHS of Eq. (1.2), which is the *free-field* intensity, to the WDR intensity *on the building facade*. Values of RAF are provided in graphical form for different building geometries based on WDR measurements.

WDR Coefficient

The WDR coefficient is an empirical factor used to calculate the WDR intensity based on the wind speed and horizontal rainfall intensity. Definition of the WDR coefficient and a brief discussion of its application in WDR research can be found in section 1.2.3.

1.2.2. Experimental Methods

The experimental study of WDR can be divided into the two general categories of field measurements using WDR gauges and wind tunnel measurement. Recently, a laser-based technique for field measurements of WDR has also been introduced [13].

WDR Gauges

The primary means of measuring WDR is the WDR gauge. As opposed to rain gauges that have a horizontal aperture to measure the rainfall, WDR gauges have vertical openings. Figure 1.1 shows schematics of rainfall and WDR gauges. These gauges have originally been used in earth sciences and meteorology, and not for building research. Measurements of WDR using such gauges date back to 1816. The first WDR gauges designed particularly for building research were introduced in 1936 by Beckett at the Building Research Station (BRS) in the UK and in 1937 by Holmgren at the Norwegian Building Research Institute (NBRI).² The gauge employed by Holmgren in 1937 in Trondheim, Norway is recognized as probably the first WDR gauge for measurements on buildings [7]. The historical trend and design features of these gauges are extensively examined in detail in references [7] and [10]. In the same references, the accuracy of measured WDR data has also been discussed. Based on the body of experimental studies of

² As pointed out by Blocken, it is not surprising that the bulk of WDR research is situated in Norway and the UK, where there are long coastlines compared to the land area and many buildings are affected by the oceanic climate and serious WDR exposure.

WDR, it can be concluded that, in general, the intensity of free (*undisturbed* or *unobstructed*) WDR increases with wind speed and horizontal rainfall intensity proportionally [7].

Measurements by *wall-mounted* gauges have led to what is today known as the *classic wetting pattern* of facades. Based on this pattern, the windward facade is wetted, while the other facades remain almost dry. On the windward facade, the wetting is increased from bottom to top and from the center to the sides. The top corners are usually most wetted, followed by the top and side edges. For high and wide buildings, most of the windward facade will catch little WDR, except for the corners, and the top and side edges. Finally, the amount of WDR at a fixed position is proportional to the wind speed and the horizontal rainfall intensity.

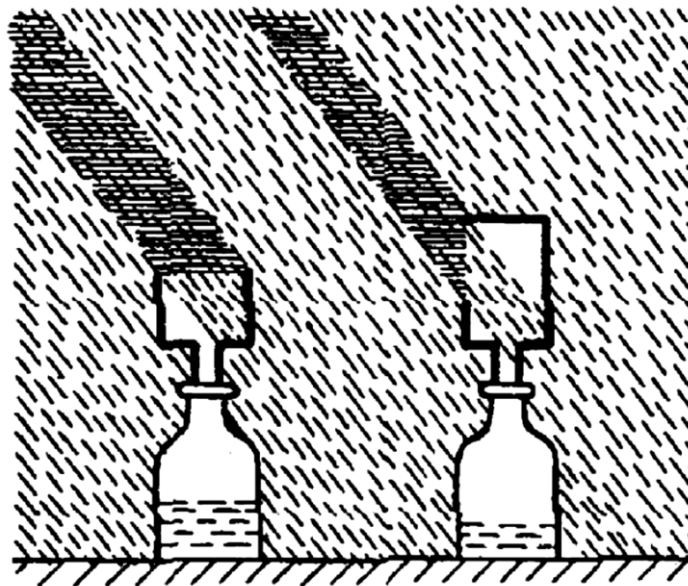


FIGURE 1.1 - RAINFALL (LEFT) AND WDR (RIGHT) GAUGES [10]

Wind Tunnel Measurements

Wind tunnel modeling of WDR has been considered by Flower and Lawson as early as in 1972 [14] and by Rayment and Hilton in 1977 [15]. Surry and Inculet [16] have pointed out the difficulties associated with wind tunnel modeling WDR. They have discussed that the main problem is simulating the actual rain event since there are well developed standard techniques for reproducing the “natural wind characteristics.” The other important problem has been determining the amount of WDR deposition on the model building. For this purpose, special techniques such as the *electrostatic-sensor* technique or the *water-sensitive paper* method are

used. In the former, droplets are initially charged with a very small electrostatic charge and the building is instrumented with sensors that would measure the transferred electrical charges. Based on the charge-to-mass ratio and the charge collected, the quantity of water, which impinges on the building surface, will be calculable as a function of time. The droplet charges used are too small to affect the trajectories of the droplets. However, as Surry and Inculet have pointed out, the charge on a particle is not proportional to the mass of the particle and hence this technique is most applicable to the cases where all the drops are of the same size. In their 1994 paper, they have also questioned the possibility of determining wetting patterns through “superimposing consecutive experiments” in which different drop sizes or driving rain angles are simulated.

Surry and Inculet [16] have used water-sensitive paper, which changes colour immediately upon contact with water. Each raindrop falling on the paper leaves a stain and, hence, a visualization of the wetting pattern is possible. By counting and sizing the stains, an estimation of the WDR deposition on different parts of the facade was made. Surry and Inculet managed to reproduce the “classical” wetting pattern of building facades. They reported the major drawbacks of this method to be the very limited time of the rain shower (as the water drops need to be distinguishable on the paper) and the fact that counting and sizing the stains are very cumbersome and not possible for all locations or for a large number of tests. They have also noted that the short period of the experiments (5-10 s) might lead to a significant variability from test to test, thus a low reliability of the results.

As Blocken and Carmeliet have mentioned in their 2004 review paper [7], although the accuracy of wind tunnel experiments had been expected to be higher than field measurements, the wind tunnel experiments, such as the one by Inculet and Surry, are an indication that this may not be necessarily true. They have also pointed out that wind tunnel work is labour intensive and expensive and it seems no less demanding than field measurements [7].

Concluding their review of WDR research, Blocken and Carmeliet [7] state that the methods for field measurement of WDR in building science have remained practically unchanged since the first measurements were made in the 1930s and that a systematic experimental approach for assessment of WDR does not seem feasible. Nonetheless, they also state that, despite all of the

drawbacks, experimental studies are vital in gaining knowledge on the interaction between WDR and buildings. Experimental studies are a basis for the development and validation of semi-empirical methods and for the validation of numerical methods.

1.2.3. Semi-empirical Methods

The fact that WDR is not among the standard meteorological data measured and reported at weather stations drove researchers to seek relationships between the quantity of WDR and the reported climatic parameters such as wind speed, wind direction and horizontal rainfall intensity. These relations are considered “semi-empirical” as they have theoretical bases as well as free parameters, which are chosen to fit experimental data. According to reference [7], all existing semi-empirical methods are based on one of the two approaches initiated by Hoppestad in 1955 [7,17]; the WDR index and the WDR relationship. These approaches are briefly described in the following section.

Semi-empirical methods can be used to make rough estimations of WDR loads on buildings. Such estimates may be sufficient in some cases, but are not capable of providing detailed information such as the complete WDR distribution on buildings or the effects of building details such as roof overhangs. In such cases, one has to resort to numerical methods [7].

The Wind-Driven Rain Index

The concept of WDR index stemmed from the observation that the amount of WDR seemed to be proportional to the product of wind speed and horizontal rainfall. WDR maps were constructed based on calculating this product for different places throughout a country. The first WDR map was prepared for Norway, by Hoppestad in 1955 [7,17], based on WDR measurements using WDR gauges and the standard meteorological data. The WDR index approach and efforts for developing new WDR maps were followed by various researchers. However, this approach turned out to be insufficient for a number of European countries as, in many cases, it underestimated the actual WDR exposure. This has been attributed to the fact that the WDR index was obtained using wind speed values that were averaged over periods both with and without rain, rather than averaging during rain only. Other deficiencies are also noted for this approach: that long time averages (annual wind and rain data) are used and that the WDR index

was a long-term index, that WDR index is a good measure for long-term events such as moisture accumulation in porous materials, but not for short-term events such as penetration through windows and curtain walls. And, that the WDR index relates to the free WDR and does take into account local phenomena such as topography and the building geometry.

Based on various studies, significant corrections have been made in the WDR index approach. The use of hourly wind and rain data in calculating the indices, the introduction of a spell index alongside the average annual index to represent short time events and the introduction of four empirical factors to take into account the effects of terrain roughness, local topography, obstructions and building geometry are among these corrections. Hence, the WDR index method, over the years, has evolved from a qualitative to a quantitative approach [7].

The Wind-Driven Rain Relationship

The WDR relationship is based on the assumption that all raindrops are of the same size and that the wind flow is uniform, steady and horizontal. Therefore, the intensity of WDR passing through an imaginary vertical surface will be

$$R_{\text{wdr}} = R_h \frac{U}{V_t} \quad (1.4)$$

where R_{wdr} is the WDR intensity, R_h is the horizontal rainfall intensity, U is the wind speed and V_t is the terminal velocity of raindrops. In Eq. (1.4), it is assumed that the wind direction stays normal to the vertical surface.

Hoppestad [17] proposed the following formula based on Eq. (1.8):

$$R_{\text{wdr}} = \kappa \cdot U \cdot R_h \quad (1.5)$$

which is known as the *WDR relationship*, with the factor κ known as the *WDR coefficient*. Average values of κ have been calculated based on measurements with WDR gauges.

Lacy [11] refined Eq. (1.5) using the empirical relationships for the median raindrop size as a function of horizontal rainfall intensity and the raindrops terminal velocity of fall, leading to

$$R_{\text{wdr}} \approx 0.222 \cdot U \cdot R_h \quad (1.6)$$

where the value of 0.222 (s/m) for κ results from the adopted empirical relationships. As reported in reference [7], several researchers have found good agreement between the results calculated with Eq. (1.6) and their measurements of free field WDR.

Equation (1.6) gives the amount of WDR passing through a vertical surface in an undisturbed stream of wind. And so, local phenomena induced by the topography and by the presence of the building are not taken into account. The flow pattern of wind around the building causes deflection of the raindrop trajectories. The amount of WDR on buildings may consequently differ from the free WDR. Using an *adapted* WDR coefficient local effects were taken into account

$$R_{\text{wdr}} \approx \kappa \cdot U \cdot R_h \cdot \cos\theta \quad (1.7)$$

where θ is the angle between the wind direction and the line normal to the wall. This equation is the WDR relationship for WDR on buildings.

Reference [7] recognizes the determination of the adapted WDR coefficient as the weakness of this method since this single value is supposed to take the entire complexity of the interaction between WDR and the building into account. It is also mentioned in the same reference that the “appropriate value” for κ should be used to assess WDR deposition on buildings using Eq. (1.7).

Numerical Methods

As mentioned previously, with “the inherent complexity” of the problem of WDR being revealed by experimental and semi-empirical methods, and with the drawbacks and limitations of such methods, researchers started use to numerical methods to investigate WDR [7].

From the fluid mechanics point of view, the problem of WDR is a multiphase flow of wind and rain around the building. In general, the continuity, Navier-Stokes and conservation of energy equations will be fully describing the system, and the set of coupled PDEs obtained from

applying these laws to each phase could be (numerically) solved to obtain the trajectories of the raindrops and, accordingly, their distribution on the building facade.

However, solving the full Navier-Stokes equations in their transient form for both wind and rain requires considerable computational resources, is time-consuming and does not seem very practical. Moreover, the highly turbulent nature of wind and the stochastic characteristic of rain add to the complexity of the problem, let alone the sophisticated interaction between WDR and buildings. Simplifying assumptions have helped reduce the complexity of the problem and made the numerical simulation of WDR possible. Numerical models, by allowing detailed and high-resolution quantification of WDR both spatially and temporally, have significantly contributed to the present understanding of the interaction between wind, rain and buildings [7].

On the other hand, the numerical method has its own drawbacks, among which are the very large amount of preparation work (pre-processing) they require, the need for high computational performance and long calculation times [7]. However, with the increasing capacities of the computers used in research labs, such limitations do not seem to persist any longer.

Accuracy requirements, such as the choice of the turbulence model, the spatial resolution of the computational grid, accuracy and the time resolution of the meteorological input data, must also be very carefully examined when using numerical models for simulating WDR. As for the future of the numerical research in WDR, it is anticipated that the semi-empirical and the numerical approaches would merge into a joint quantification method [7]. Such a “hybrid” approach is expected to lead to a “WDR exposure database” where WDR coefficients for the easy-to-use semi-empirical correlations are accurately calculated based on a large number of numerical simulations [7].

A historical review of research on numerical simulation of WDR is presented in the next section.

1.3. Literature Review of Numerical Simulation of WDR

Numerical techniques have been used to predict the trajectories of raindrops since the early 1970s. A good example is the work of Rodgers *et al.* in 1974 [18], wherein a set of data from wind tunnel measurements on a scale model was used to calculate the trajectories of raindrops with different diameters. A numerical procedure for calculating raindrop impact rates on a “slab

type” building has been proposed in this work. An approximate analytical formula is presented to predict the effects of the aspect ratio on deposition rates.

However, it was not until 1979 that Computational Fluid Dynamics (CFD) were introduced to research on WDR [7]. In 2004, Blocken and Carmeliet [7] made a comprehensive review of wind-driven rain research in building science, providing a historical overview of the development of numerical simulation of WDR, as well as other methods.

The bulk of numerical research on WDR has been conducted in the past twenty years [7], starting with the pioneering work of Choi in 1991 [19]. He developed a numerical method in which the raindrop trajectories were calculated based on a steady state solution of the wind flow around the building. This technique has been the basis of many studies including the current thesis. In Choi’s method, the flow pattern is obtained by solving the Reynolds-Averaged Navier-Stokes (RANS) equations, the continuity equation and the equations of the standard k - ϵ turbulence model. This technique allows the determination of the spatial distribution of WDR on buildings under steady state conditions of wind and rain, *i.e.* for fixed wind speed, wind direction and horizontal rainfall intensity. In his 1993 paper [20], where WDR on rectangular buildings with a variety of aspect ratios was investigated, Choi reported that raindrop trajectories to be strongly dependent on the size of the droplet. The amount of rainwater hitting the front face is also reported to be strongly influenced by the wind speed and highly dependent on the location on the façade. The upper quarter of the windward facade would receive much more rain than the sum of the remaining three quarters. These observations are now known as the “classical” wetting pattern, widely used in the benchmark studies. This classical pattern has been reproduced by the present study as well.

In 1994, Choi further developed his model to a “systematic method” through which the amount of rain falling on the building faces could be computed for different “return periods” [21]. This method was made possible by integrating the probability calculations corresponding to the occurrence of wind and rain at the same time based on meteorological records into the CFD-based procedure he had previously developed for the computation of raindrop trajectories.

Choi performed the first numerical study of the effects of *gusts* on WDR deposition on buildings in 1997 [22]. In order to do this, he used random numbers to generate the fluctuating component

of the wind velocity. Special considerations were made to take care of both small- and the large-scale gusts. The effects of gusts on the mean intensity of WDR on the windward facade are found to be insignificant. The effect of random turbulence is shown to be small, whereas the larger gust, which was claimed to be a better representation of the actual situation, has had a greater influence. This work, in essence, completed the author's earlier work which used the mean flow conditions and thus could yield the mean wind-driven rain patterns only.

Later in 1999 [23], based on the method he had presented in 1994, Choi proposed simplified expressions which involved single parametric values pertaining to the averaged conditions and were applicable to practical problems. Based on the results, Choi has concluded Driving Rain Index (DRI) is a good indicator of the overall WDR wetting. He also has highlighted that either the full CFD simulation or these simplified equations must replace "the guess work" by designers for determination of the wind-driven wetting patterns of facades.

Hangan, in 1999 [24], introduced a CFD methodology to reproduce the previously developed wind tunnel experiments. Explaining the motivation behind this work, he has argued that many components of the methodology already existed, but they had never been brought together in a proper form for general applications. He used the commercial CFD package FLUENT to solve the wind flow field around the building, Then, the trajectories of raindrops were calculated using Lagrangian particle tracking. The volumetric fraction of water in air being low and the particle-particle interactions being negligible were the fundamental assumptions made in this work. The same CFD software and the same fundamental assumptions are used in the present study. The numerical work of Hangan has reproduced an earlier wind tunnel experiment closely. Examining both $k-\epsilon$ and RSM turbulence models in his numerical solution, the author has reported the same general flow patterns around buildings as described in reference [25]. Stokes law is used to compute the drag force on the raindrops in this work. The use of this law is based on the assumption of spherical shape for the droplets, which is highly questionable. Turbulent dispersion is also taken into consideration in this work using the *instantaneous* velocity of wind in the Lagrangian equation of motion of the raindrops, which may be also put into question as the wind flow has been solved under steady state conditions. As an application of the developed method, Hangan has also investigated the effectiveness of a cornice design in reducing the rain impact rate on the upper part of the facade of a low-rise building, by comparing results of the

simulations without and with the cornice. He has reported a “positive effect” for the cornice over a great majority of the building zones. Nevertheless, the sizing and other details of the cornice are not given.

In 2000, Blocken and Carmeliet [26] extended Choi’s method by adding the temporal component and developing a new data averaging technique, allowing the determination of the temporal (in addition to the spatial) distribution of WDR based on climatic data generally available. They emphasized, in this work, the importance of validation. Following that, Blocken and Carmeliet published a paper on collecting representative experimental data for estimating WDR exposure [27], where they have discussed different issues of the experimental studies intended for validation of numerical simulations, including time-averaging techniques. Their experiments showed the capability of their presented numerical method in estimating WDR loads on building envelopes accurately.

In 2001, Choi studied wind-driven rain during thunderstorms and non-thunderstorms [28]. He has investigated the variation of the wind-driven rain intensity with the averaging period and concluded the short duration intensity can be up to 20 times larger than the hourly average. His study of the WDR intensity coefficient indicates that the coefficient calculated based on raindrop size distribution can be significantly underestimating at low altitudes close to the ground. The actual coefficient was shown to be 1.5-2.2 times this “ideal” value. This discrepancy has been attributed to the large slip velocity of the raindrops with respect to air, due to the sharp gradient of wind speed near the ground. He has thus concluded that the commonly accepted assumption that the horizontal velocity of the raindrop is equal to the wind speed ceases to be valid close to the ground.

In 2002, Blocken and Carmeliet applied their extension of Choi’s technique to a low-rise building of complex geometry under a few onsite recorded rain events [29]. They have also verified their numerical method in both space and time by a full-scale experiment to show how well the numerical method performs in real-life situations. This validation study is crucial to the present work, as the current simulations are validated against one of the numerical simulations presented in the mentioned work. As related to the subject of the present study, the authors have mentioned that, for fixed wind speed and raindrop diameter, the shelter effect of the roof overhang increases as the overhang width increases. The shelter provided by the overhang has

been shown to decrease as wind speed increase since the trajectories would be more inclined and the sweeping effect becomes more important. A decreased shelter against smaller raindrops has also been reported, but the effect of the raindrops size has been less pronounced than the influence of wind speed. As will be discussed in Chapter 4, similar conclusions can be made in general from the results of the current study.

In their 2005 paper [30], Blocken and Carmeliet have pointed out the very few efforts in the validation of CFD for calculating the amount of WDR falling onto building facades. However, in the same paper, which contains new validation efforts, the conclusion has been drawn that “satisfactory agreement” is possible to achieve between the experimental and numerical results. They have pointed out the simplification of the upstream wind conditions to be the main reason of the observed discrepancies.

Later, in 2006, Blocken and Carmeliet published a paper on validity of the “cosine projection method” for WDR calculations under oblique winds [31]. The idea behind this method is that the WDR deposited on the facade by any oblique wind can be computed by multiplying the WDR intensity under a normal wind with the same speed by the cosine of the wind angle. This method, although generally accepted and widely used, had not been validated. The authors have also mentioned the “temptation” of applying the cosine projection to reduce the computational expense of numerical simulations. However, their numerical tests on a low-rise cubic building have revealed that the cosine projection to be not strictly valid, leading to significant errors. They have also argued that, since the complexity of the WDR distribution patterns is expected to increase for complex geometries, the failure of the cosine projection will be likely even more pronounced. The authors have made the concluding remark that, even for a simple cubic building, development of improved simplified models for oblique winds might turn out to be an “impossible task” and CFD-based numerical simulation might be the only option. Oblique winds are studied in the present thesis as well and the results confirm the invalidity of the cosine projection.

In 2007, Blocken and Carmeliet [32] used a high-resolution set of experimental data from a measurement set-up specifically designed for CFD validation studies and performed a detailed validation study on a low-rise building under a number of very different rain events. This work

has shown CFD-based simulations to be able to provide quite accurate predictions of WDR deposition on the building facade. Like in their earlier works [25,26], they attributed the discrepancy between their numerical simulation and the experiments to the simplification of the upstream terrain.

In 2008, Abadie and Mendes [33], tried to address the effects of turbulence modeling on the distribution of WDR catch ratio on the windward facade of an isolated rectangular building. The simulation is performed for an isolated rectangular building and the authors have looked at the effect of turbulence on the specific catch ratio for a single droplet diameter and under fixed wind speed and angle only. Most notably, they have shown turbulence to have a negligible effect on the WDR wetting of the entire windward wall, but substantial influence on the local values of specific catch ratio. Based on studies like this, the relatively simple and computationally less expensive k- ϵ model has been used to model turbulence in the current work.

Abuku *et al.*, in 2009 [34], studied WDR on a simple rectangular low-rise test building subject to various oblique winds as they had found the previous efforts addressing wind directions normal to the facade or on buildings with complex geometry only. The CFD solution has been validated by comparing the results with those of full-scale measurements. Despite a satisfactory agreement between experimental and numerical results, significant discrepancies have been reported near the roof overhang and near the downwind edge of the facade. These discrepancies have been attributed to the inaccuracies in the numerical model resulting from very small impact angles of the raindrops at those facade positions. This, in turn, stems from the fact that the specific catch ratio is determined based on the configuration of raindrop trajectories and their intersection with the plane of the facade. Accordingly, as the angle between the trajectory and the facade decreases, the determination of the point of intersection loses accuracy. Moreover, the authors have argued that although, in the WDR literature, turbulent dispersion had been considered less important for low-rise buildings and normal wind directions, it might be significant for oblique winds. Having these conclusions in mind, oblique winds with angles up to 60° are investigated in the present study.

In the same year, Abuku *et al.* [35] examined the “traditional” approach to the implementation of WDR loads in numerical HAM analyses, in which the total rainwater is applied as an average

mass flux calculated from all the raindrops during the time interval of the meteorological input data and averaged spatially and temporally. They measured the WDR intensity, relevant environmental conditions and the resulting moisture response of the wall on a test building, and compared the data to the results of numerical simulations based on the traditional approach. They showed that the numerical simulations to overestimate the average moisture content of the specimen significantly. This overestimation has been attributed to the error from splashing and bouncing of the raindrops (which is ignored in the traditional averaging technique) and the errors associated with averaging the data. Questioning the traditional approach and pointing out the possible sources of error, the authors have concluded that an accurate and reliable numerical HAM simulation of the response of walls to impinging WDR is a very difficult task and further investigation of the topic is required. In spite of the errors that stem from neglecting the surface phenomena such as splashing still not fully known and to save time and computational effort, and to focus on the effects of overhangs, this thesis does not treat the rain-facade interaction. As in many other studies, WDR is simulated until it hits a solid boundary. After that, the particle is removed from the domain. The interaction between the wind-driven raindrops and the facade is important from both fundamental and practical perspectives and needs to be examined in more depth in the future.

Blocken *et al.*, in 2009 [36], published a high-resolution CFD simulation of convective heat transfer from the facade of a low-rise building. In this work, a comparison has been made between the distributions of heat transfer coefficient and catch ratio on the facade. It has been shown that there is a strong similarity in the spatial distributions of the two, with both heat transfer coefficient and catch ratio increasing from bottom to top, and from the center to the sides, with maxima at the top edge and top corners. It has been also argued that since the coefficients of convective heat and mass transfer are directly related, the latter will also reach its highest values at the top of the facade.

Briggen *et al.* tried to address the problem of the sensitivity of WDR CFD simulations to the geometrical details of the facade in 2009 [37]. This work points out such details as a challenge in CFD simulation of WDR. The substantially large difference between the length scales, from several hundred meters (the computational domain) down to a few centimeters (the facade details), and the subsequent need for very fine grids near the building surface are the main

difficulties. Examining results from computer models including different levels of details and by comparison to the results of field measurements, it has been concluded that including the geometrical details yields significant improvements (up to 14%) in the predictions of the numerical simulations. These improvements have all been at the upper portion of the facade and mainly at measurement positions, which are in the “direct vicinity” of such details. Increases as large as 40% in the catch ratio are reported at positions very close to the geometrical details. The effect of the geometrical details has been shown to be less pronounced for higher wind speeds. No conclusion has been made on the lower parts of the facade since “turbulent dispersion was neglected, and modeling accuracy is low at these locations.” Since roof overhangs lay in the finer end of the length scales, the cited study is of importance to the present thesis. It reveals the sensitivity of the results to both the geometry details and their discretization. Geometrical details other than roof overhangs such as fenestrations, balconies, etc. are however not modeled in the current study. As will be discussed in Chapter 3, neglecting these features of the building is a potential source of error.

In 2009, Blocken *et al.* [38] provided a “non-exhaustive” overview of the status of the application of CFD in building performance simulation with a focus on outdoor environment. Different research areas such as pedestrian wind environment around buildings, wind-driven rain on building facades, convective heat and mass transfer coefficients at building surfaces, and air pollutant dispersion around buildings were examined in this paper. The main advantage of the CFD-based simulations in comparison with other methods, specifically wind tunnel measurements, is recognized to be their capacity in producing data for the whole flow field with a high level of control over the conditions. However, the accuracy of CFD is pointed out as an important matter of concern and the need for the assessment of numerical and physical modeling errors by detailed verification and validation studies is highlighted. As related to WDR, two main reasons are given in this work for the limited applicability of CFD. First, the excessively time-consuming character of Lagrangian particle tracking of raindrops that is performed for a large number of combinations of reference wind speed, wind direction and raindrop diameter. Second, with solving the highly turbulent wind flow using the steady state RANS models, the turbulent dispersion of raindrops cannot be accurately modeled. Turbulent dispersion becomes important at lower parts of high-rise building. The first reason has been a serious restricting factor in the numerical simulations of the present study too. A more accurate modeling of turbulent dispersion

is suggested to be possible by transient simulations using Large Eddy Simulation (LES). They also have pointed out that to conquer the problem of intensive Lagrangian particle tracking associated to a transient solution, the traditional Eulerian-Lagrangian framework in CFD-based simulation of WDR should be replaced by Eulerian-Eulerian modeling, wherein the wind flow pattern and raindrop trajectories are both computed in an Eulerian framework.

In 2009, Blocken *et al.* [39] studied WDR deposition on a configuration of a high-rise building screened by a low-rise building using CFD. The two-building configuration was numerically simulated as well as each building separately to analyze the “mutual influence” of the buildings on WDR deposition pattern on them. The wind flow simulations were validated with PIV measurements in a wind tunnel. The authors have explained, as an observation motivating their work, that almost all CFD studies of WDR were conducted for isolated buildings while buildings very rarely stand alone. In addition, the influence of surrounding buildings on the WDR exposure of the facades had needed further investigation. The current thesis examines the effects of overhangs on isolated buildings only, neglecting the effects of the neighbouring construction. It has been also discussed in the mentioned reference that the capability of the CFD techniques to yield details of the spatial and temporal distribution of WDR on facades can be used to study the accuracy of the semi-empirical correlations and, eventually, improve them.

In 2010, Huang and Li presented one of the few implementations of the Eulerian-Eulerian approach to the simulation of WDR [40]. A number of advantages have been pointed out for this approach over the conventional Eulerian-Lagrangian approach. The reasons why the Euler-Euler frame is not widely used in WDR research are also discussed. The focus of this study has been the test building previously studied by Blocken and Carmeliet in 2005 [41]. The numerical results of the presented Eulerian-Eulerian approach are shown to agree well with the available experimental and numerical data.

In 2010 [42], Blocken and Carmeliet compared the semi-empirical model in the ISO Standard for WDR assessment [43], the semi-empirical model by Straube and Burnett (SB) [44] and the CFD model developed by Choi and extended by themselves [25,26]. These three models are acknowledged as “most advanced” and “most frequently used” for the calculation of wind-driven rain deposition on building facades. The focus of this study is the theory and concepts underlying

each of these models and the resulting capabilities and limitations. After a brief review of the historical development of each, implementation of different parameters involved in these models is examined, followed by a comparison in terms of “time and storage, and the potential accuracy.” It has been argued that ISO and SB models are easy-to-use and quick at the expense of generally lower accuracy. On the other hand, CFD simulations are disadvantaged as being time-consuming. However, they can provide information in greater detail that, if carefully applied, can be in good agreement with experimental data. It is also pointed out that the level of complexity and the cost of CFD-based models make them impractical for widespread use. These models, nevertheless, can be used to evaluate and improve the semi-empirical models.

In a following paper in the same year, Blocken *et al.* [45] compared the performance of the three models by applying them to four different isolated buildings under steady state conditions of wind and rain. Two features were investigated in order to make this comparison: the *wind-blocking effect* of the building, which is disturbance introduced by the presence of the building to the upstream wind flow, and reproduction of relation between catch ratio and horizontal rainfall intensity. CFD results are shown to have significantly better accuracy than the predictions of the semi-empirical models, based on the validation efforts for wind flow patterns and WDR deposition patterns obtained from CFD and that the parameters influencing WDR are best implemented in the CFD model. Among other observations, it is also reported that the wind-blocking effect is well reproduced by the CFD model, but not by the ISO and the SB model. It is also concluded that the height and width of the building have both significant effects on the WDR exposure of the facade. The strong effects of the building geometry, especially the ratio of its width to its height, are observed in the present thesis too. The weakness of the semi-empirical models, as demonstrated in the cited paper, is attributed to the fact that only the height of the building is considered in the ISO and SB model, while the influence of building width is neglected (ISO) or considered negligible (SB). The expected increase in the WDR coefficient as the horizontal rainfall intensity increases is clearly shown by the CFD model, whereas the ISO model and the SB model gave opposite trends. This paper draws the conclusion that capabilities and deficiencies of the ISO and SB models should be considered when they are used for WDR deposition calculations. The necessity for further model development using the current models as a “strong and necessary basis” and through validated CFD simulations is emphasized.

Van Hoof *et al.* studied wind flow and WDR in twelve different generic stadium configurations with various WDR shelters using CFD in their 2011 paper [46]. Steady state 3D RANS equations of wind flow were numerically solved in this work using CFD. They made comparisons between the different cases they investigated in terms of WDR exposure and the protection that each configuration provides.

In 2011, Blocken *et al.*, further continuing their comparative studies, made an “intercomparison” of the three models they had examined earlier (CFD, ISO and SB) by applying them to a low-rise test building and a monumental tower building under actual transient rain events [47]. Experimental data from previous studies have been used for the purpose of comparison and validation. Large discrepancies for the ISO and SB models are reported at many facade positions, while good agreement was obtained between the CFD results and the measurements. The reasons for these discrepancies is claimed to be difficult to identify due to the complex nature of the large number of influencing parameters, including geometrical details of the building, *e.g.* roof overhang, and the varying conditions of wind and rain. However, based on the “prior knowledge” of the advantages and disadvantages of these models, a number of reasons are suggested. First, the wind-blocking effect is not taken into account in ISO and SB models. Second, the variation of the overhang shelter with wind speed is not reflected by these models. Finally, ISO and SB models can provide information for a limited number of building geometries only.

In a section of the same work [47], while reviewing the status of *Computational Wind Engineering* (CWE), examination of Large Eddy Simulation (LES) and hybrid Unsteady RANS (URANS)-LES is identified as the next step to be taken in numerical research on WDR. The problems of the steady RANS models, especially in accurately reproducing the separation beyond the windward building edges, are presented as the main motivation behind this possible change of the framework. It is also pointed out that the hybrid approach would lead to a more accurate, yet simpler, representation of the turbulent dispersion of raindrops too. Furthermore, since the combination of the currently used Lagrangian method of tracking raindrops with LES would lead to high computational costs, an Eulerian approach for WDR should be explored to decrease the computational expense effectively. It is argued, in the end of this paper, that the

deficiencies of the present semi-empirical models can be solved using CFD. Detailed results of validated CFD simulations can be used to improve the semi-empirical models.

In conclusion, and as can be seen from this brief chronicle of numerical studies of WDR, the lack of a systematic study of the effects of overhangs on WDR loads should be pointed out. WDR, and its relationship with variables such as wind speed and rainfall intensity, are extensively studied using both numerical and experimental methods. The effects of wind and rain on the deposition of WDR on buildings are examined in detail, even for special events such as gusts and thunderstorms, and are almost completely known. The important role that the treatment of design details, can have on obtaining sound results from numerical simulations is also revealed by different researchers. However, the effects of such details are not fully understood.

As far as roof overhangs are concerned, their effectiveness in protecting the facade from WDR loads are shown in a number of studies. Nevertheless, at least to the knowledge of the author, there are no quantified measures of the effectiveness of the overhang. Moreover, the mechanism through which the overhang protects the facade is not fully understood, nor is the way it could be affected by different parameters, *e.g.* wind speed, rainfall intensity and overhang size.

Considering the large number of variables involved, as well as the uncertainties and the high expenses associated with field measurements, CFD-based numerical simulation seems to be a more efficient method of investigating the effectiveness of overhangs. Field measurements of WDR are generally expensive to set up. Data from field measurements must be recorded over long periods to gather statistically meaningful data, considering the highly fluctuating natures of both wind and rain. Empirical correlations, as discussed in previous sections, are shown to have serious weaknesses in predicating the effects of geometric details such as overhangs. Numerical simulation using the existing RANS-based CFD techniques, on the other hand, is, in general, less expensive, faster and more reliable. Various studies have shown the validity of CFD-based simulation of WDR and CFD is now established as a reliable tool in this research area. Furthermore, compared to field measurements, there is a higher level of control over variables in numerical simulation. Comparison of WDR loads on facades of a building with and without an overhang under exactly the same wind and rain conditions is possible through CFD-based simulation and the possible differences can be attributed to the overhang only.

1.4. Scope

This thesis is part of the Natural Sciences and Engineering Research Council of Canada's NEWBuildS network. NEWBuildS is a multi-disciplinary NSERC strategic research network for Engineered Wood-based Building Systems. The current research falls under *Theme 4: Building systems – durability, sustainability and enhanced products*. The long-term goal of the research is to develop a methodology to assess the wind-driven rain loads on any given mid-rise building and to evaluate the impact of wind-driven rain on building envelopes. Appropriate technical solutions to WDR moisture-related problems can then be developed to reduce building envelope failures. The key objective of the project is to provide recommendations on design of effective roof overhangs for mid-rise buildings eventually.

As discussed in the previous sections, although roof overhangs are known as an effective solution to the problems caused by WDR, their effects are not known in detail. This work intends to investigate the performance of overhangs in terms of protecting facades from WDR. Different variables, namely, overhang size, wind speed, wind angle and rainfall intensity, and their influence on the performance of the overhang are examined. Effort is made to provide a fundamental understanding of the mechanisms through which overhangs affect WDR deposition on facades. The main approach of this study is numerical simulation based on Computational Fluid Dynamics (CFD). As is essential to any numerical study, validity of the solution is confirmed by comparison to field measurements and other existing data from the literature.

The prime subject of this thesis is a low-rise cubic building. With the original scope of the project as well as practical considerations in mind, an actual mid-rise building will be briefly studied too. Results comprise WDR wetting patterns (*catch ratio* contours) of facades mainly, which can reveal the effects of overhangs. There is also a need for a global measure to quantify the protection provided by overhangs against WDR. Effort is made to establish such a measure and show its consistency with other parameters used to describe WDR.

CHAPTER 2

Numerical Simulation of Wind-Driven Rain

From a fluid mechanics point of view, WDR is a multiphase¹ flow of wind and rain. However, based on certain assumptions, the flow could be solved in simpler ways. It is conventional in WDR studies to assume that the contribution of raindrops to the momentum of the wind phase is so small compared to the highly turbulent bulk of the wind flow that it could be neglected. Therefore, the coupling between the two phases is a “one-way” coupling [48]. This is because the volume fraction of raindrops in space is low ($\sim 10^{-6}$) even for heavy rainfalls (See Appendix A). Hence, the rain phase may be treated as a *dilute* phase. Moreover, the average spacing between the falling raindrops is large enough (~ 10 cm [49]) that the rain phase may be treated as a *discrete* phase, *i.e.* the interaction between the raindrops is also negligible. There are two main practical advantages to these assumptions; first that the Reynolds Averaged Navier–Stokes equations of wind flow can be solved for the wind phase independent of the rain phase, and second, that the equations governing the motion of raindrops can be simplified to an ODE [10] and easily solved using numerical integration techniques.

In this chapter, numerical solution of wind flow around the building using Computational Fluid Dynamics is first discussed. In the second section, the equation of motion of raindrops and its solution are discussed. The third section is devoted to the computation of catch ratio values based on the raindrop trajectories.

2.1. Particle Laden Turbulence

Turbulent shear flows dispersing solid or liquid particles are known as *particle-laden* flows [48]. WDR is categorized as a particle-laden flow. The coupling between the phases involved in such flows is mainly determined by the volume fraction of the particles, their mass fraction and their *Stokes* number, which is a measure of the inertia or “responsiveness” of the particles [50]. Figure 2.1, which is adapted from reference [48], shows the division between the different regimes of

¹ Note that rain consists of different phases, rather than a single liquid phase, as it comprises a combination of raindrops varying in shape and size. However, in the remainder of this text, rain may be referred to as a single phase.

interaction between the suspended particles and the flow. The horizontal axis is the volumetric fraction of the particle (here, the rain raindrops) in the bulk flow (air). The vertical axis is a representation of the Stokes number, *i.e.* the ratio between the characteristic time of the particle (τ_p) to the viscous time scale of the flow (τ_κ).

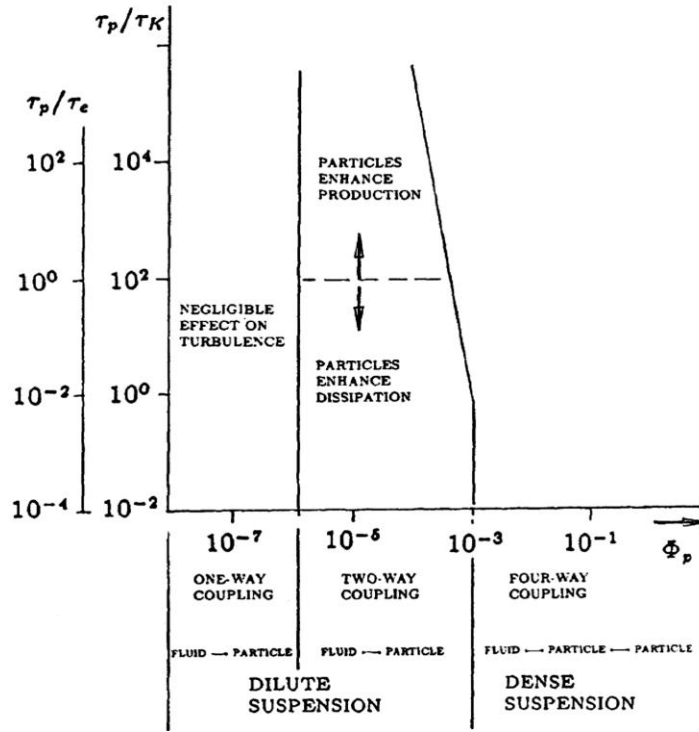


FIGURE 2.1 – REGIMES OF INTERACTION BETWEEN PARTICLES AND THE FLOW [48]

As seen in this diagram, in the one-way coupling region, *i.e.* where the particle-flow and particle-particle interactions are negligible, volume fraction is the decisive factor determining the regime of the flow. The volume fraction of the wind-driven raindrops is calculated as

$$\Phi = \frac{V_{wdr}}{V_{air}} = \frac{1}{V_{air}} \int_d V(d) dd \quad (2.1)$$

As shown in Appendix A, this expression has an implicit dependency upon the intensity of rainfall. For the typical rainfall intensities of interest to the present study, the volume fraction of WDR does not exceed 10^{-6} in order of magnitude. As shown in Fig. 2.1, the one-way coupling region is independent of the time scale ratio, *i.e.* the Stokes number.

2.2. Numerical Simulation of Wind Flow

This section is devoted to the solution of wind flow around buildings. Governing equations, boundary conditions, and the details of the numerical schemes used for solving the flow are discussed briefly.

2.2.1. Governing Equations

The wind flow is described by the continuity and the Reynolds Averaged Navier–Stokes (RANS) equations, which, in conservative form and using compact notation, may be written as:

$$\rho \frac{\partial u_i}{\partial t} + \rho u_j \frac{\partial u_i}{\partial x_j} = -\frac{\partial p}{\partial x_i} + \frac{\partial \tau_{ji}}{\partial x_j} + S_i \quad (2.2)$$

Here, ρ is the density of air, u_i denotes the time-averaged velocity, p is the pressure, τ_{ji} is the shear stress tensor and S_i is the momentum source term including the contribution from the rain phase. Under steady state conditions, and neglecting the momentum source term S_i , the RANS equations above are simplified to

$$\rho u_j \frac{\partial u_i}{\partial x_j} = -\frac{\partial p}{\partial x_i} + \frac{\partial \tau_{ji}}{\partial x_j} \quad (2.3)$$

which in combination with a turbulence model form a *closed* set of equations.

2.2.2. Modeling Turbulence

Turbulence, as proposed by Taylor and von Karman in 1937, “is an irregular motion which in general makes its appearance in fluids, gaseous or liquid, when they flow past solid surfaces or even when neighbouring streams of the same fluid flow past or over one another” [51]. Turbulence follows Navier-Stokes equations and with a proper set of initial and boundary conditions defined, numerical computation of any turbulent flow should be possible [52]. Nevertheless, this turns out to be only true in an abstract sense. The large number of degrees of freedom of a turbulent flow makes it “impractical” to be “directly” computed [51]. There are two major modeling approaches to the problem of turbulence; averaging (*e.g.*, Reynolds averaging) and filtering (*e.g.*, Large Eddy Simulation).

In this work, and mainly based on the works of Blocken [8,9,10], Reynolds-averaged equations of wind flow are solved using a realizable k- ϵ turbulence model [51].

k- ϵ is one of the two-equation turbulence models in which *turbulence kinetic energy* (k) and *dissipation rate* (ϵ) are both given as functions of the fluctuating component of the velocity vector. This model has two additional PDEs derived from the conservation of turbulence kinetic energy and by taking a moment of the Navier-Stokes equation [51]. There are different variations to the k- ϵ model. The model used in this study is called the realizable k- ϵ model, with the term “realizable” referring to mathematical constraints of the model that make it consistent with the physics of turbulent flows [53].

Realizable k- ϵ Model

The realizable k- ϵ model was proposed in 1995 by Shih et al. [54] with the intention of addressing some of the deficiencies of traditional k- ϵ models. Extensive validation studies have been carried on this model. The model has been tested on a wide range of different flows including separated flows that are of particular interest to the present work. Its performance has been found to be substantially better than the standard k- ϵ model for separated flows [53]. As mentioned in section 1.3, results of a study of the effects of turbulence modeling on evaluating WDR loads on buildings published in 2008 [33] have shown that, overall, different turbulence models yield nearly the same wetting patterns.

Wall Functions

Solid boundaries significantly affect turbulence. No-slip condition at the wall affects the mean velocity. Moreover, viscous damping reduces the tangential velocity fluctuations and kinematic blocking reduces the normal fluctuations. On the other hand, turbulence is rapidly enhanced in the outer part of the near wall region as the large gradients in mean velocity produce turbulence kinetic energy [53].

Near-wall treatment is therefore crucial to the accuracy of modeling turbulence. “The k- ϵ model is primarily valid for turbulent core flows” and consideration needs to be given when using these models for wall-bounded flows [53]. There are two main approaches to modeling the near-wall region. In one approach, the viscous sublayer and buffer layer are not resolved. Rather, semi-

empirical formulas called “wall functions” are used to bridge these regions to the turbulent core. The other approach modifies equations of the turbulence model so that the viscosity-affected region of the turbulent boundary layer could be resolved with a mesh all the way to the solid wall. Standard wall functions, which “work reasonably well for a broad range of wall-bounded flows” and are the default setting of the FLUENT solver [53], are used in this work.

2.2.3. Computational Domain

Figure 2.2 shows a typical computational domain. For the preliminary validation study (see Chapter 3), the domain size was chosen based on the case presented in Appendix J of reference [10]. Generally, the domain size is modified so that the far field boundaries would not affect the flow around the building.

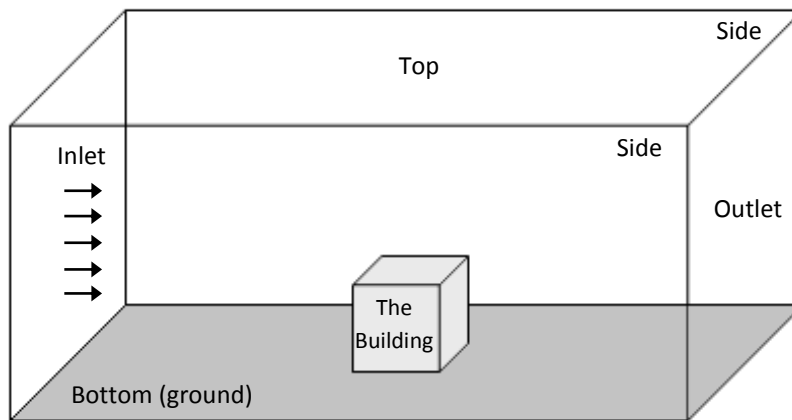


FIGURE 2.2 – SCHEMATIC OF THE COMPUTATIONAL DOMAIN

2.2.4. Boundary Conditions

In this section, the conditions at the boundaries of the computational domain are described.

Inlet Conditions

The inlet wind velocity has as an exponential profile as described by Eq. (2.4), with the direction of the flow being normal to the inlet boundary.

$$U(y) = U_H \left(\frac{y}{H} \right)^{\alpha_p} \quad (2.4)$$

Here, U_H is the velocity of the wind at height H above the ground, y is the elevation from the ground and exponent α_p depends on the terrain type over which the upwind wind flow is developed [55].

Inlet turbulence kinetic energy and a modified dissipation rate are set at the inlet boundary based on the work of Blocken [10] as

$$k = \frac{(u_{ABL}^*)^2}{\sqrt{C_\mu}} \quad (2.5)$$

and

$$\varepsilon(y) = \frac{(u_{ABL}^*)^3}{\kappa(y + y_0)} \quad (2.6)$$

In these equations, y_0 is the aerodynamic roughness length and u_{ABL}^* , the *friction velocity*, is a measure of the velocity fluctuations in the turbulent boundary layer

$$u_{ABL}^* = \sqrt{\frac{\tau_w}{\rho}} \quad (2.7)$$

Different values for u_{ABL}^* are given in [10] based on measurements of the wind velocity profile. A representative value of 0.69 m/s has been used in the current study. $C_\mu=0.09$ is one of the constants in the k- ε model [51]. The more frequently used value of 0.42 for the Von Karman constant κ has been used here [10, 51].

Outlet Conditions

The outlet is set as a pressure boundary condition with the gauge back pressure forced to be zero.

Solid Surfaces

Solid surfaces, *i.e.* the bottom of the domain that represents the ground and the building walls, are set as impermeable no slip boundaries.

As related to turbulence, roughness height and a roughness constant need to be specified on solid boundaries. The default roughness constant of 0.5 [53] is used in all cases. The ground roughness is set based on the representative values for different terrain types as given in reference [56]. Zero roughness height is chosen for the building walls. The error introduced to the simulation by this approximation is unknown. However, it is suspected to be small compared to the uncertainties due to turbulence modeling and other approximations and assumptions. Ideally, an equivalent non-zero roughness representing both the surface roughness and the geometrical details excluded from the model, such as balconies, should be calculated. This equivalent roughness length should then be implemented at the boundaries representing the building walls.

Side Boundaries

The two sides and the top of the domain are set as symmetric boundaries. Normal to these boundaries, the velocity and the gradient of the other field variables would be zero.

2.2.5. Numerical Solution

The commercial CFD package ANSYS FLUENT 14 has been used to solve the equations of motion of wind. Different details of the numerical solution are briefly discussed in the following sections.

Spatial Discretization

ANSYS GAMBIT 2.4.6 has been used to create and discretize the model. Surfaces of the domain are meshed using quadratic elements. Structured elements (*mapping* scheme) are generated on the building walls and the domain boundaries, except for the bottom of the domain (representing the ground) where an unstructured scheme (*pave*) is implemented. The volume is discretized using tetrahedral elements. A grid convergence study has been performed to ensure grid independence and to estimate discretization errors (see Chapter 3).

Solution Schemes

A second order solution of the continuity, RANS and k- ϵ equations is sought using SIMPLE pressure–velocity coupling and Standard pressure discretization [53].

The solution is initialized using *hybrid initialization*. The *Full multigrid* (FMG) initialization technique is used in a number of cases to accelerate convergence [53].

Numerical Convergence

The solution convergence is monitored based on residuals of the governing equations as well as the average pressure coefficient on the building. In some cases, the magnitude of velocity vectors at certain positions upstream of the building are also examined to ensure convergence. At convergence, scaled residuals of the continuity, momentum and k-ε equations are all smaller than 10^{-4} .

2.3. Numerical Simulation of Rain

Simulating a stochastic phenomenon such as rain is only possible through simplification and assumptions. This section is devoted to the details of the simulating rain as it is driven to the building. Governing equations, boundary conditions, and the details of the numerical schemes used for computing the raindrop trajectories are discussed.

2.3.1. Governing Equations

In a Lagrangian framework, and based on the assumption of a dilute discrete phase, the equation governing the motion of raindrops is reduced to the ODE

$$\rho_w \frac{d^2 \vec{r}}{dt^2} = (\rho - \rho_w) \vec{g} + \vec{F}_D \quad (2.8)$$

where \vec{r} is the position vector of the droplet, ρ_w is the density of rainwater, ρ is the density of air, \vec{g} is the gravitational acceleration and \vec{F}_D is the drag force. The first term on the RHS of Eq. (2.8) represents the buoyancy force exerted on the raindrops as they fall in the air under the gravity field.

Based on the definition of the drag coefficient, C_D , the magnitude of the drag force can be calculated as

$$F_D = C_D \left(\frac{\rho}{2} \left| \vec{u} - \frac{d\vec{r}}{dt} \right|^2 \right) A_f \quad (2.9)$$

with A_f being the frontal area of the raindrop. The vector \vec{F}_D is in the same direction as the velocity vector of air with respect to the raindrop $(\vec{u} - \frac{d\vec{r}}{dt})$.

Eq. (2.8) can then be rearranged to the form below, as given in reference [10]

$$\frac{d^2\vec{r}}{dt^2} = \left(\frac{\rho - \rho_w}{\rho_w} \right) \vec{g} + \frac{3\mu C_D \text{Re}_d}{4\rho_w d^2} \left(\vec{u} - \frac{d\vec{r}}{dt} \right) \quad (2.10)$$

Here,

$$\text{Re}_d = \frac{\rho d}{\mu} \left| \vec{u} - \frac{d\vec{r}}{dt} \right| \quad (2.11)$$

shows the raindrop Reynolds number, based on the raindrop diameter (d) and the magnitude of the relative velocity of the continuous phase (air) with respect to it.

The position vector, \vec{r} , can be obtained by numerically integrating Eq. (2.10) using standard techniques such as Runge-Kutta.

The Discrete Phase Model (DPM) module of the commercial CFD package ANSYS FLUENT is used to perform the Lagrangian particle tracking and calculate raindrop trajectories.

2.3.2. Integration Time Step

Regardless of the numerical scheme used, a time step size Δt must be defined in order to integrate the ODE obtained in Eq. (2.10). This integration time step is computed based on a *length scale* (L), the speed of the particle (u_p) and the speed of the continuous phase (u_c):

$$\Delta t = \frac{L}{u_p + u_c} \quad (2.12)$$

As defined by the Eq. (2.12), the length scale L is proportional to the integration time step and is equivalent to the distance that the particle will travel before its trajectory is updated. For the cases presented in this work, a length scale of 0.001 m, which is of the same order of magnitude as the raindrops size, has been used.

A smaller value for this length scale increases the accuracy of the trajectory calculations for the discrete phase. However, particle positions are always computed when particles cross the boundaries of control volumes [53]. Therefore, even if a very large length scale is specified, the time step used for integration will be adjusted so that the control volume would be traversed in one step. It is thus assumed that when a sufficiently fine CFD grid is used for the wind flow, the length scale for particle tracking will be more or less unimportant. Yet, the length scale may be *too small*, *i.e.* is computationally inefficient.

2.3.3. Boundary Conditions

Injection Position

The location of the *injection plane*, *i.e.* the surface from which the raindrops are injected into the domain, is determined by trial and error so that the raindrops would end up in the region of interest on the facade.

A perturbation study has been performed to examine the sensitivity of raindrop trajectories and catch ratio values to the injection positions (see Appendix B).

Initial Vertical Velocity

Raindrops are injected into the computational domain with a vertical velocity equal to their terminal velocity of fall. This velocity is adopted from the experimental work of Gunn and Kinzer [57]. The dynamics of free falling raindrops is quite complicated and it is well known that, especially as the size increases, the shape and behaviour of raindrops deviate considerably from perfectly spherical particles. Although the mentioned study is performed in stagnant air, its

results are widely applied to WDR too. Since, in the numerical simulation, a discrete set of raindrop diameters is used to represent the whole raindrop size spectrum, the measured values of the raindrops terminal velocity of fall are implemented as a *look-up table* at the injection boundary conditions.

Initial Horizontal Velocity

The initial horizontal velocity of each raindrop upon injection into the domain is set as the velocity of the undisturbed wind at the same height as the injection position. The condition essentially means no initial slip (in horizontal direction) between the continuous and discrete phases.

Interaction with Solid Surfaces

The solid surfaces, namely, the bottom of the domain (the ground) and the building walls, will *trap* the raindrops upon impact. This means that the raindrops are removed from the domain after they hit a solid boundary for the first time.

2.3.4. Raindrop Drag Law

The behaviour of falling raindrops is known to deviate from that of perfect spheres. This is mainly because of the deformation of initially spherical droplets due to the drag force they experience as they fall in the atmosphere. The main factors affecting the shape of a raindrop, and thus its drag coefficient, are the gravitational force, the hydrostatic pressure within the raindrop, the aerodynamic pressure (drag) and the surface tension [58]. For example, surface tension tends to minimize the surface area of the raindrop. On the other hand, due to boundary layer separation past the droplet, regions of high curvature gradient are likely to occur, so that the high surface tension in such locations would balance the high pressure gradients due to presence of the wake.

The conventional drag laws in the study of multiphase flows are the Morsi-Alexander [59] law and various modifications of the Stokes law. However, the former involves *shape factors* which may be calculated only with the knowledge of particle geometry (surface area) and thus is not applicable to the wind driven raindrops. On the other hand, using Stokes law for non-spherical particles, including the largely deflecting raindrops, is questionable.

A set of experimental data on the drag coefficient of free-falling raindrops as a function of the raindrop Reynolds number [57] is used here. Nonetheless, and unlike the terminal velocity of fall, since a continuous range of Reynolds numbers is likely to occur, an analytical expression for the drag law is required. Equation (2.13) is a fourth order polynomial curve is fitted to the data from reference [57].

$$\log(C_D) = 0.0358z^4 - 0.2255z^3 + 0.5731z^2 - 1.2462z + 1.4633 \quad (2.13)$$

with $z = \log(\text{Re}_d)$.

This curve fit is implemented as a User Defined Function (UDF) in the DPM toolbox of FLUENT.

Comparison between spherical drag law and this curve fit, as seen in Fig. 2.3, shows that large raindrops ($d > 3 \text{ mm}$) tend to have a larger deviation from perfectly spherical behaviour. The observed deviation also can be explained by considering the deformation of the raindrops and the fact that larger drops will have an effective frontal area significantly greater than the area calculated based on their nominal diameter.

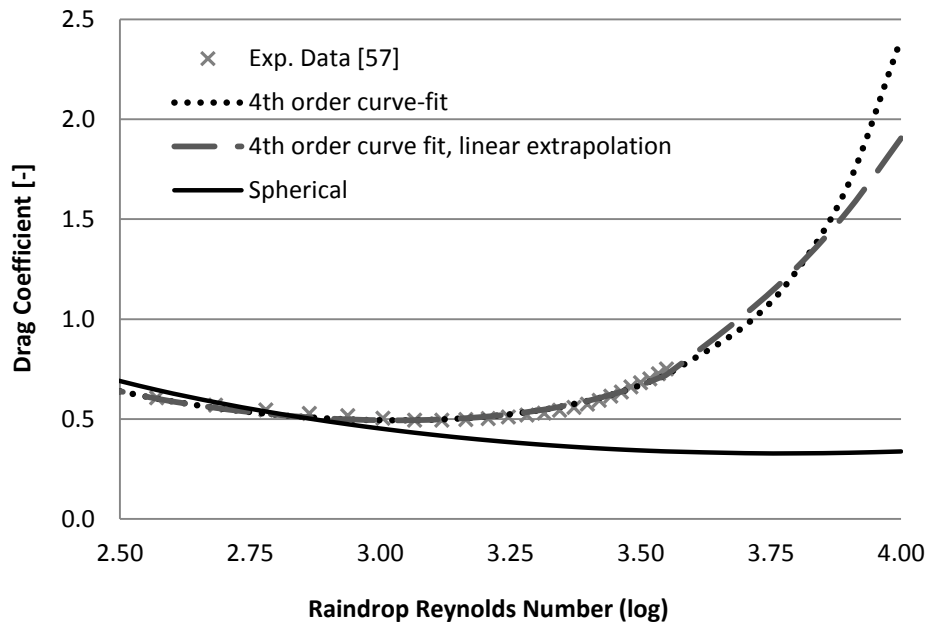


FIGURE 2.3 – COMPARISON OF DIFFERENT DRAG LAWS FOR HIGH RAINDROP REYNOLDS NUMBERS

Moreover, since there is no experimental data for a relatively small range of the Reynolds numbers that are likely to occur ($\sim 10^{3.5}$ - 10^4), two extrapolation methods were tested; one based on the same 4th order curve fit, and the other one based on linear extrapolation of the last two data points.

As seen in Fig. 2.3, the extrapolations both have a large deviation from the spherical drag law. However, numerical tests have revealed that implementation of either of these two drag laws in the simulations does not affect the Lagrangian tracking of the raindrops and their distribution on the building facade significantly.

2.3.5. Raindrop Diameter Distribution

Raindrops with different sizes are observed in a rainfall event. Usually, raindrops are likely to form with an *equivalent* diameter, *i.e.* diameter of the sphere with the same volume as that of the raindrop, within the range of 0.3 mm to 6 mm. A widely used correlation for the probability of each diameter occurring in a rainfall is given by Best [60] as function of the intensity of the rainfall and the raindrop diameter.

The original expression given by Best [60] is a *volume-based* function, which needs to be modified to a *flux-based* expression. Blocken [10] has suggested such a modification based on the terminal velocity of free falling raindrops, as given by Eq. (2.14)

$$f_h(d) = \frac{f(d)V_t(d)}{\int_a f(d)V_t(d)dd} \quad (2.14)$$

Here, f_h is the modified probability density function (PDF), f is the original PDF from reference [47] and V_t is the terminal velocity of fall. The integral is taken over the whole size spectrum.

It is noteworthy that Best's distribution is based on a wide range of experimental data at different locations including, in particular, studies in Canada. It is suspected, however, that this distribution may be influenced by local climate conditions (such as cloud elevation) in addition to parameters such as rainfall intensity. As illustrated in Chapter 1, a large body of the numerical research in WDR is performed for European conditions. Nonetheless, whether the same relations

can be used for other regions and climates, and the possible error introduced to the simulation by doing so, is not completely known. Despite this, and considering the scope of this work, the same diameter distribution is used here.

2.3.6. Turbulent Dispersion of Raindrops

Turbulent dispersion, which is the transport of droplets by the fluctuating component of the turbulent velocity of the continuous phase, is neglected in favour of computational effort, as is usual in discrete phase modeling and specifically numerical studies of WDR.

Moreover, as the current approach is based on a steady state solution of the wind flow using RANS turbulence models, considering turbulent dispersion of raindrops, which is an unsteady feature of turbulence, is not very meaningful [10].

Turbulent dispersion of raindrops is however known to be a probable reason for the discrepancies between the results of different numerical and experimental studies. The role of this phenomenon could vary depending on the building geometry and the position on the facade [34]. It has been suggested that, if desired, a more accurate modeling of turbulent dispersion can be done by transient simulations using turbulence models such as Large Eddy Simulation [34].

2.4. Numerical Simulation of Wind-Driven Rain

Modeling wind-driven rain using the method proposed by Choi [20], which is the basis of this work, consists of four main steps:

- i.* Solution of wind flow around the building,
- ii.* Performing the Lagrangian particle tracking raindrops with different diameters,
- iii.* Calculation of specific catch ratios based on the configuration of raindrop trajectories,
- iv.* Integrating the results of step (*iii*) to calculate catch ratio as a *weighted average* of the specific catch ratios.

The first two steps are discussed in sections 2.2 and 2.3 respectively. The calculations corresponding to these steps are done by the commercial CFD package FLUENT. The remaining two steps, for which a MATLAB code has been developed, will be treated in this section.

2.4.1. Catch Ratio

As mentioned previously, the main parameter of interest in this study is catch ratio. For fixed wind conditions, catch ratio is, in general, a function of raindrop diameter (d) as well as time. In the case of a constant rainfall event and under steady state wind conditions, time dependency will vanish and the catch ratio will be a function of raindrop diameter only:

$$\eta(d) = \frac{R_{wdr}(d)}{R_h(d)} \quad (2.15)$$

Moreover, mass conservation requires that

$$R_h A_h = R_{wdr} A_f \quad (2.16)$$

where R_h is the *horizontal* rainfall intensity, A_h is the area of a horizontal surface at a certain height above the ground, R_{wdr} is the vertical component of the rainfall flux vector at the facade and A_f is the wetted area on the building facade, as depicted in Fig. 2.4. Thus, the expression defining *specific* catch ratio may be rewritten as

$$\eta_d = \frac{A_h(d)}{A_f(d)} \quad (2.17)$$

Figure 2.4 is a graphical representation of the idea behind catch ratio and horizontal and wetted areas.

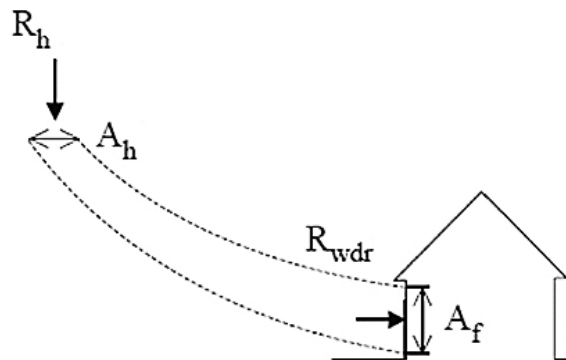


FIGURE 2.4 – REFERENCE AND VERTICAL WETTED AREAS THAT APPEAR IN THE DEFINITION OF CATCH RATIO [10]

Integrated over the range of raindrop diameters that are likely to occur in a rainfall event, a weighted average of specific catch ratios may be calculated as

$$\eta = \int f_h(d)\eta_d dd \quad (2.18)$$

where the weighting function $f_h(d)$ is the probability density function of each raindrop size (see section 2.3.5).

A trapezoid scheme is utilized to calculate the integral of the definition of catch ratio (Eq. (2.18)) numerically:

$$\eta = \sum_i f_h(d_i)\eta(d_i)\Delta d_i \quad (2.19)$$

In order to calculate this summation, values of specific catch ratio, $\eta(d_i)$, are first calculated for raindrop diameters of 0.3 to 6 mm. This range is taken based on the population distribution given in reference [60] as well as for comparison with reference [10]. As in reference [10], within the range of 0.3-1 mm, an increment of $\Delta d=0.1$ mm will be used, while for the range of 1-6 mm, raindrop diameter is increased by an increment of $\Delta d=0.2$ mm. For the ends of the range, $\Delta d=0.05$ mm is used. Then, each specific catch ratio is multiplied by $f_h(d_i)$, the occurrence probability raindrop with size d_i , as the weighting function. Finally, the summation is taken over the weighted specific catch ratios multiplied by the proper bin size (Δd_i).

2.4.2. Computational Methods for Area Calculations

As described in the beginning of this section, for steady state problems, calculation of the specific catch ratio reduces to calculation of the *wetted* area, A_f , which is the portion of facade area covered by raindrops released from some reference horizontal area (A_h).

Once the particle trajectories are computed and the distribution of raindrops on the facade is determined, the facade is divided into rectangular *cells*. These cells are the computational representation of WDR gauges. To determine the value of catch ratio in each of such cells, the wetted area A_f in the cell and a reference horizontal area A_h need to be calculated. The numerical procedure for computing these areas starts with identifying the raindrops in each rectangular cell and tracking them back in the particle tracking dataset to find where they originally were

released from. Reference and wetted areas are then calculated based on the configuration of raindrops. Figure 2.5 shows typical distribution of the raindrops in one of the rectangular cells on the facade.

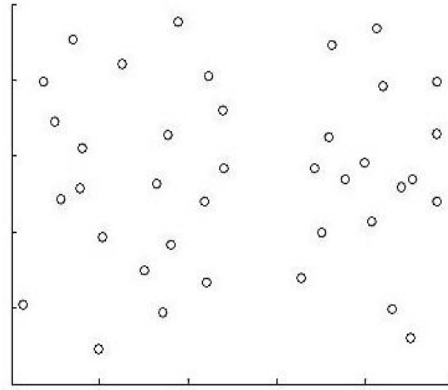


FIGURE 2.5 – TYPICAL DISTRIBUTION OF RAINDROPS ON A CELL ON THE FACADE

The fundamental assumption underlying this approach is that adjacent raindrops form *streamtubes*. All the raindrops injected in a streamtube will remain inside the streamtube until they hit the facade. These streamtubes, while passing through the wind flow field, will deform and distort and catch ratio is a measure of the expansion or contraction that a streamtube experiences.

Two different methods are tested to estimate the area wetted by the streamtube ending up in each cell and the horizontal area from which this streamtube has been released. In the first method, hereinafter referred to as *extremum rectangle*, a rectangle is formed based on the extremum positions of the drops, *i.e.* maximum and minimum coordinates on the planes containing the facade and the horizontal surface.

The second approach, referred to as *convex hull*, is based on the algorithms developed to solve a classical problem in computational geometry known by the same name. The question is to determine the circumscribing polygon which would contain (or include) all members of a given set of planar points. Different solutions such as the *gift wrapping method* are proposed for this problem and robust numerical algorithms are developed based on them [61]. Details of these algorithms are beyond the scope of this thesis. Based on comparisons with published data (see Chapter 3), the convex hull method is used in this study. This method is also more consistent

with the physics the phenomenon. Typical *wetted areas* formed based on both these methods are shown in Fig. 2.6.

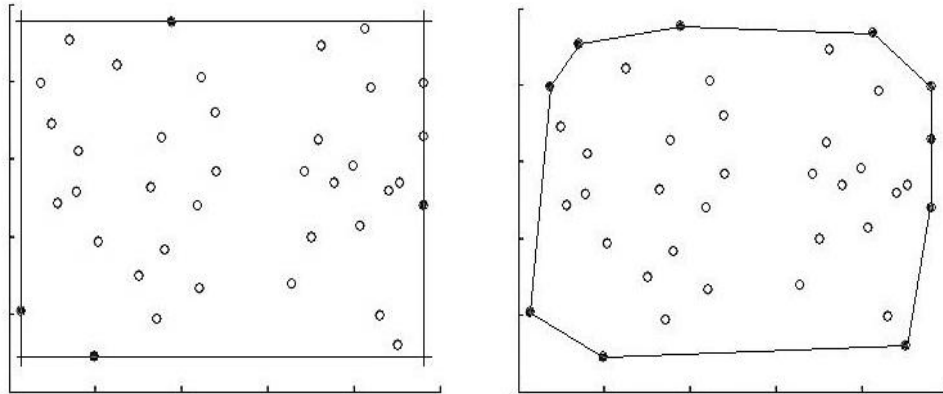


**FIGURE 2.6 – AREAS FORMED BY EXTREMUM RECTANGLE (LEFT)
AND CONVEX HULL (RIGHT) METHODS**

CHAPTER 3

Verification, Validation & Accuracy

Verification and validation are essential parts of any numerical study. Verification deals with mathematics and addresses the correctness of the numerical solution to a given model, while validation deals with how the physics of the problem are treated and addresses the appropriateness of the model [62]. In this chapter, general verification of the solver and validation of the present approach to simulating wind-driven rain are presented, followed by a brief discussion of the sources of error and uncertainty.

3.1. Verification

The commercial CFD package FLUENT, which is part of the ANSYS Fluid Dynamics suite, is verified in several studies. For instance, reference [63] is a comprehensive verification document based on as many as 66 different cases, including 3D, turbulent and multiphase flows. The close agreement between the ANSYS solutions and the theoretical or experimental results, as reported in this reference, shows the high level of reliability of the solver.

3.2. Validation

Blocken et al. [39] have suggested two methods for validating CFD-based simulations of WDR:

- i)* by comparing calculated and measured wind-flow patterns, and
- ii)* by comparing calculated and measured WDR amounts.

Here, a combination of the two is presented.

3.2.1. Validation of the Numerical Solution of Wind Flow

In the 4-step technique¹ used in this work for modeling WDR, the most important modeling assumptions are embedded in solving the wind flow field with steady RANS equations and a turbulence model (step *i*). Implementation of the Discrete Phase Model, assuming a one-way coupling between the wind and rain phases, makes the first step even more critical. Therefore,

¹ See section 2.4.

different features of the flow field, especially in a close neighbourhood of the building, must be carefully examined in order to ensure validity of the results. The calculations in steps *ii* to *iv* are generally considered less critical although they are based on certain assumptions and might require validation too.

In this section, the CFD results for the wind flow field around the building are validated by a visual examination of the flow patterns and by comparing the CFD results of the stagnation pressure on the building with the theoretical predictions.

Flow Patterns

Different features of flow around a rectangular building are shown in Fig. 3.1. The most significant features are the division of the streamlines into *upwash* and *downwash* at almost two-third height of the windward facade, the upstream (standing) vortex, the relatively large wakes over the building roof and edges, and the recirculating region past the building.

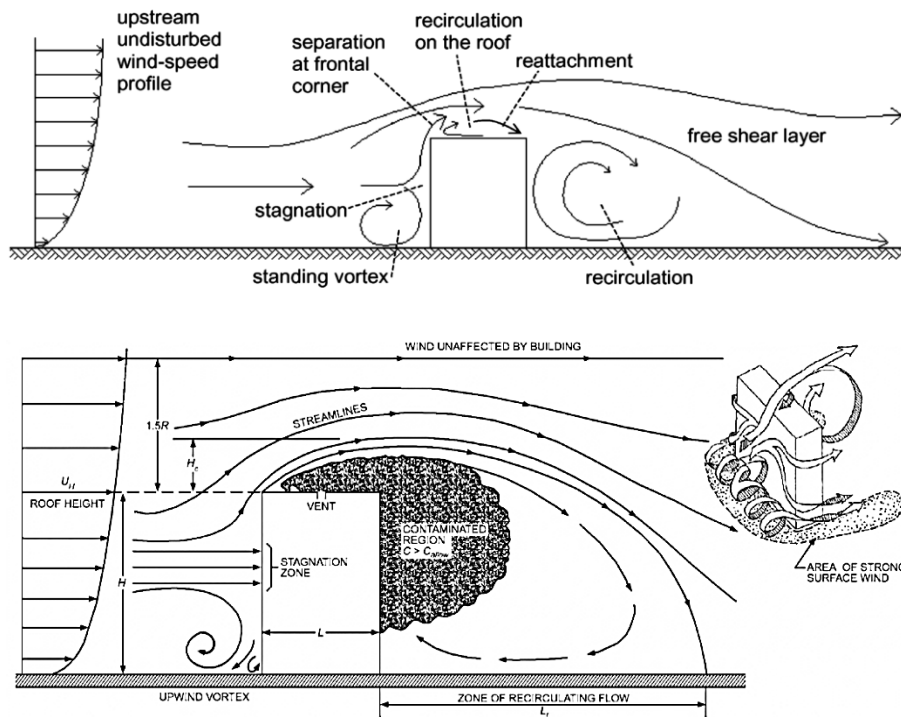


FIGURE 3.1 – FLOW PATTERNS AROUND BUILDINGS AS PRESENTED IN REFERENCES [10] (TOP) AND [25] (BOTTOM)

The same patterns around a cubic building as the ones depicted in Fig. 3.1 are generated by the CFD solution, as shown in Fig. 3.2. It is thus concluded that the main features of the flow are captured by the present CFD solution.

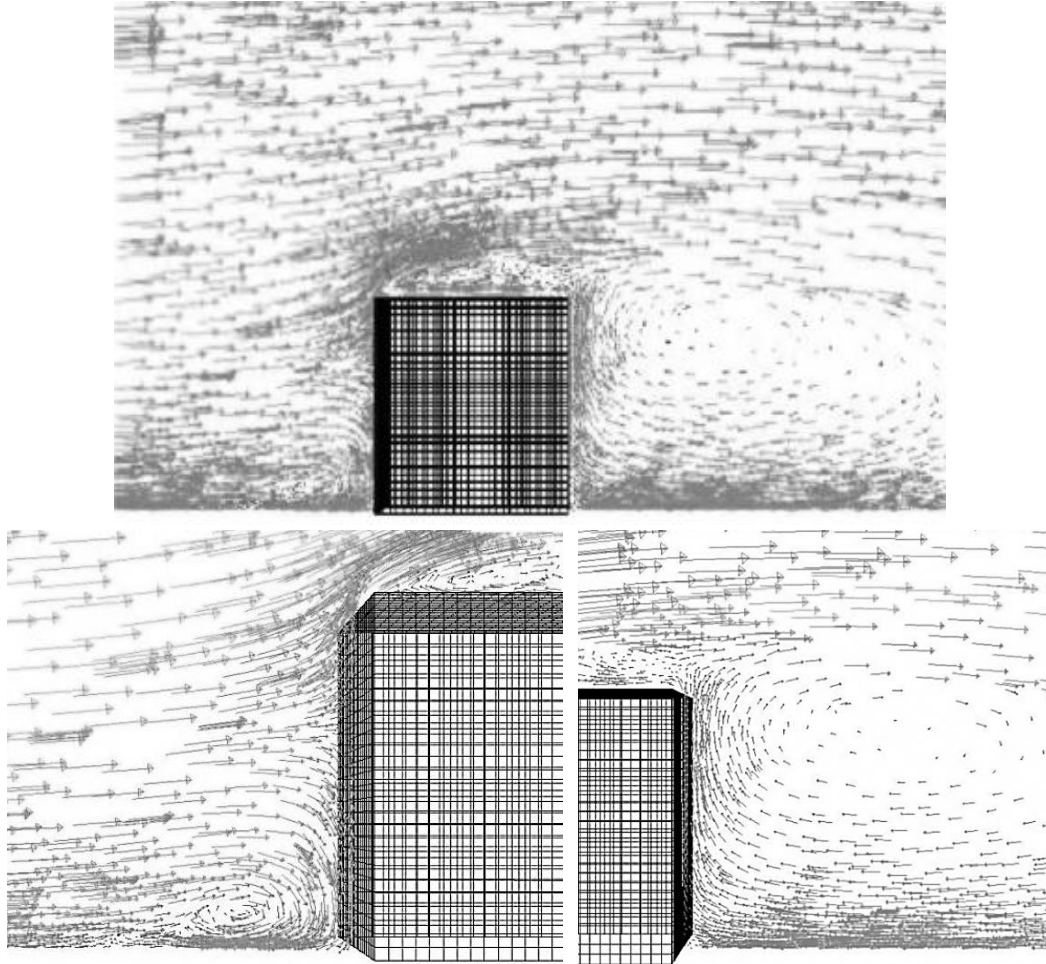


FIGURE 3.2 – SIDE VIEWS OF THE WIND VELOCITY VECTOR FIELD (CFD)
TOP: GENERAL PATTERN AROUND THE BUILDING
BOTTOM: UPSTREAM VORTEX, UPWASH AND DOWNWASH (LEFT)
AND DOWNSTREAM RECIRCULATING REGION (RIGHT)

Stagnation Pressure

Figure 3.3 shows the stagnation pressure distribution on a cubic building. This figure is generated for a $U_{10}=10$ m/s wind, approaching the building in the normal direction. The general pattern is similar for different wind speeds, but obviously different for different wind angles.

Maximum stagnation pressure has been compared, and proven to be in good agreement, with the predictions based on the Bernoulli equation as discussed in reference [25]. This maximum is likely to occur at almost two-third of the building height [25]. CFD results, as seen in Fig. 3.3, show the same approximate location on the windward facade.

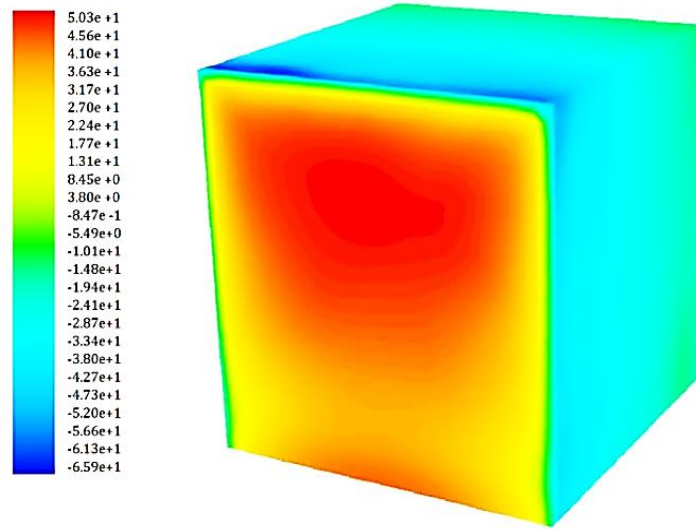


Figure 3.3 - PRESSURE DISTRIBUTION ON THE BUILDING PREDICTED BY CFD FOR $U_{10}=10$ m/s (Pa, gauge)

Based on the undisturbed wind speed at two-thirds of the building height, the Bernoulli equation yields a stagnation pressure of 54.24 Pa, for $U_{10}=10$ m/s, while the CFD solution predicts a maximum pressure of 50.3 Pa on the building. The close agreement between these results is another indication of the validity of the current CFD solution.

Typical values for the surface-averaged pressure coefficient are also given in reference [25] for low- and high-rise buildings. The results of CFD are in very good agreement with these values too. For example, the area-weighted average pressure coefficient on the windward facade of the cubic building subject to a normal wind with $U_{10}=10$ m/s is predicted by CFD to be about 0.59, while the mentioned reference suggests an approximate range of 0.4-0.6. CFD pressure coefficients have been calculated with U_{10} as the reference velocity.

3.2.2. Validation of Catch Ratio Calculations

In addition to the CFD solution of the wind flow, the Lagrangian particle tracking of the raindrops and the post-processing MATLAB code developed for determining the distribution of

raindrops on the building and calculating catch ratio values need to be validated too. These calculations correspond to the steps *ii*, *iii* and *iv* of Choi's method [20]. In this section, the catch ratio values calculated in the present study are validated by comparison to a previously published numerical study and data from field measurements.

Comparison to Other Numerical Simulations

An extensive validation study has been performed to reproduce the results of Blocken [10] for a simple cubic building, with a side length of 10 m, subject to undisturbed wind with an exponential velocity profile (see Eq. (2.4) on page 31). Figure 3.4 shows a schematic of this cubic building.

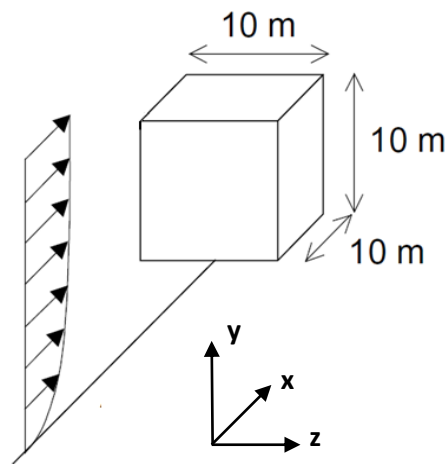


FIGURE 3.4 - SCHEMATIC OF THE CUBIC BUILDING [10]

In reference [10], which is the basis of the current validation study, catch ratio values are reported at six locations on the upper half of the windward facade for different wind speeds, wind angles and rainfall intensities. The situation of the whole facade is also shown as catch ratio contours for one wind speed (normal to the facade) and rainfall intensity. Representative data, for $U_{10}=10$ m/s and $\alpha_p=0.15$, from the six monitored points as well as the mentioned distribution are compared in this section. The results have proven to be in very good agreement with the validation reference.

Reference [10] does not provide information on the size of the area represented by each of the points. The results presented in this section are calculated for $0.2 \text{ m} \times 0.2 \text{ m}$ cells considering the

used raindrop injection density. In the limit of cells approaching *points* infinitesimally, the effect of the cell size on the catch ratio value at individual points is expected to vanish.²

Figures 3.5 and 3.6 show catch ratio versus rainfall intensity at the top corner and top center points of the windward facade, respectively. Catch ratio values based on both area calculation methods discussed in section 2.4.2 are presented here. Catch ratio data from reference [10] are calculated based on an area calculation method similar to the *Convex Hull* method.

As seen in Figs. 3.5 and 3.6, the difference in catch ratio values varies from position to position and for different rainfall intensities. For instance, for a moderate rainfall intensity of $R_h=5$ mm/hr, while the Rectangle method seems to work better at the corner point (5% deviation from literature data, versus 39% deviation of the Convex Hull), under the same rain conditions, the Convex Hull method works better at the center point (5% versus 22% discrepancy). On average, the Convex Hull method is within 31% and 5% of the reference data at points 1 and 2, respectively. The average differences between the Rectangle method results and those of reference [10] are 31% at position 1 and 18% at position 2.

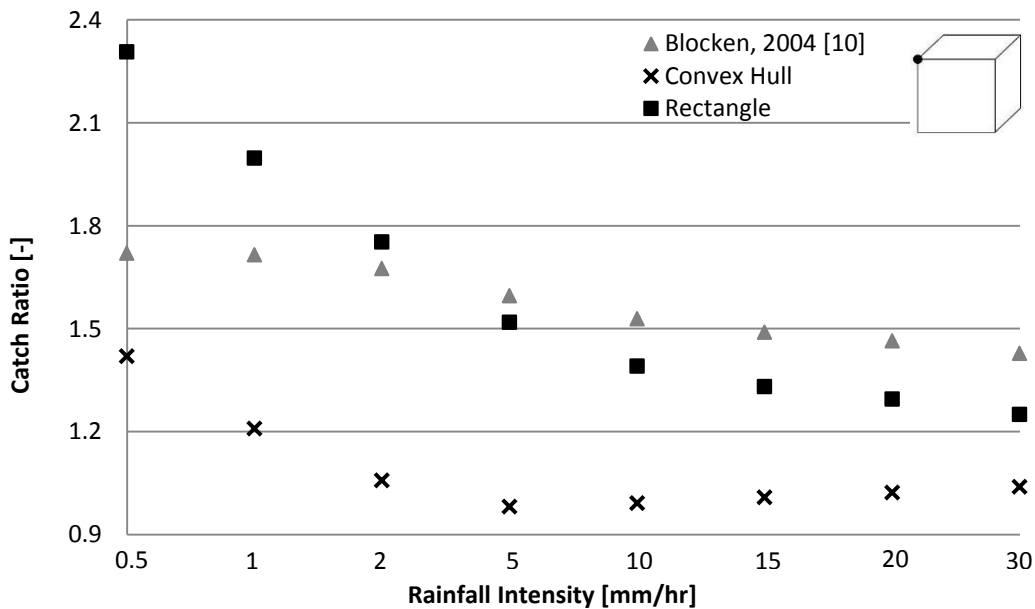


FIGURE 3.5 – CATCH RATIO VS. RAINFALL INTENSITY AT TOP CORNER OF THE WINDWARD FACADE OF THE CUBIC BUILDING ($U_{10}=10$ m/s)

² For a more information on “cell size,” see Section 2.4.2 and Appendix B.

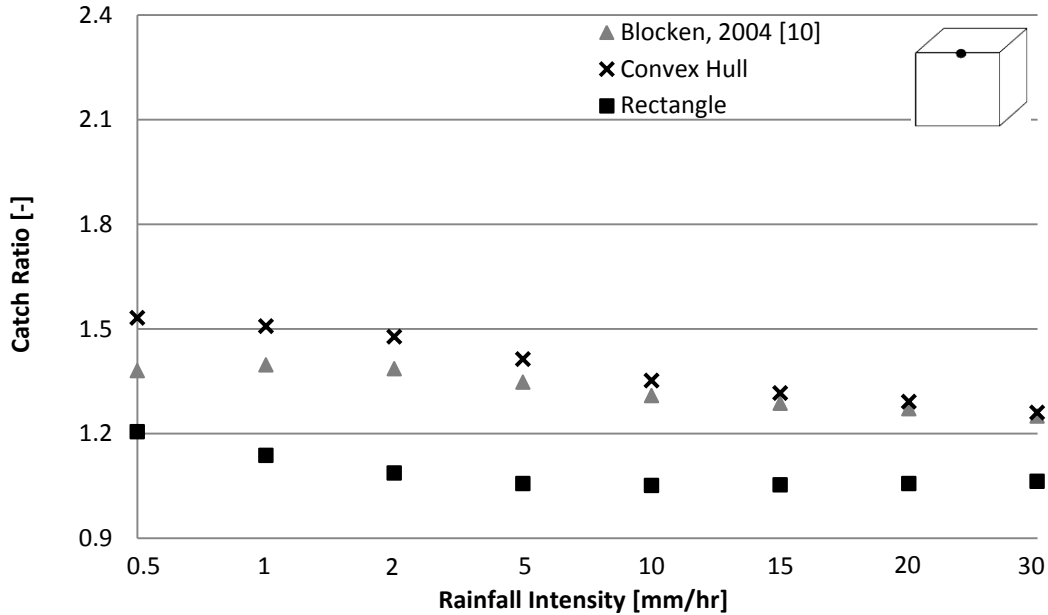


FIGURE 3.6 – CATCH RATIO VS. RAINFALL INTENSITY AT THE TOP CENTER POINT OF THE WINDWARD FAÇADE OF THE CUBIC BUILDING ($U_{10}=10$ m/s)

Differences in the CFD solution of the wind flow, area calculation methods, and the raindrops drag laws are the main reasons of the discrepancies between the results of the current study and reference [10]. Determining the exact share of each factor is difficult. However, since the discrepancy is largest (up to ~40%) at the corner point (Fig. 3.5) and for lower rainfall intensities, which correspond to a majority of small drag-driven raindrops, it is suspected that the difference in the drag law and the numerical solution of the wind flow are the dominant factors.

Figure 3.7 shows catch ratio contours over the windward facade of the cubic building under a normal wind with $U_{10}=10$ m/s and a low rainfall intensity of $R_h=1$ mm/hr. The overall distribution resulted from the present numerical scheme seems to be in good agreement with published results of Blocken [31]. In addition to the aforementioned sources of discrepancy between the results, different data smoothing and contour generation algorithms can also contribute to the difference between these contours. More details on how the contours presented in this work are generated can be found in Chapter 4. Note the pronounced discrepancies of these contours near the edges and corners and the closer agreement in the middle of the facade. This is further evidence that differences in the drag law and CFD of the wind flow are most likely the primary reason of the observed discrepancies.

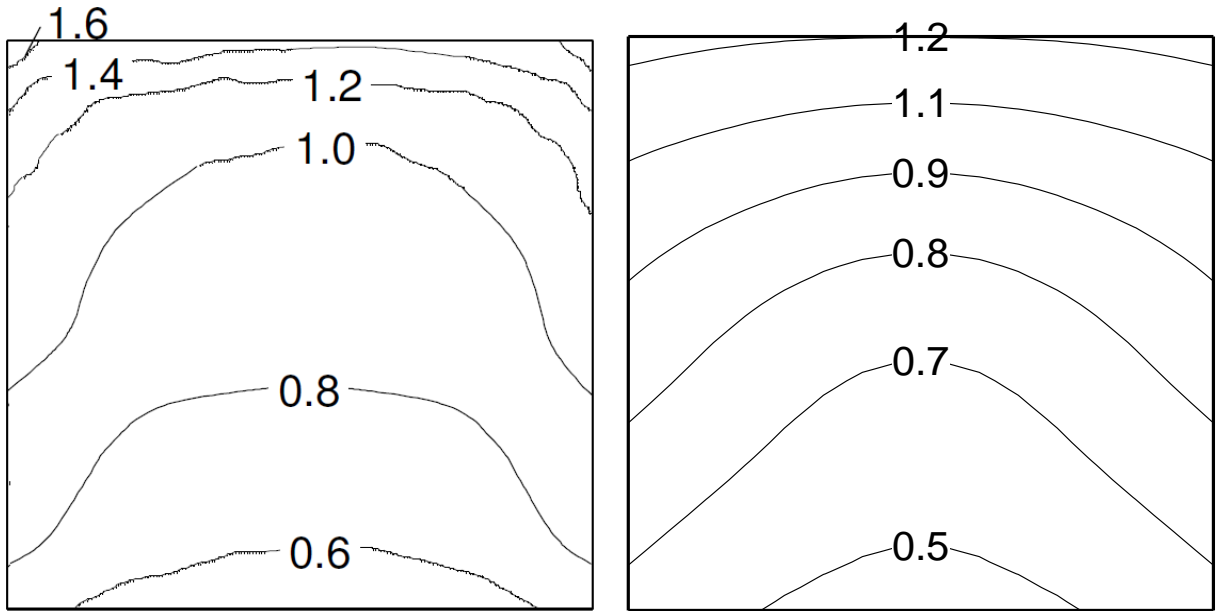


FIGURE 3.7 – CATCH RATIO CONTOURS ON THE WINDWARD FACADE ($\theta=0$, $U_{10}=10$ m/s, $R_r=1$ mm/hr)
LEFT: BLOCKEN [31], RIGHT: THE PRESENT STUDY

Comparison to Field Measurements

The validation study presented in the previous section shows the results of the present numerical study to be in good agreement with the results of other numerical studies from the literature. However, as for any numerical work, further validation, based on experimental data, is also needed.

The developed numerical scheme is evaluated for a test building in Vancouver, Canada under a number of selected wind and rain conditions. The test building is hereinafter referred to as the *Cassier* building. A set of measured WDR data on this building from 2007-2009 are available [64]. In this study, a 6 hour period of wind approaching the East facade of the building in the normal direction is chosen. Wind speed and rainfall intensity data corresponding to this period are averaged using a weighted averaging technique based on rainfall intensity, originally proposed by Blocken [10] and used as boundary conditions of the numerical model. A velocity profile exponent of 0.25 is used to represent the moderately obstructed surroundings of the building [55]. Further details on data analysis as well as the CFD simulation are presented in Appendix C.

Figure 3.8 shows the catch ratio values calculated based on the measurements and predicted by numerical simulation at three locations along the South-East edge of the building. The comparison suggests good agreement (~10-20% difference) between the results, considering all the uncertainties associated with both the measurements and the numerical modeling.

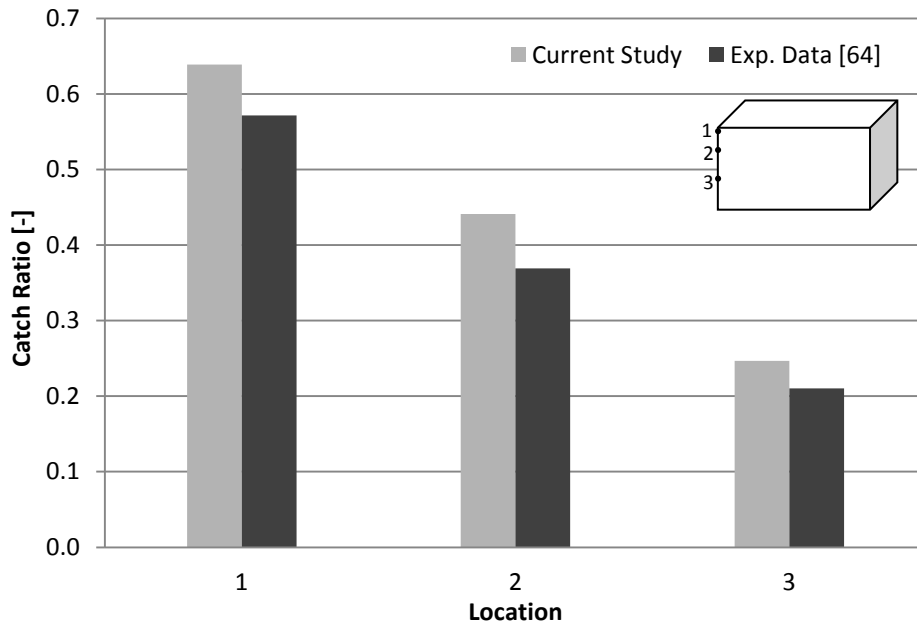


FIGURE 3.8 – CATCH RATIO VALUES ALONG THE SOUTH-EAST EDGE OF THE CASSIER BUILDING ($U_{10}=4.5$ m/s, $R_h=2.3$ mm/hr)

3.3. Sources of Error

The numerical solution errors that occur in every numerical simulation include round-off error, iterative convergence error, and discretization error, which corresponds to errors from discretizing both the domain and the boundary conditions. The numerical error due to machine accuracy is obviously another inherent source of error of any numerical simulation. In addition, there are certain errors introduced to the solution by the models used and the assumptions made. In this section, an estimation of the discretization error is given using Richardson extrapolation method [65]. Subsequently, the criteria for iterative convergence of the solution and major sources of modeling errors in the numerical simulation of WDR are briefly discussed.

3.3.1. Discretization Error

By converting the governing differential equations into a system of algebraic equations, *i.e.* discretizing the system, a certain error, known as *discretization error*, is introduced. Discretization error also occurs due to the discretized implementation of the boundary conditions. Discretization error is the difference between a numerical solution of the discretized equations and the exact solution of the continuum partial differential equations.

As discussed by Roy [62], there are two main reasons for evaluating the discretization error. The first reason is to obtain an assessment of the discretization error associated with a given solution, which might be needed during analysis of simulation results or for a model validation study. The second reason is to derive a *grid adaptation* process.

The method used in this work for estimating the discretization errors is based on Richardson extrapolation [65] and requires numerical solutions on two or more meshes with different levels of refinement. These numerical solutions are used to obtain a higher-order estimate of the exact solution. This estimate of the exact solution can then be used to estimate the error in the numerical solutions. This is an *a posteriori* method and is the most popular extrapolation-based error estimator [62].

Separate grid studies have been performed for each of the two different buildings that are studied in this work. The grid convergence index is calculated based on the relations given in reference [66]. A summary of these calculations are presented in Tables 3.1 and 3.2. The associated discretization errors are shown to be substantially small (<5%).

For the cubic building, pressure coefficient values area-weighted averaged over the windward facade of the building, with $U_{10}=5$ m/s wind approaching in the normal direction, are used as the key field variables. For the Cassier building, specific catch ratio ($d=1.4$ mm) values on the East facade (near the North-East corner) of the building, calculated under a 45° oblique wind with $U_{10}=5$ m/s, are used. Horizontal and total velocity magnitude profiles on vertical and horizontal lines upstream of the buildings, obtained from different grid sizes, are also compared. Figures 3.9 and 3.11 provide a visual comparison of these velocity profiles. The differences between the results obtained from different grid levels tend to be larger near the ground and in the vicinity of the turbulent boundary layer, but obviously small overall.

TABLE 3.1 – GRID CONVERGENCE PARAMETERS (CUBIC BUILDING)

Number of control volumes	Nominal grid size ³ [m]	Refinement ratio	Field variable (C_p)	Grid Convergence Index
941607	1.30	-	15.04	5%
534319	1.56	1.21	14.84	
198285	2.17	1.39	15.07	

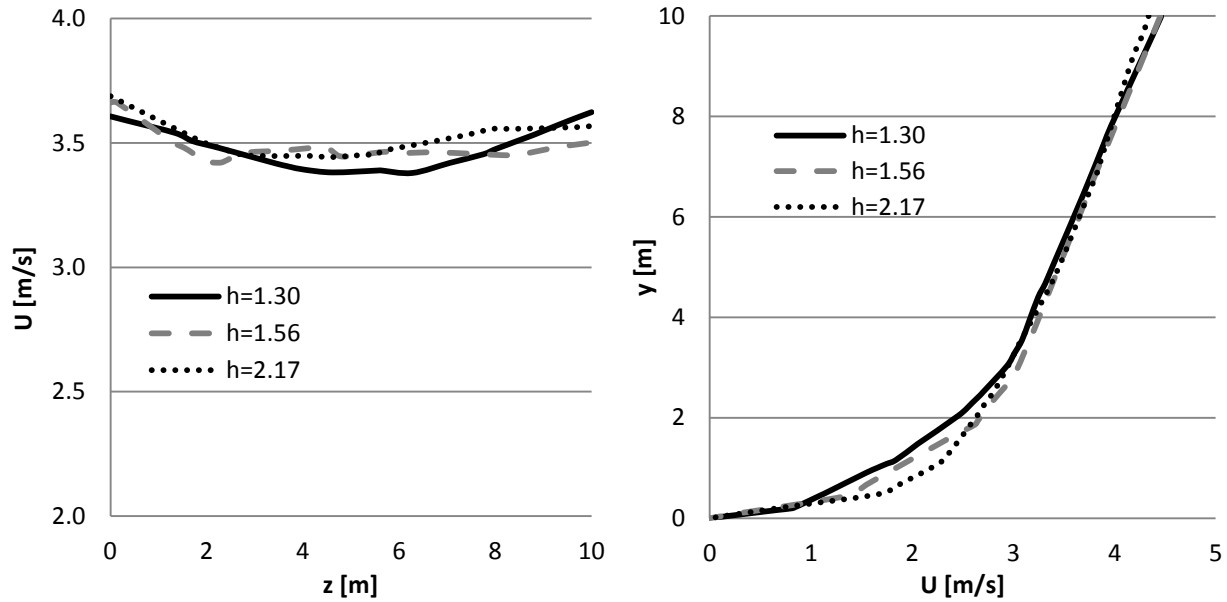


FIGURE 3.9 – HORIZONTAL VELOCITY MAGNITUDE ALONG A HORIZONTAL ($y=5$) (LEFT) AND A VERTICAL ($z=0$) (RIGHT) LINE 10 m UPSTREAM OF THE CUBIC BUILDING ($U_{10}=5$ m/s)

Figure 3.10 shows the distribution of 1 mm raindrops on the facade with raindrop trajectories calculated with different CFD grids. These raindrops are all injected on the centerplane of the facade ($z=0$) and are driven to the cubic building by a normal $U_{10}=2$ m/s wind. Particle trajectories are expected to be symmetric under such symmetric flow conditions. However, raindrop trajectories, and consequently the distribution of catch ratio on the facade, show a deviation from fully symmetric patterns. It can be seen in Fig. 3.11 that coarser grids lead to

³ Since non-uniform grids are used in this study, h is an *equivalent* grid size calculated as

$$h = \left[\frac{1}{N} \sum_{i=1}^N (\Delta V)_i \right]^{1/3}$$

where $(\Delta V)_i$ is the volume of each control volume and N is the total number of control volumes [66].

larger deviations from a symmetric deposition of the raindrops. It is deduced from similar numerical tests that the observed deviation from a symmetric distribution of catch ratio for symmetric flow conditions is due to numerical errors mainly.

A *safety factor* of $F_s=1.3$, as suggested by Roache [67], is used in the discretization error estimations to achieve a 95% confidence interval.

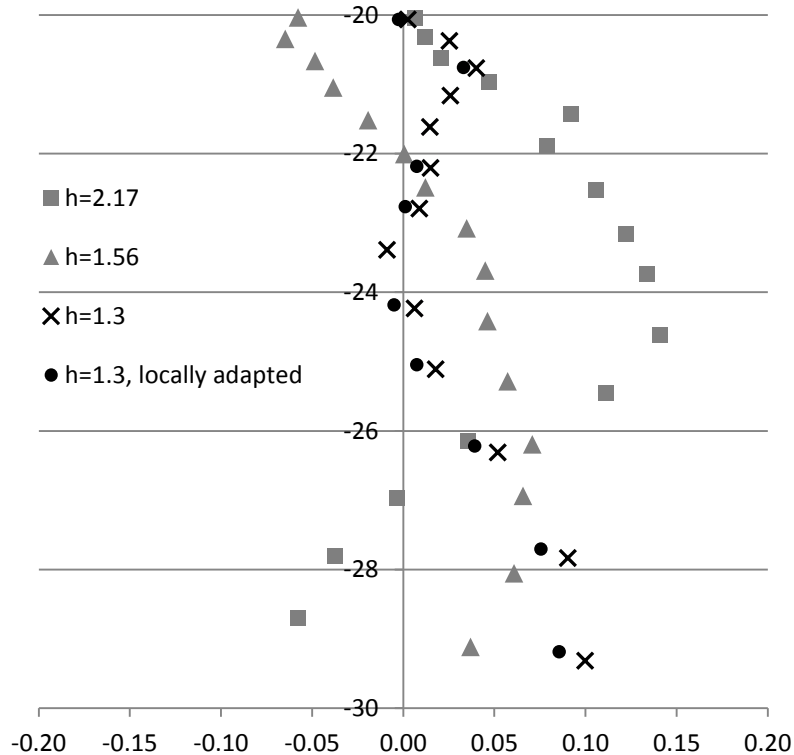


FIGURE 3.10 - DISTRIBUTION OF 1 mm RAINDROPS NEAR THE CENTERLINE OF THE WINDWARD FACADE OF THE CUBIC BUILDING, CALCULATED AT DIFFERENT GRID LEVELS ($U_{10}=5$ m/s)

Whether the specific catch ratio is an appropriate parameter for monitoring grid convergence is questionable to some extent. There are two potential sources of error involved in the catch ratio calculations, other than discretization error; numerical error introduced by Lagrangian particle tracking and the error due to the curve-fitted drag law. Nevertheless, as long as the same numerical scheme and the same drag law are used for integrating the ODE of raindrop motion, the relative difference between catch ratio values can be attributed to the difference in grid size, *i.e.* discretization error, only. When flow-field variables, such as static pressure on the building and wind velocity at a number of different positions upstream of the building, are tested for this

purpose, they all have yielded discretization errors smaller than or equal to the ones reported above. After this Richardson-extrapolation based grid convergence analysis, the grids are further refined locally during the solution based on different parameters such as pressure gradients, velocity component gradients and, most importantly, y^+ .

TABLE 3.2 – GRID CONVERGENCE PARAMETERS (CASSIER BUILDING)

Number of control volumes	Nominal grid size [m]	Refinement ratio	Field variable ($\eta_{d=1.4}$)	Grid Convergence Index	
2607354	1.42	-	0.336	9%	-
1190449	1.84	1.30	0.350		7%
564701	2.36	1.28	0.332	-	-
268333	3.03	1.28	0.299		

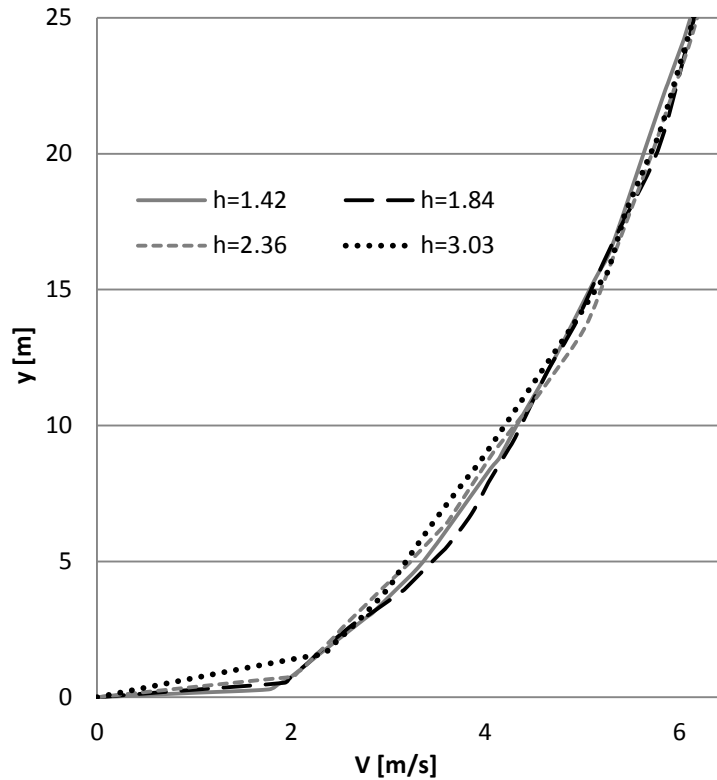


FIGURE 3.11 – VELOCITY MAGNITUDE PROFILE ALONG A VERTICAL LINE ON THE 45° PLANE, 5 m UPSTREAM OF THE CASSIER BUILDING ($U_{10}=5$ m/s)

3.3.2. Iterative Convergence Error

Iterative convergence error arises due to incomplete iterative convergence of the numerical solution of a discrete system. Residuals at each iteration, which are considered a much better measure of convergence than the difference between successive steps [62], are used as the main convergence criterion. Residuals are calculated by plugging the current numerical solution into the discretized form of the equations. The residuals should obviously approach zero (within machine accuracy) as the solution converges.

For the simulations presented in this work, residuals of the six governing equations (continuity, x-, y- and z-velocity, k and ϵ) are monitored with the convergence criterion being a reduction of at least four orders of magnitude. Different flow parameters, such as the pressure coefficient on a wall or averaged velocities on lines or planes upstream of the building, are also monitored to ensure a stable converged solution. Default relaxation factors were used in all the CFD solutions.

3.3.3. Modeling Errors

In addition to the numerical errors discussed in the previous sections, there are other errors in numerical simulations, including the present work, that originate from the *models* used and their underlying assumptions. Although there are certain methods for quantifying modeling errors, the descriptive discussion presented here suffices considering the scope of this thesis.

Turbulence Modeling

The highly turbulent wind flow plays the key role in WDR. Treatment of the wind flow is therefore crucial in numerical simulation of WDR. Nevertheless, “the understanding of the physics of turbulence remains incomplete [...and] sets the *upper limit* to the current understanding of the *more complex* particle-laden turbulent flows” [48].

However, the approximate solutions of wind flow obtained based on simple turbulence models, such as the k - ϵ model, fortunately have proven to be within acceptable accuracy for practical applications [51, 53]. On the other hand, the Lagrangian tracking of the raindrops demands significant computational power and time. Hence, treating the wind flow using demanding techniques such as Large Eddy Simulation (LES) does not seem feasible considering the available computational resources and time.

As related to turbulence, a *secondary* modeling error also arises by neglecting the turbulent dispersion of the raindrops, which has been discussed in more detail in section 2.2.6.

Undisturbed Wind Velocity Profile

The profile assumed for the speed of the undisturbed wind approaching the building is one of the key assumptions of this simulation. The exponential profile used in this work is proposed by Blocken [10] and has been modified and validated in the Atmospheric Boundary Layer (ABL) literature (see references [10], [30] and [68] for example). However, considerable simplification is embedded in this simple profile as the turbulent boundary layer of the wind flow and the obstruction it experiences before hitting the building are represented by two constants (U_H and α_p) only. The roughness height assumed for the surroundings of the building and the inlet kinetic energy (k) and dissipation rate (ϵ) boundary conditions introduce further errors.

Discrete Phase Modeling of Rain

As discussed in Chapter 2, raindrops are treated as discrete particles with the interaction between them, as well as their effect on the wind flow, being neglected. The error introduced by this simplified approach, nevertheless, is suspected to be small in comparison to the dominant modeling errors, *i.e.* the errors associated with modeling the turbulence.

In addition, there are certain numerical errors that originate from the numerical integration of the ODE of the raindrops motion. Nevertheless, these errors are considered essentially small since the used integration scheme is a fourth order method, while the numerical solution of the PDE of the wind flow is of second order accuracy. It is noteworthy, however, that the accumulation of the integration errors at successive time steps (the “pollution error”) could be considerable.

Raindrop Drag Law

As extensively discussed in section 2.3.4, the drag law used for the raindrops in the present work is based on a curve-fit to a set of experimental data. In addition to the measurement errors associated with the experimental data, there are errors introduced by the curve fitting process and extrapolating beyond the range of the measured values.

Since the drag force is a key parameter in calculating the raindrop trajectories, and hence catch ratio values, the error associated with it is considered as one of the important sources of uncertainty in the results. As mentioned previously, the discrepancies observed between the

current results, the previous works and the measurements are partly due to the different drag laws and their associated errors.

Raindrop Size Distribution

The probability density function used to determine the frequency of the raindrops with a certain diameter in a given rainfall event is based on measured data. These measurements are presented as (rainwater) volume fraction with respect to the air. There are, therefore, certain measurement errors, as well as errors in the empirical correlation extracted from those measurements, that would propagate through the calculations, specifically when integrating specific catch ratios to compute total catch ratio values.

Note that the volume-based expression from reference [60] is converted to a flux-based basis by a function that involves raindrop terminal velocities.⁴ Hence, there are even further uncertainties in the flux-based probability density function that has been used.

Furthermore, there are potential errors associated with using the results of field measurements of raindrop size distribution performed in climates different from that of where the building is located. The amount and relative significance of such errors are not known.

The Streamtube Assumption

As discussed in section 2.4, the fundamental assumption that reduces the calculation of catch ratios to a calculation of (injection and wetted) areas, is that the raindrops form *closed* streamtubes. In other words, the raindrop trajectories do not intersect and the rainwater content of a streamtube remains constant. Numerical tests have shown this assumption to be acceptably accurate. However, these streamtubes may be highly distorted (especially when small raindrops are driven by high-speed winds to the corners and edges of a building) and raindrop trajectories might cross each other occasionally.

⁴ See section 2.3.5.

CHAPTER 4

Results & Discussion

The results of the numerical simulations are presented in this chapter. The focus of the study has been a simple cubic building mainly. There are two reasons for this choice. First, that there are published numerical studies on a similar geometry in the WDR literature (reference [10]) that provide a basis for validation of the present numerical simulations (see Chapter 3). Second, the simplicity of the building, and consequently the flow field around it, would make it easier and less time consuming to examine different overhangs, under a number of different wind and rain conditions. In addition, it is expected that the effects of overhangs would be easier to assess on such a simple building. The performance of overhangs with different widths is investigated under different wind speeds, wind angles and rainfall intensities. A second building, representing a test building for which field measurements of WDR are available, is also studied for a few combinations of overhang size and wind and rain conditions.

Results are presented as catch ratio contours over the windward facades and an overhang *effectiveness index* that has been introduced in order to quantify the effectiveness of the overhangs. Local catch ratio values, specific catch ratio contours and graphs showing the distribution of raindrops on the facade are also used to provide insight when discussing the findings.

4.1. The Cubic Building

The 10 m cubic building introduced in section 3.2 is studied with different overhangs added as extensions of the building roof. Three rectangular overhangs are tested with widths (x) of 30 cm, 60 cm and 90 cm. All these overhangs are horizontal (zero pitch angle), 15 cm thick (y) and 10 m long (z). Figure 4.1 shows a schematic of the cubic building with added overhang.

Table 4.1 summarizes the information concerning the computational domain size and discretization. An undisturbed wind with an exponential speed profile (see section 2.2.3) approaches the building with the wind angle θ measured clockwise with respect to the normal vector of the plane containing the windward facade, as depicted in Fig. 4.1. The boundary

conditions are discussed in detail in Chapter 2. Here, the boundary conditions of the CFD solution of wind flow around the cubic building are summarized in Table 4.2.

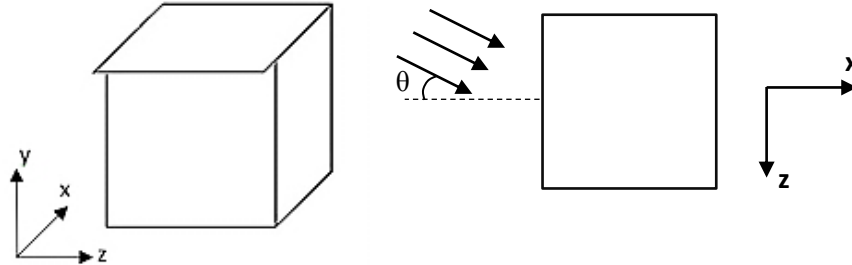


FIGURE 4.1 - SCHEMATIC OF THE CUBIC BUILDING ISOMETRIC (LEFT) AND TOP (RIGHT) VIEWS

TABLE 4.1 – COMPUTATIONAL DOMAIN SIZE & DISCRETIZATION FOR THE CUBIC BUILDING

Domain Length (x)			310 m
Domain Height (y)			60 m
Domain Width (z)			110 m
Surface Mesh	Size	Domain sides	3 m
		Building walls	0.3 m
	Type	Quadrangle	
Volume Mesh	Number of CV's		$\sim 6 \times 10^5$
	Type		Tetrahedral

TABLE 4.2 – SUMMARY OF BOUNDARY CONDITIONS FOR THE CUBIC BUILDING

Boundary		Inlet	Sides	Top	Bottom	Outlet	Building
Condition	Momentum	Direction: Normal to boundary Magnitude: $U_{10} = 2, 5 \text{ \& } 10 \text{ m/s}$ $\alpha_p = 0.15$	Symmetry	Symmetry	No slip, impermeable	Backflow pressure ($p_0 = 0$, gauge)	No slip, impermeable
	Turbulence	k : Eq. (2.5) ϵ : Eq. (2.6)			Roughness height ($K_s = 0.03 \text{ m}$)	$k_{\text{backflow}} = 1 \text{ m}^2/\text{s}^2$ $\epsilon_{\text{backflow}} = 1 \text{ m}^2/\text{s}^3$ (default settings)	Roughness height ($K_s = 0$)
	DPM	-	-	-	Trap	-	Trap

4.1.1. Catch Ratio Contours

The main parameters that affect the effectiveness of the overhang are the overhang size, wind angle, wind speed and rainfall intensity. The effects of each factor are examined while the other three are fixed. Winds approaching the windward facade at 0° (normal), 30° , 45° and 60° angles are studied. Three wind speeds of 2, 5 and 10 m/s representing low, moderate and high speed winds and three rainfall intensities of 2, 5 and 10 mm/hr, representing low, moderate and high intensities of rainfall, are studied.

In this section, catch ratio contours over the windward facade of the cubic building are presented for different combinations of the mentioned variables. In these contours, the horizontal and vertical axes are in z - and y -direction respectively. The left border ($z=-5$) corresponds to the windward edge (the *leading edge*) of the facade. All the catch ratio calculations are performed for $0.3 \text{ m} \times 0.3 \text{ m}$ cells. Contours are generated after smoothing catch ratio values at the cells using algorithms such as *Negative Exponential* and *Losses* in SigmaPlot [69].

When the wind is approaching the building in the normal direction, *i.e.* in symmetric flow conditions, both the raindrop distribution patterns and the catch ratio contours are expected to be symmetric. Results, however, show otherwise. The observed slight deviations from symmetry are suspected to be due to asymmetry in the flow field (especially for high wind speeds), numerical errors in the CFD solution of the wind flow and the numerical errors associated with the catch ratio calculations and contour generation. This has been discussed in section 3.3.1 too.

Catch ratio contours for normal wind with a moderate speed of $U_{10}=5 \text{ m/s}$ and under a moderate rainfall intensity of $R_h=5 \text{ mm/hr}$ are shown in Fig. 4.2. Buildings with different overhang widths are compared to the case without an overhang. It can be seen that the introduction of the overhang changes general wetting patterns of the facade, as well as the local catch ratio values. For instance, note how after the 30 cm overhangs is added, the contour lines separate at the $y>7$ and $-1<z<1$ region. This *saddle point* tends to occur at lower positions as the overhang width increases. The *separated* contour lines correspond to different catch ratio values for each case. For example, with a 30cm overhang the saddle point occurs between the 0.35 lines, while for 60cm and 90cm overhangs, the separated lines are the 0.3 and 0.25 contour lines respectively. Under these wind and rain conditions, the wider overhangs provide much better protection at the

upper half of the facade. On the other hand, introduction of the overhang has almost no effect on the lower half.

Figure 4.3 shows the catch ratio contours on the windward facade for the wind speed of $U_{10}=5$ m/s, a moderate rainfall intensity of $R_h=5$ mm/hr and a wind angle of $\theta=45^\circ$. Overhangs seem to change the wetting patterns significantly under such oblique winds too. As in the case of a normal wind, the protective effect of the overhang increases with its width. The overhangs are also more effective on the upper half of the facade and away from the windward edge ($z=-5$). The bottom right corner of the facade ($0<y<5$, $0<z<5$) is almost not influenced by the overhang at all. In addition, around the center of the windward edge ($z\sim-5$ and $-5<y<-4$), the 60 cm overhang has led to a slightly increased ($\sim 4\%$) catch ratio compared to the case with the 30 cm overhang. This increase, which might be due to numerical errors too, is not observed for the 90 cm overhang. The increased protection provided by the overhang as its size increases, while quite significant from 30 cm to 60 cm, diminishes from 60 cm to 90 cm.

Figure 4.4 shows the distribution of catch ratio on the windward facade under different rainfall intensities. These results are for normal wind direction and the moderate wind speed of $U_{10}=5$ m/s. Without an overhang, higher catch ratios are observed at the top corner under the low rainfall intensity. For example, compare 0.65 under $R_h=2$ mm/hr with 0.6 and 0.55 under $R_h=5$ mm/hr and $R_h=10$ mm/hr respectively. However, the lower portions of the facade have slightly larger catch ratios under higher rainfall intensities. The difference between low ($R_h=2$ mm/hr) and moderate ($R_h=5$ mm/hr) rainfalls is also greater than the difference between moderate and high ($R_h=10$ mm/hr) intensities. Overall, with or without the overhang, the rainfall intensity does not have a significant effect on the wind-driven wetting of the facade. In addition, the performance of the overhang, at least at moderate wind speeds such as 5 m/s, seems to be independent of the rainfall intensity.

The effect of wind speed is shown in the contours of Fig. 4.5. In these contours, the rainfall intensity and the overhang width are fixed at 5 mm/hr and 60 cm respectively and the wind approaches the building in the normal direction. Wind speed seems to play a larger role than rainfall intensity. The effectiveness of the overhang also varies under different wind speeds. Based on these results, a 60 cm overhang helps protect the upper half of the facade from WDR loads in low, moderate and high wind speeds. Yet, in terms of reducing catch ratio compared to

the case without an overhang, the 60 cm overhang appears to be much more effective under the low wind speed of $U_{10}=2$ m/s.

A visual evaluation of the performance of the 60 cm overhang under different wind angles is provided by Figs. 4.6A and 4.6B. In these figures, catch ratio contours on the windward facade of the cubic building subject to a $U_{10}=5$ m/s wind at varying angles and a rainfall intensity of $R_h=5$ mm/hr are presented. It can be seen in these contours that the wind angle has a significant influence on the WDR wetting patterns of the facade. Over the entire facade, the catch ratio decreases significantly as wind angle increases. Under 30° and 45° winds, most of the WDR deposition occurs near the windward edge of the facade. However, with the wind angle further increased to $\theta=60^\circ$, the higher catch ratios move towards the right edge ($z=+5$) of the facade. The 60 cm overhang seems to be well protecting the facade, especially the upper half, under all the wind angles. As observed in the previous cases, the lower half is almost not influenced by the presence of the overhang at all. For oblique winds, the protective effect of the overhang increases as we move away from the windward edge ($z=-5$). The change caused by the overhang in the wetting pattern (the configuration of the contour lines) is obvious for the oblique winds too. As an example, compare the 0.3, 0.15, 0.1 and 0.07 contour lines for 0° , 30° , 45° and 60° wind angles respectively. The variation is similar to the observed trend for different overhang widths under a normal wind (see Fig. 4. 2 and its description).

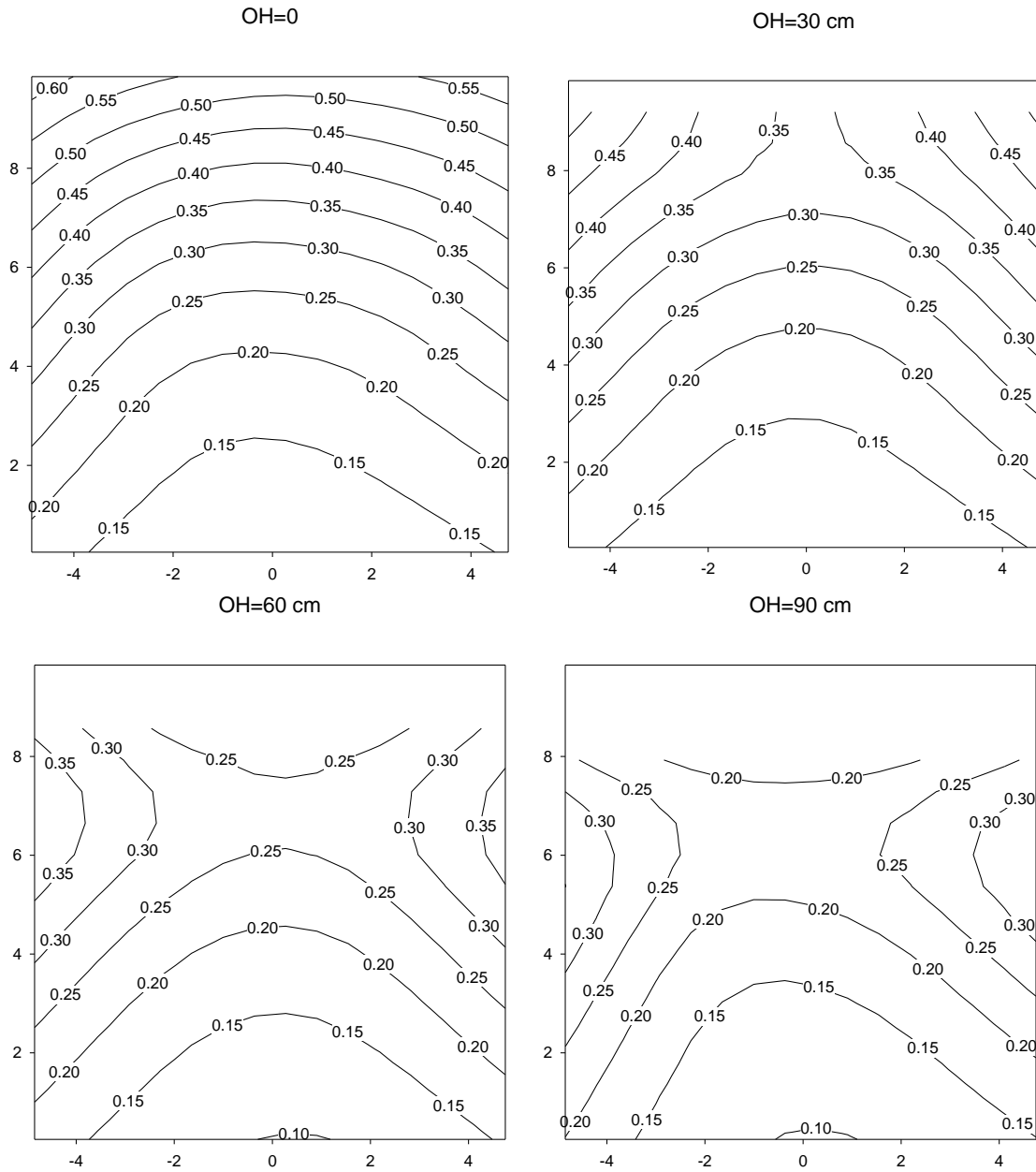


FIGURE 4.2 – CATCH RATIO CONTOURS ON THE WINDWARD FACADE OF THE CUBIC BUILDING WITH DIFFERENT OVERHANGS UNDER A NORMAL WIND ($\theta=0^\circ$, $U_{10}=5$ m/s, $R_h=5$ mm/hr)

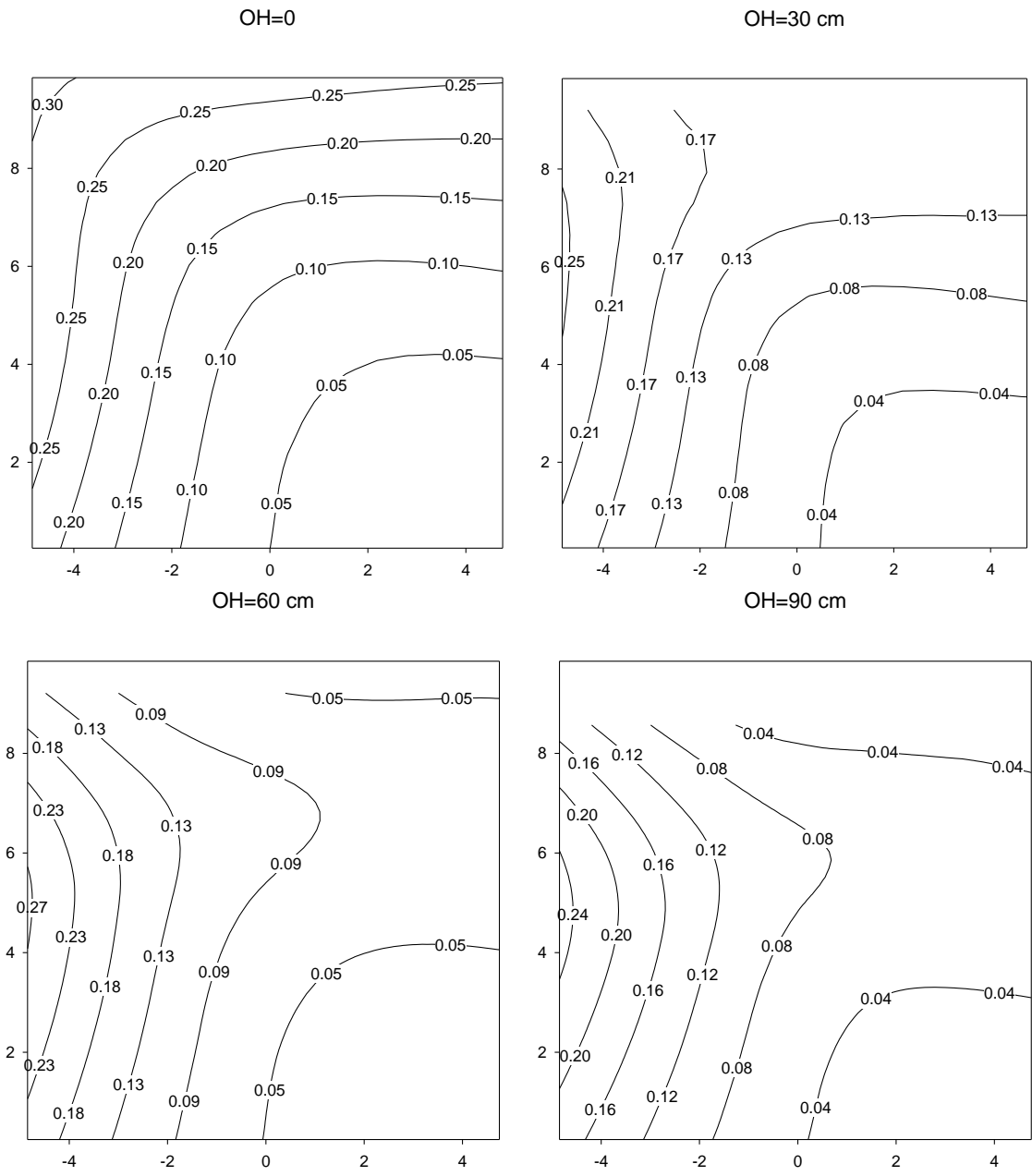


FIGURE 4.3 - CATCH RATIO CONTOURS ON THE WINDWARD FACADE OF THE CUBIC BUILDING WITH DIFFERENT OVERHANGS UNDER AN OBLIQUE WIND ($\theta=45^\circ$, $U_{10}=5$ m/s, $R_h=5$ mm/hr)

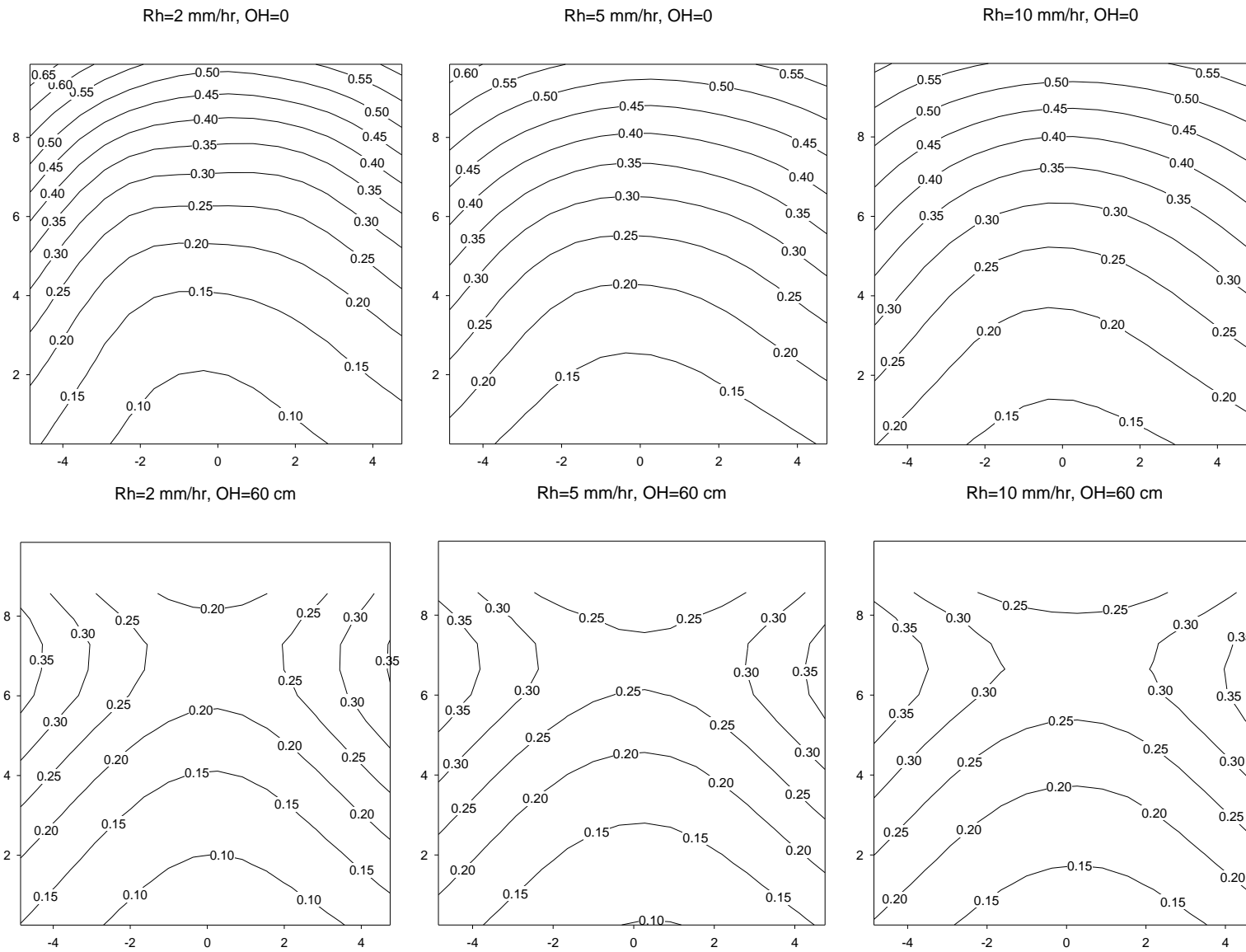


FIGURE 4.4 – CATCH RATIO CONTOURS ON THE WINDWARD FACADE OF THE CUBIC BUILDING UNDER DIFFERENT RAINFALL INTENSITIES, WITHOUT (TOP) AND WITH (BOTTOM) THE 60 cm OVERHANG ($\theta=0^\circ$, $U_{10}=5$ m/s)

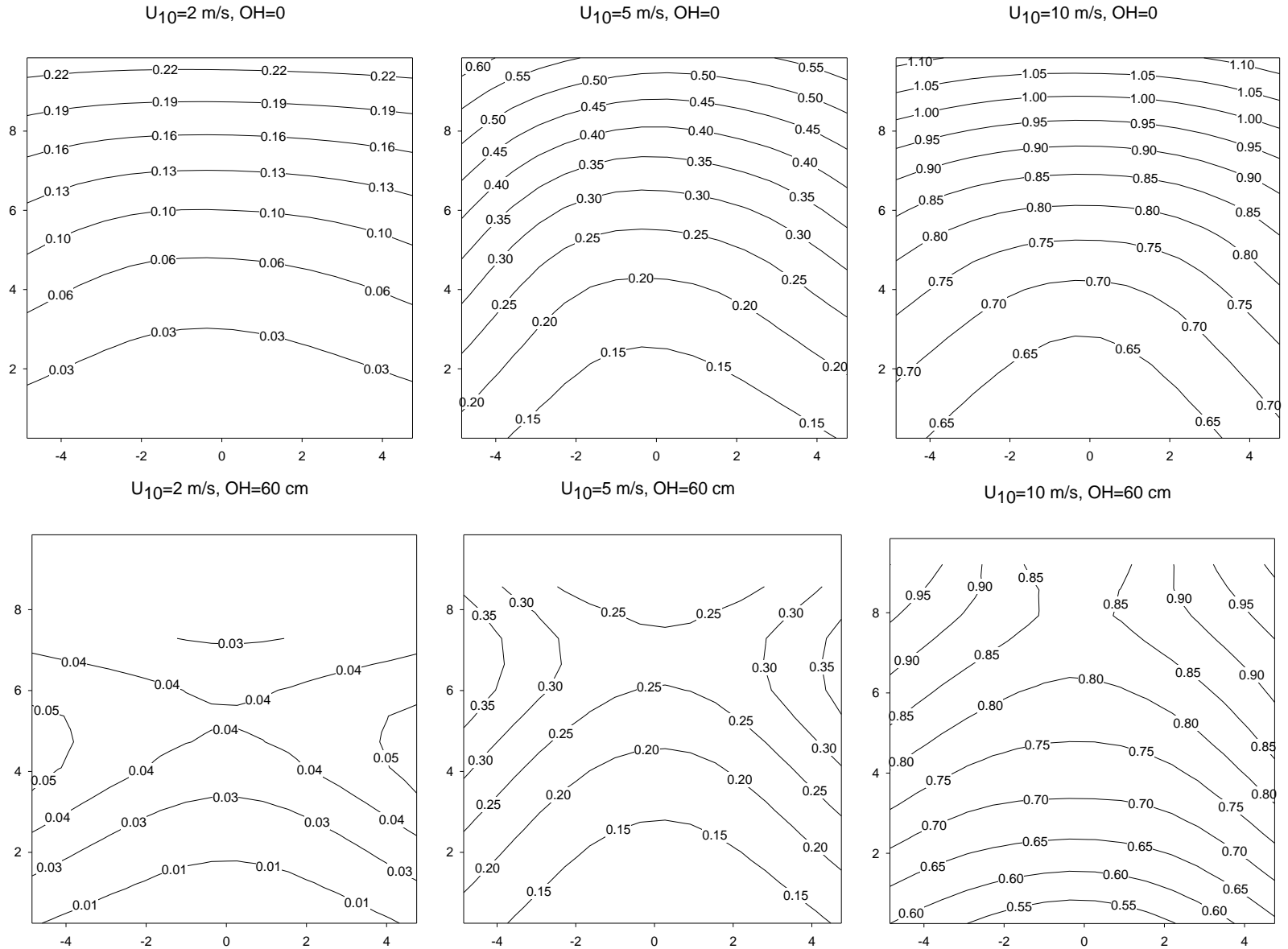


FIGURE 4.5 – CATCH RATIO CONTOURS ON THE WINDWARD FACADE OF THE CUBIC BUILDING UNDER DIFFERENT WIND SPEEDS, WITHOUT (TOP) AND WITH (BOTTOM) THE 60 cm OVERHANG ($\theta=0^\circ$, $R_h=5$ mm/hr)

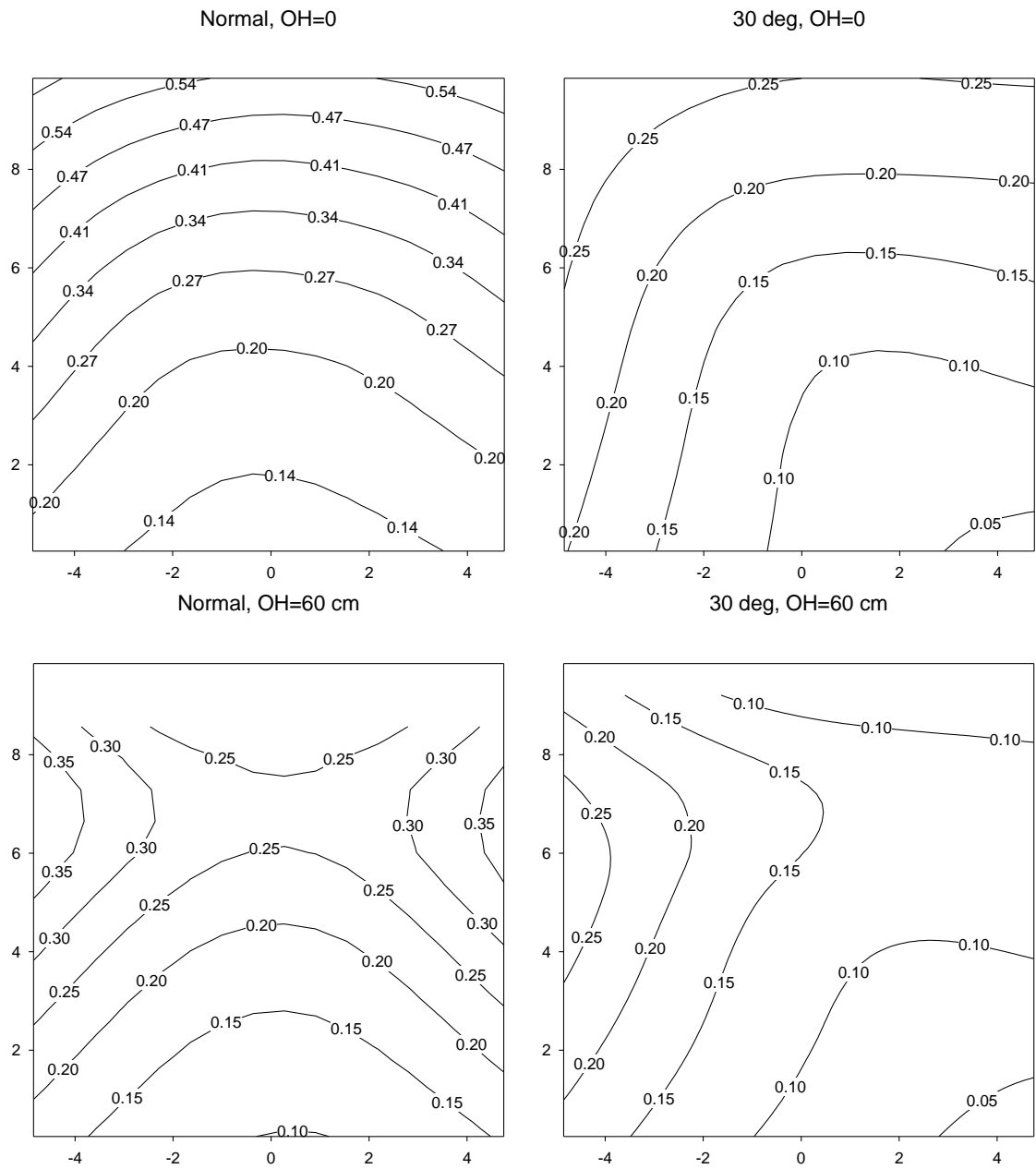


FIGURE 4.6A – CATCH RATIO CONTOURS ON THE WINDWARD FACADE OF THE CUBIC BUILDING WITHOUT AND WITH THE 60 cm OVERHANG UNDER NORMAL AND 30° WINDS ($U_{10}=5$ m/s, $R_h=5$ mm/hr)

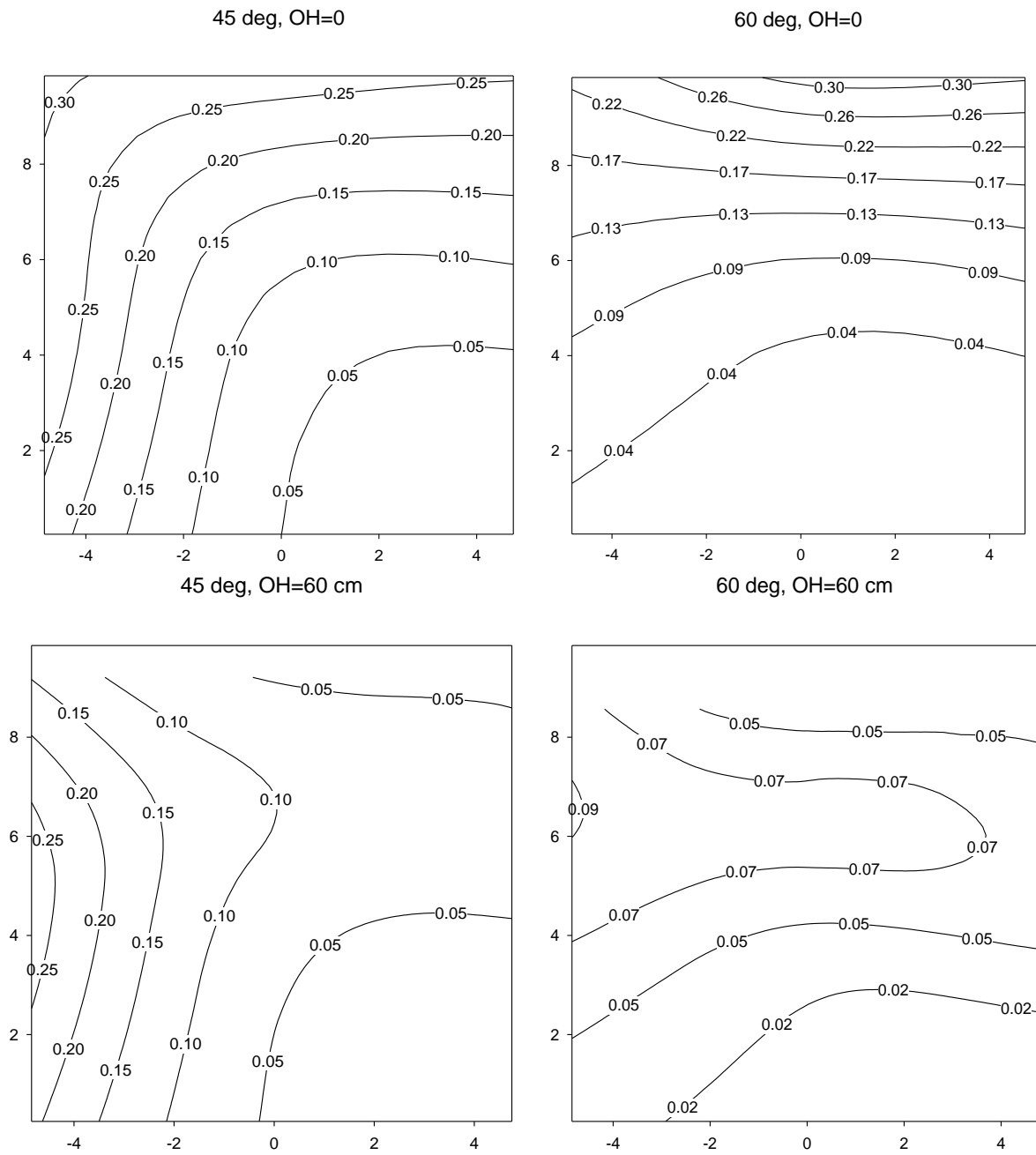


FIGURE 4.6B - CATCH RATIO CONTOURS ON THE WINDWARD FACADE OF THE CUBIC BUILDING WITHOUT AND WITH THE 60 cm OVERHANG UNDER 45° AND 60° WINDS ($U_{10}=5$ m/s, $R_h=5$ mm/hr)

4.1.2. Effectiveness Index

In order to quantify the protective effect that an overhang may have, an effectiveness index (δ) is defined as the percentage change between the area-weighted averages of the local catch ratio values without and with the overhang, as described by Eq. (4.1).

$$\delta = \left(\frac{\bar{\eta} - \bar{\eta}_{OH}}{\bar{\eta}} \right) \times 100 \quad (4.1)$$

In this equation, $\bar{\eta}$ and $\bar{\eta}_{OH}$ designate the average catch ratio values without and with the overhang respectively. The average value is calculated based on Eq. (4.2), with the cell area as the weighting function.

$$\bar{\eta} = \frac{1}{\sum_{i=1}^n A_i} \sum_{i=1}^n \eta_i A_i \quad (4.2)$$

The summation index i is the cell number, A_i is the area of the i^{th} cell and n is the total number of the cells over which the average is calculated.

In the case of a constant cell size over the averaging range, Eq. (4.2) is simplified to

$$\bar{\eta} = \frac{1}{n} \sum_{i=1}^n \eta_i \quad (4.3)$$

Calculating the effectiveness index over different areas on the facade could provide insight into the effectiveness of the overhang at different locations. Figure 4.7 shows the portions of the windward facade of the cubic building for which the effectiveness index has been calculated and reported.

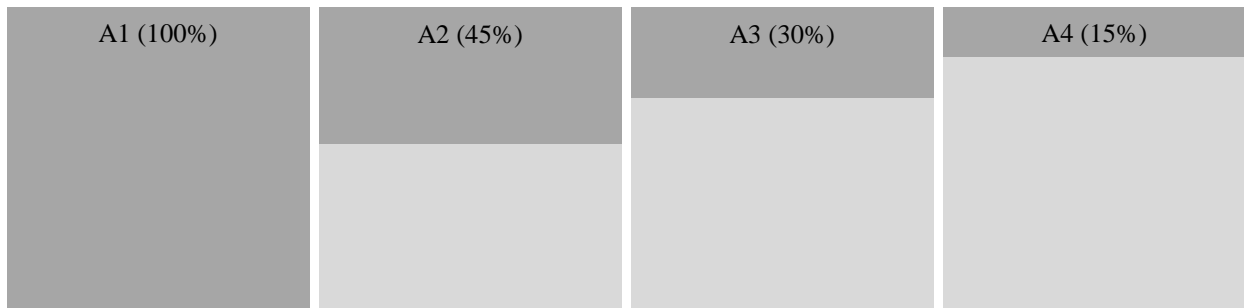


FIGURE 4.7 – EFFECTIVENESS INDEX CALCULATION AREAS ON THE WINDWARD FACADE OF THE CUBIC BUILDING

Table 4.3 shows the percentage of total WDR load on the facade that is deposited in the partial areas introduced in Fig. 4.7. These percentages are calculated, using Eq. (4.4), as the ratio between surface integrals of the catch ratio distribution on the partial area and the whole facade.

$$\tilde{\eta}_i = \frac{\int_{A_i} \eta \, dA}{\int_A \eta \, dA} \quad (4.4)$$

where A and A_i are the total and partial areas on the facade and $\tilde{\eta}_i$ denotes the percentage of total WDR that is deposited on the partial area A_i.

TABLE 4.3 – THE PERCENTAGE OF WDR ON DIFFERENT PARTS OF THE WINDWARD FACADE OF THE CUBIC BUILDING WITH NO OVERHANG

θ [°]	U_{10} [m/s]	R_h [mm/hr]	$\tilde{\eta}$		
			A4	A3	A2
0	2	5	33%	58%	76%
	5	2	30%	52%	68%
		5	28%	48%	65%
		10	26%	46%	63%
10	5	20%	37%	53%	
30	5	5	23%	43%	59%
45			28%	48%	64%
60			41%	66%	81%

The values of $\tilde{\eta}$, as given in Table 4.3, show the concentration of WDR loads on the upper half of the windward façade. It is therefore most critical for the overhang to protect these areas. This table is a quantitative expression of the trends observed in the catch ratio contours presented in the previous section.

Figures 4.8 to 4.11 show the effectiveness index of different overhangs over the areas A1 to A4. The same observations as made from the catch ratio contours can be made from these diagrams. It is hence concluded that the proposed effectiveness index (Eq. (4.1)) is a good quantified measure of the effects of overhangs.

For example, Fig. 4.8 shows that the 90 cm overhang provides the best protection (28% over the whole facade when $U_{10}=5$ m/s and $R_h=5$ mm/hr) compared to the other overhangs (OH=30 cm and 60 cm). It is also seen in the same figure that the effectiveness of all the overhangs increases

as we move toward the top edge of the facade. Note that the upper portions of the facade, especially around the corners, are generally subject to the highest WDR loads. Therefore, it is very important, from a building science point of view, to protect these points from WDR deposition.

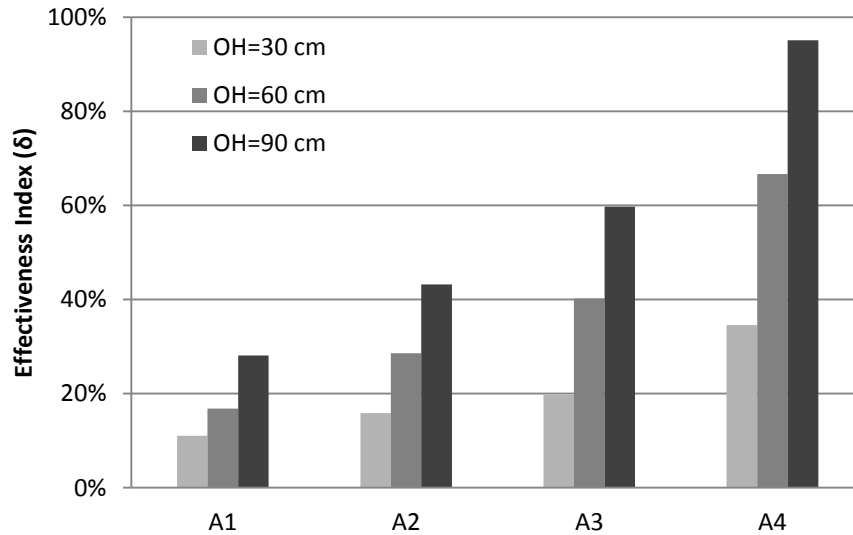


FIGURE 4.8 – EFFECTIVENESS INDEX OF DIFFERENT OVERHANGS OVER DIFFERENT PORTIONS OF THE WINDWARD FACADE OF THE CUBIC BUILDING ($\theta=0^\circ$, $U_{10}=5$ m/s & $R_h=5$ mm/hr)

Figure 4.9 shows that, as seen in the contours of Fig. 4.4, the rainfall intensity has almost no effect on the protection provided by an overhang. Similar to what is understood from the contours, the difference between the low and moderate rainfalls is larger than the difference between the moderate and high intensities of rainfall. Over the top 15% of the facade (A4), the 60 cm overhang has an effectiveness index of 68% under the moderate rainfall intensity of 5 mm/hr and an index of 67% under both moderate ($R_h=5$ mm/hr) and high ($R_h=10$ mm/hr) rainfalls. Further investigation shows that all three overhangs have the same performance under low, moderate and high rainfall intensities.

On the other hand, as understood from the corresponding catch ratio contours (Fig. 4.5), Fig. 4.10 shows the large sensitivity of the effectiveness of the overhang to the wind speed. The 60 cm overhang provides substantially better protection against the rainwater driven by low speed winds. Numerical tests on other overhangs (OH=30 cm and 90 cm) have revealed similar patterns in their performance. This overhang (OH=60 cm) has effectiveness indices of 70% and

100% over the whole facade and the upper 15% of the facade respectively, under a relatively low speed of $U_{10}=2$ m/s.

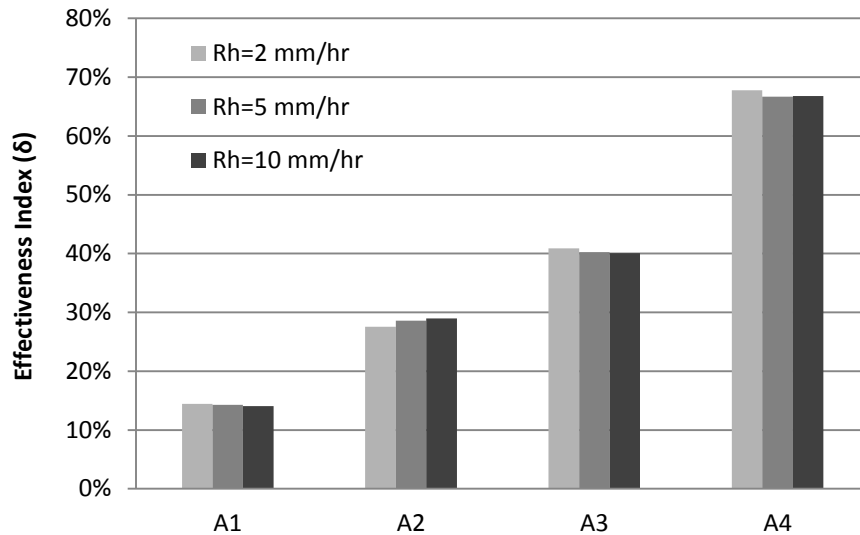


FIGURE 4.9 – EFFECTIVENESS INDEX OF THE 60 cm OVERHANG OVER DIFFERENT PORTIONS OF THE WINDWARD FACADE OF THE CUBIC BUILDING UNDER DIFFERENT RAINFALL INTENSITIES ($\theta=0^\circ$, $U_{10}=5$ m/s)

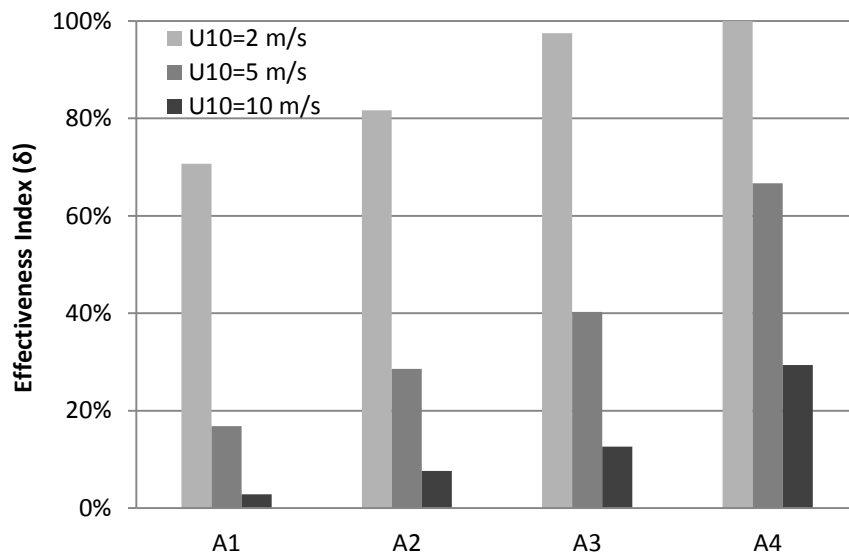


FIGURE 4.10 – EFFECTIVENESS INDEX OF THE 60 cm OVERHANG OVER DIFFERENT PORTIONS OF THE WINDWARD FACADE OF THE CUBIC BUILDING UNDER DIFFERENT WIND SPEEDS ($\theta=0^\circ$, $R_h=5$ mm/hr)

However, the same overhang has almost no overall effect (~3%) and considerably smaller effects on the upper 15% of the facade (~30%) when the facade is subject to a strong wind with $U_{10}=10$ m/s. These results also show the greater sensitivity of the effectiveness of the overhang to the

position on the facade under high wind speed. Changing the area over which the effectiveness index is being calculated from A1 to A4 (100% to 15% of the facade), the effectiveness of the 60 cm overhang improves by a factor of 1.4 under $U_{10}=2$ m/s ($\delta=100\%$ versus $\delta=70\%$). However, with $U_{10}=10$ m/s, A4 ($\delta=30\%$) receives 10 times better protection than the whole facade ($\delta=3\%$).

Figure 4.11 shows the effectiveness index of the 60 cm overhang over different areas on the facade and under different wind angles. The overhang is quite effective in protecting the upper portions of the facade (A3 and A4) from WDR under all the examined wind angles. The 60 cm overhang is most effective in protecting different areas of the facade when the building subject to a 60° wind. Note, nonetheless, that the effectiveness index is a measure of reduction in catch ratio *relative* to the case without an overhang. As the wind angle increases, the windward facade receives less WDR. This can be seen in Figs. 4.6A and 4.6B, comparing the catch ratio contours without the overhang and under different wind angles.

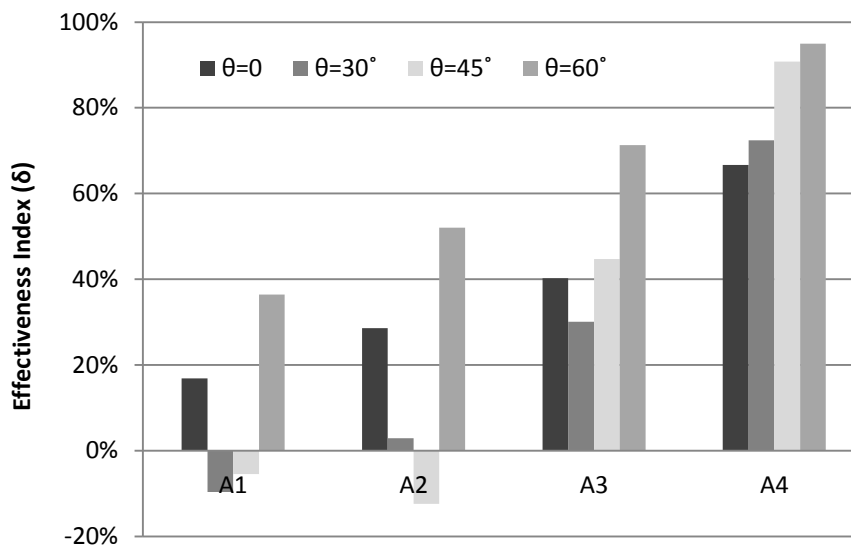


FIGURE 4.11 – EFFECTIVENESS INDEX OF THE 60 cm OVERHANGS OVER DIFFERENT PORTIONS OF THE WINDWARD FACADE OF THE CUBIC BUILDING UNDER DIFFERENT WIND ANGLES ($U_{10}=5$ m/s & $R_h=5$ mm/hr)

The negative value of the index over A1 and A2, under 30° and 45° winds, suggests that the overhang would have some *adverse* effects. Since the index is positive over A3 and A4 for all the angles, the locations at which the overhang has increased the deposition of WDR should all be in the lower two-thirds of the facade. Evidence of such adverse effects, *i.e.* an enhanced WDR load when an overhang is added, can also be seen in the contours of Fig. 4.6A. For example, for

$\theta=30^\circ$, the 0.25 contour line is being *pushed down* after the 60 cm overhang was added. This means that at almost half the height of the building and close to the windward edge ($z \sim -5$ and $-5 < y < -4$), the overhang does not have protective effects, but also has led to increased WDR deposition. It is noteworthy, nevertheless, that the uncertainty associated with the numerical simulation is larger at the lower half the facade and the observed increase in the catch ratio could be partly due to numerical errors.

To provide more insight into the results shown in Fig. 4.11, catch ratio values averaged over areas A1 to A4 with and without the 60 cm overhang are shown in Table 4.4. These values are for a $U_{10}=5$ m/s wind approaching at different angles and a moderate rainfall intensity of $R_h=5$ mm/hr. Shaded cells show the cases where the addition of the overhang has led to an increased catch ratio, and thus a negative effectiveness index.

TABLE 4.4 – AREA-AVERAGED CATCH RATIO VALUES WITHOUT AND WITH THE 60 cm OVERHANG UNDER DIFFERENT WIND ANGLES ($U_{10}=5$ m/s, $R_h=5$ mm/hr)

θ [°]	OH [cm]	η [-]			
		A1	A2	A3	A4
0	0	0.281	0.399	0.448	0.514
	60	0.233	0.285	0.268	0.171
30	0	0.157	0.204	0.223	0.234
	60	0.172	0.198	0.156	0.065
45	0	0.132	0.185	0.209	0.244
	60	0.140	0.208	0.116	0.023
60	0	0.096	0.171	0.208	0.261
	60	0.061	0.082	0.060	0.013

4.1.3. Discussion

As discussed in Chapter 2, under steady state conditions, the calculation of catch ratio is simplified to calculating the ratio of areas from which raindrops are falling to the areas on the facade that are wetted by WDR. Hence, understanding raindrop trajectories and their deposition patterns on the facade is the key to interpretation of the catch ratio results.

As implied by Eq. (2.8), two forces, namely gravity and drag, affect wind-driven raindrops. It is the balance between these forces that determines the trajectory of a raindrop. Small raindrops ($d < 2$ mm) tend to be mainly affected by the wind drag force, more strictly follow the wind flow

patterns and thus have highly curved trajectories. On the other hand, large raindrops are gravity driven, are less influenced by the flow field and tend to have straight trajectories. Their motion can be projected as vertically free falling under gravity and horizontally being carried by wind without slip. An actual rainfall event consists of raindrops with diameters in the typical range of 0.3-6 mm. The empirical correlation given by Best [60] for the size distribution of raindrops shows that as the rainfall intensity increases, the size of the raindrops that hold the greatest share also increases.

Figure 4.12 shows the trajectories of small ($d=0.5$ mm) and large ($d=3$ mm) raindrops in side and top views. It should be noted that, while these graphs are generated for $U_{10}=5$ m/s, the raindrop trajectories have the same general patterns under different wind speeds. Note the pronounced difference of the trajectories around the corners and over the roof.

The presence of the large upstream vortex creates a *void* space adjacent to the facade in which the small raindrops are not driven horizontally anymore and start to free fall toward the ground. In addition, the vortex might drive the raindrops *back* from the building and prevent them from approaching the lower parts. The large gravity-dominant raindrops ($d=3$ mm), on the other hand, are deposited on the facade more uniformly. There is, nonetheless, a higher concentration of WDR deposition at the upper edge of the facade. These large raindrops are almost not affected at all by the vortex upstream of the building. Rather, they carry on their nearly straight line trajectories until they hit the facade.

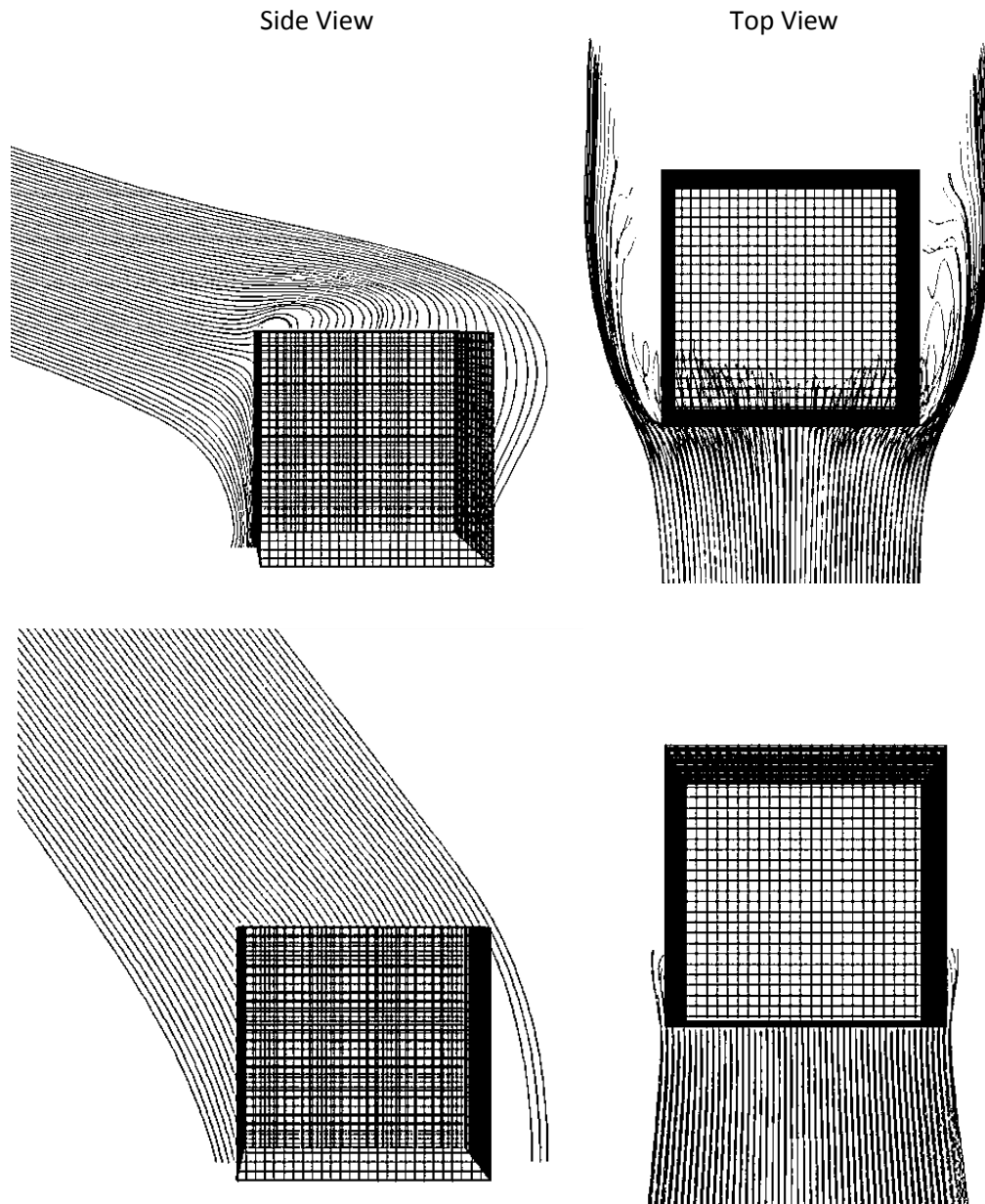


FIGURE 4.12 - RAINDROP TRAJECTORIES ($\theta=0^\circ$, $U_{10}=5$ m/s), TOP: $d=0.5$ mm, BOTTOM: $d=3$ mm

In Fig. 4.13, the deposition patterns of the same raindrops (0.5 mm and 3 mm) on the windward facades of the buildings without and with a 60 cm overhang are shown. Wind speed is fixed at $U_{10}=5$ m/s and the wind angle is $\theta=0^\circ$. It can be seen that the small drag-dominant raindrops ($d=0.5$ mm) are deposited on the facade with higher concentration around the corners and edges. On the lower half of the facade, significantly fewer raindrops are deposited.

It can also be seen in Fig. 4.13 that the 60 cm overhang almost completely protects the facade from smaller raindrops; only a few of these raindrops make it to the lower half of the facade and regions away from the edges and the upper half remain completely dry. On the other hand, only a small area at the top of the facade is protected from large raindrops. Disposition of the large raindrops on the lower parts of the facade is almost not influenced at all by the presence of the overhang.

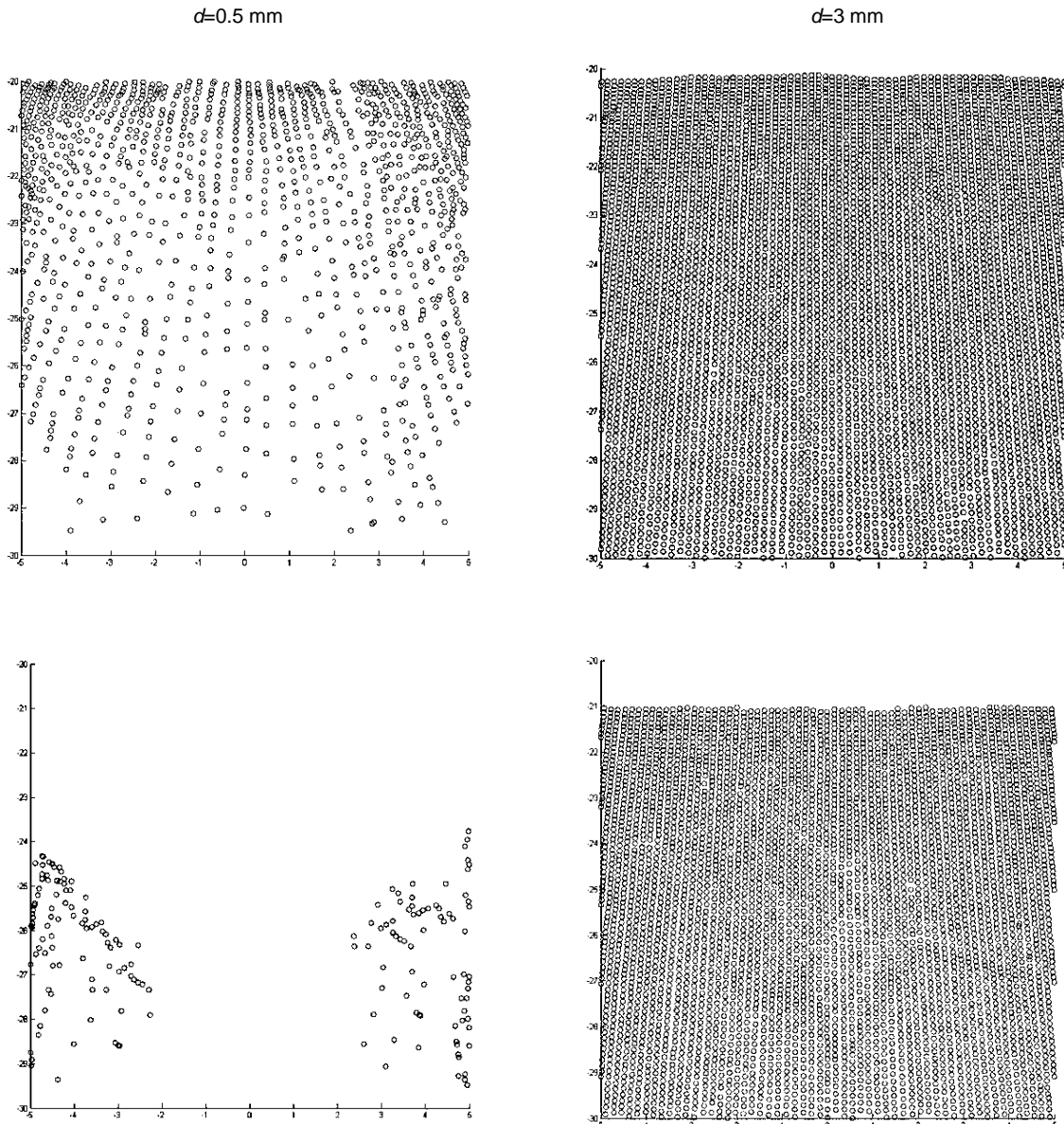


FIGURE 4.13 – DISTRIBUTION OF SMALL (LEFT) AND LARGE (RIGHT) RAINDROPS ON THE WINDWARD FACADE OF THE CUBIC BUILDING WITHOUT (TOP) AND WITH (BOTTOM) THE 60 cm OVERHANG UNDER A NORMAL WIND ($\theta=0^\circ$, $U_{10}=5$ m/s)

In Fig. 4.14, the deposition patterns of the same representative raindrops ($d=0.5$ mm and 3 mm) are depicted over the windward facade of the cubic building subject to an oblique wind with $\theta=45^\circ$ and $U_{10}=5$ m/s. As expected, the raindrops are more packed near the windward edge ($z=-5$). The concentration of the raindrops decreases from the windward edge toward to downwind edge. This variation is more pronounced for smaller raindrops ($d=0.5$ mm). This is another indication of how they closely follow the wind streamlines. The performance of the overhang is, however, different under this oblique wind. The area fully protected from the small raindrops has drastically decreased from almost 70% (for normal wind, Fig. 4.13) to almost 25% of the total facade area. Moreover, the lower half of the facade is not protected at all from these small drag-driven raindrops. For large raindrops ($d=3$ mm), the influence of the 60 cm overhang under the oblique wind is more similar to its influence under the normal wind. The main difference is observed over a small area around the top left corner of the facade where raindrops have *penetrated* just below the overhang and have wetted an area which had been fully protected under the normal wind (Fig. 4.13).

Figure 4.15 shows the distribution of specific catch ratios on the facade for the same two raindrop sizes (0.5 mm and 3 mm), under the wind conditions of $\theta=0^\circ$ and $U_{10}=5$ m/s, without and with a 60 cm overhang. Comparison of this figure to Fig. 12 shows how the raindrop distribution patterns are interconnected with and translated to catch ratio contours. The same observations regarding the regions that receive higher concentrations of WDR and the protecting effects of the overhang can be made based on these contours. As previously mentioned, the introduction of overhangs not only changes the value of catch ratio at individual points, but also leads to changes in the wetting pattern of the facade (the configuration of the contour lines). Note that although there are a number of 0.5 mm raindrops hitting the lower half of the facade, no contour line is shown over that area ($\eta_{d=0.5}=0$). This is due to the computational scheme used for calculating catch ratios; if the number of raindrops in a cell is not large enough to form a *wetted area*, the catch ratio corresponding to that cell will be zero (See section 2.3).

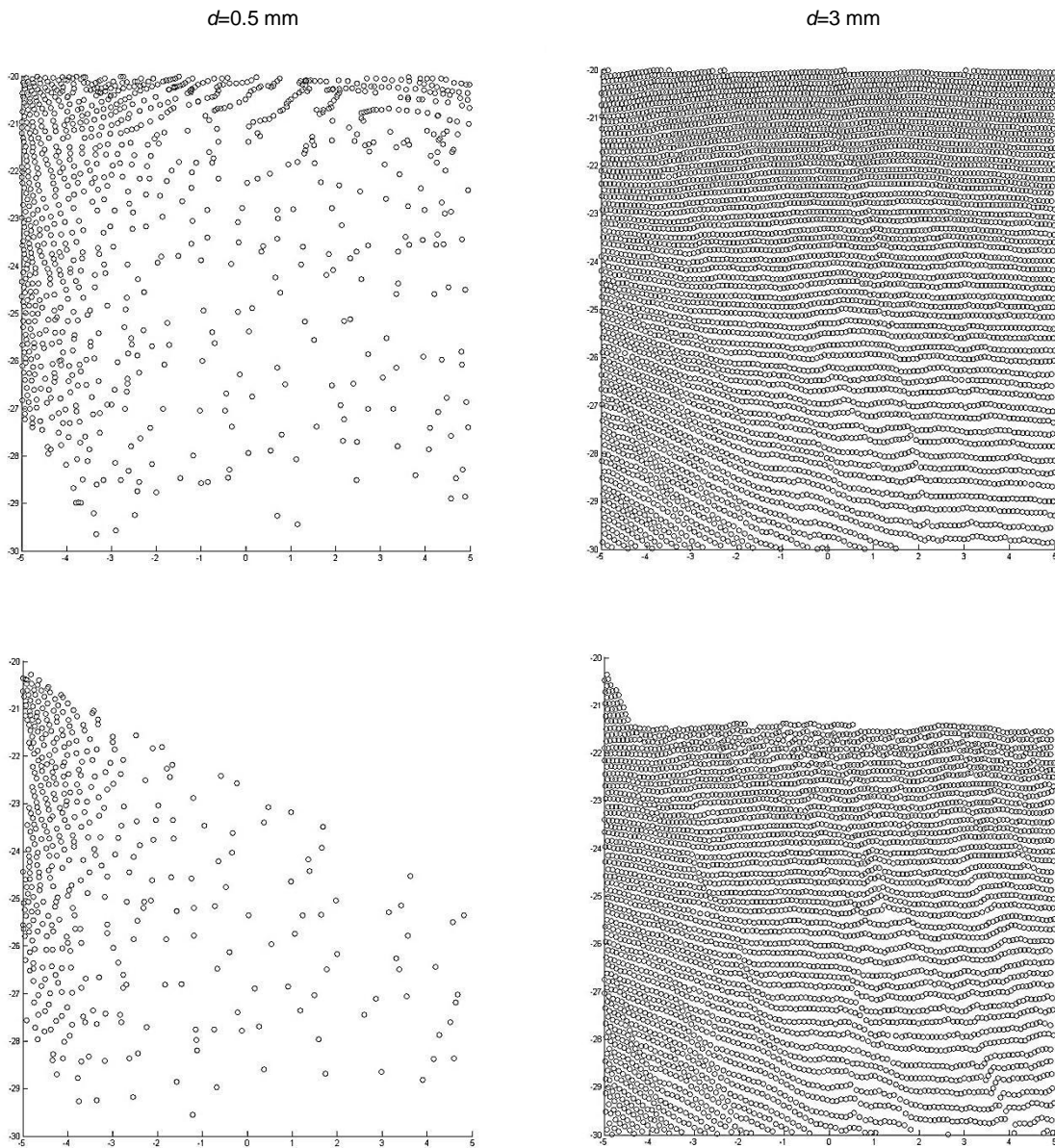


FIGURE 4.14 – DISTRIBUTION OF SMALL (LEFT) AND LARGE (RIGHT) RAINDROPS ON THE WINDWARD FACADE OF THE CUBIC BUILDING WITHOUT (TOP) AND WITH (BOTTOM) THE 60 cm OVERHANG UNDER AN OBLIQUE WIND ($\theta=45^\circ$, $U_{10}=5$ m/s)

The observations made based on the raindrop distribution are confirmed by the contours of Fig. 4.15. Almost 70% of the facade is protected from 0.5 mm raindrops, for which no contour line is shown. Less than 10% of the facade is protected from 3 mm raindrops. Specific catch ratio values ($d=3$ mm) are reduced as much as 50% by introducing the 60 cm overhang.

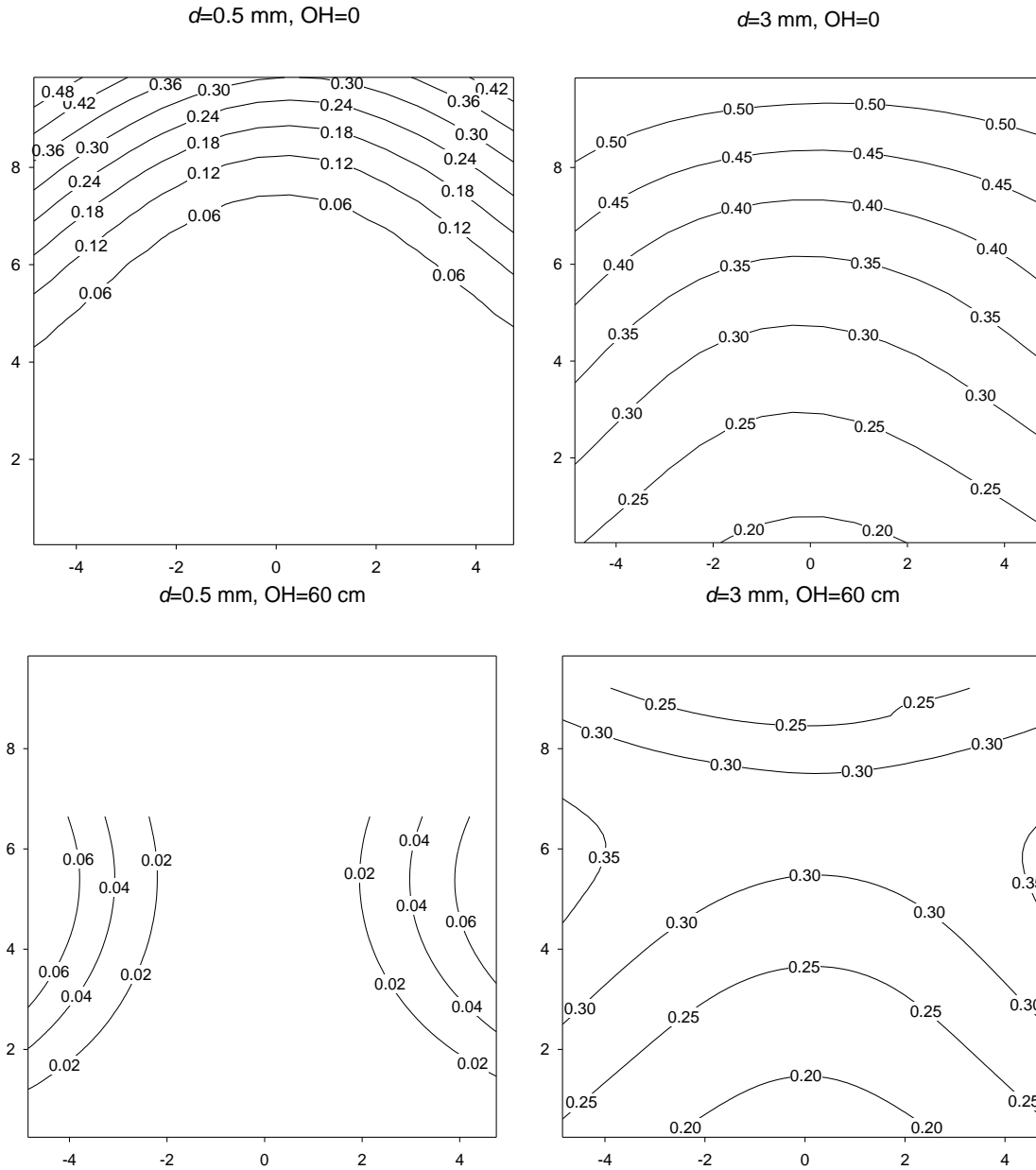


FIGURE 4.15 – SPECIFIC CATCH RATIO CONTOURS ON THE WINDWARD FACADE OF THE CUBIC BUILDING WITHOUT (TOP) AND WITH (BOTTOM) THE 60 cm OVERHANG ($\theta=0^\circ$, $U_{10}=5$ m/s)

Based on these observations, and various numerical tests, the impact of overhangs on WDR deposition on buildings is attributed to two major effects. The first one is the *direct* protection of the facade from rain exposure. This effect, which is dominant for larger (gravity-driven) raindrops, can be clearly seen in Figs. 4.14 and 4.15. This direct effect is also expected to be dominant under high rainfall intensities, where large (gravity-driven) raindrops are more likely to

appear, and low wind speeds, where the raindrop trajectories have larger slopes. The second effect is the *indirect* effect of the overhang through the disturbance it introduces in the wind flow pattern. This disturbance is pronounced especially in the standing upstream vortex, the high vorticity regions around the corners and edges, and the wake above the building roof. Since small (drag-driven) raindrops follow the wind flow more strictly, the indirect effect is expected to be more significant for them. Therefore, this effect is dominant under low rainfall intensities, where small raindrops hold a greater share.

These effects are more clearly seen in Figure 4.16 where the catch ratio distributions are shown as 3D surfaces. The contours presented in the results section are projections of such 3D surfaces on the y-z plane (the windward facade). Note how the almost linear surface showing the distribution of the catch ratio without an overhang turns into a highly curved surface when a 60 cm overhang has been added. Most notably, the addition of the overhang has led to the occurrence of a saddle point at approximately $y=7$ and $z=0$. The large curvature of the plane is due to the indirect effects of the overhang, *i.e.* the change in the flow patterns upstream of the building.

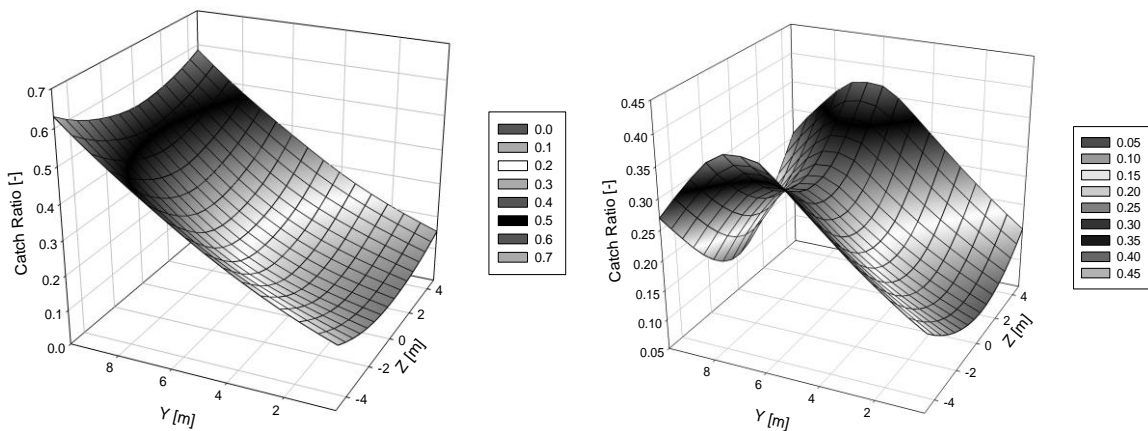


FIGURE 4.16 - DISTRIBUTION OF CATCH RATIO ON THE WINDWARD FACADE OF THE CUBIC BUILDING WITHOUT (LEFT) AND WITH (RIGHT) THE 60 cm OVERHANG ($\theta=0^\circ$, $U_{10}=5$ m/s, $R_h=5$ mm/hr)

The actual influence of the overhang will be a combination of these two effects, which can both be seen in Fig. 4.17. This figure shows the trajectories of small drag-driven as well as large gravity-driven raindrops under low and high wind speeds of $U_{10}=2$ m/s and $U_{10}=10$ m/s. Note that, under the low wind speed, from both small and large raindrops, a few of them approaching

the upper edge are *directly* blocked by the overhang. This direct effect is relatively small considering the small width of the overhang (30 cm). However, there are other raindrops influenced by the presence of the overhang; the overhang has created a *dead zone* where small raindrops have highly curved trajectories and approach the ground almost free falling. The large raindrops, on the other hand, are almost not affected at all away from the top edge. For the high wind speed, the direct shading effect is almost nonexistent for both small and large raindrops. The indirect effect is substantially smaller. The majority of the raindrops approaching the facade hit the building. A small portion of the small raindrops is influenced, nevertheless, by the effect of the overhang on the wake.

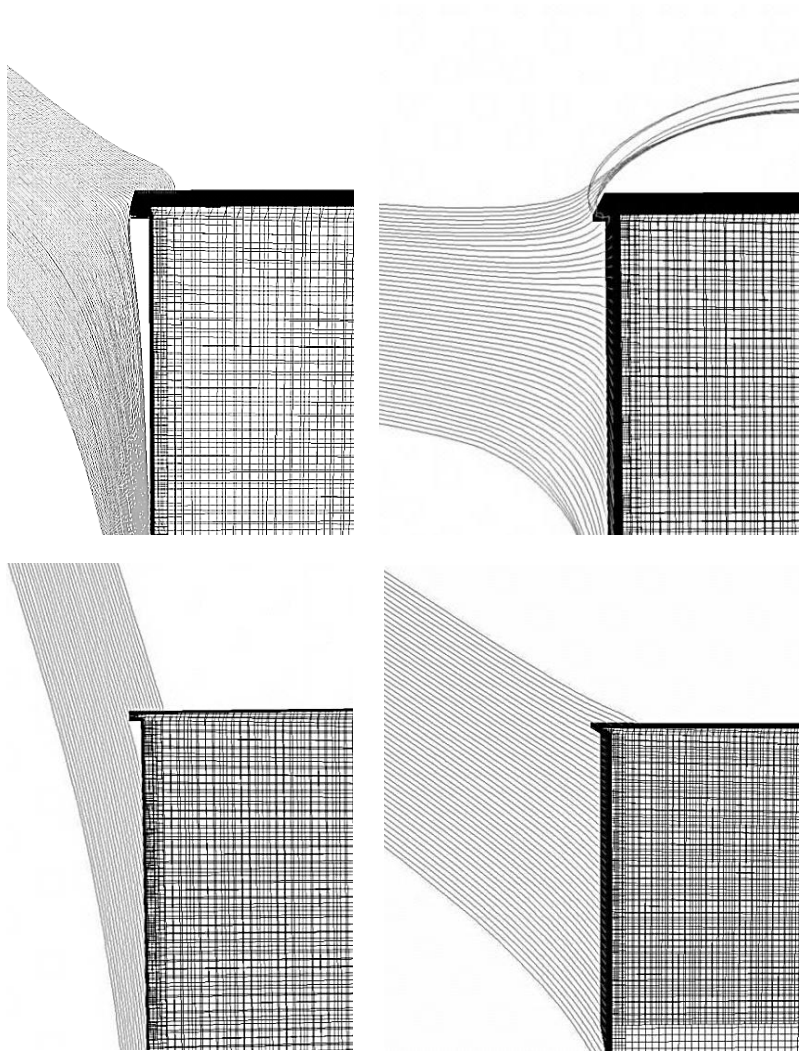


FIGURE 4.17 – EFFECTS OF A 30 cm OVERHANG ON 0.5 mm (TOP) AND 3 mm (BOTTOM) RAINDROPS UNDER NORMAL WIND WITH DIFFERENT SPEEDS, LEFT: $U_{10} = 2$ m/s, RIGHT: $U_{10} = 10$ m/s

The Effects of Overhang Size

As the overhang width increases, the area *shaded* by the overhang increases and the disturbance introduced by the overhang to the wind flow field upstream of the building will be larger. Therefore, both direct and indirect effects of the overhang will increase. Hence, as expected, larger overhangs are more effective in protecting the facade from WDR.

All the overhangs studied in this work have the same thickness (15 cm). Compared to the other geometric length scales involved, especially the building height, and within a practical range, the thickness of the overhang would have negligible effects.

The Effects of Rainfall Intensity

The protection a given overhang provides against raindrops of a certain size is only a function of its size and wind conditions (angle and speed). On the other hand, the overall effectiveness of an overhang in an actual rainfall event is the combination the effects it has on different raindrops. This combined effect is governed by the raindrop size distribution, *i.e.* the share raindrops of a certain diameter hold in the total rainwater driven to facade (and affected by the overhang). As discussed in Chapter 2, this size distribution is determined by the rainfall intensity. Therefore, the overall effectiveness of an overhang in a rainfall event is connected, however indirectly, to the intensity of the rainfall.

As mentioned previously, catch ratio values, as well as the performance of the overhang, demonstrate a greater sensitivity when lower intensities are examined. This can be attributed to the fact that the low rainfall intensities comprise a majority of smaller drops that are carried by wind more easily and deposited at the upper part of the facade. On the other hand, large drops, which hold greater shares under high intensity rainfalls, tend to fall in straight trajectories and hit the lower portions of the facade. This is in agreement with the observations reported by Blocken [29]. He has shown the relationship between catch ratio and the rainfall intensity to be nonlinear for low intensities ($R_h \leq 2$ mm/hr) and almost linear for moderate and high ($R_h > 2$ mm/hr) intensities of rainfall.

However, the fact that different overhangs have almost constant effectiveness index under a variety of rainfall intensities suggests that the sensitivity of the effectiveness index to the

raindrop size is not large enough to make a significant difference in the overall (average) effectiveness index when different weighting functions are used.

The Effects of Wind Speed

The wind speed seems to be the dominant factor in the performance of overhangs. All the examined overhangs are more effective under low wind speed. When driven by lower speed winds, raindrops tend to have steeper trajectories since the horizontal component of their motion would be smaller than their vertical free fall. Therefore, the direct shading effect of the overhang is expected to be larger under low wind speeds. This can be seen in Fig. 4.18. Far from the building, the slope of the raindrop trajectory ($\tan \gamma$) can be calculated as the ratio between the magnitudes of the vertical and the horizontal components of the raindrop velocity.

Since, far enough above the ground, the magnitude of the horizontal and vertical velocities of the raindrop are equal to the wind speed at the same elevation and the raindrop terminal velocity respectively, the slope calculated from Eq. (4.5) is proportional to the inverse of the wind speed. This is shown schematically in Fig. 4.18 where the slope of raindrop trajectories (for a fixed raindrop size) and the projected/protected height (l) beneath the overhang are compared for low and high wind speeds.

$$\tan \gamma = \left(\frac{V_t}{U} \right) = \frac{l}{OH} \quad (4.5)$$

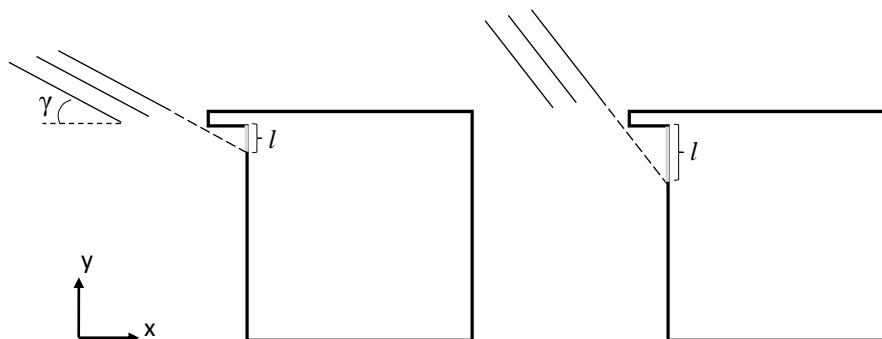


FIGURE 4.18 – PROJECTED AREA BENEATH THE OVERHANG UNDER HIGH (LEFT) AND LOW (RIGHT) SPEED WINDS

In addition, less irregularity is observed in the in the flow field under low wind speeds. The small drag-driven raindrops have, hence, trajectories with smaller curvature gradients. The overhang can have larger impacts in raindrops with regular trajectories.

The Effects of Wind Direction

The wind direction has significant effects on both the WDR deposition on the facade and the effectiveness of the overhang. Differences in the raindrop distribution patterns under different wind angles are obvious when Figs. 4.13 and 4.19 are compared. Wind speed is $U_{10}=5$ m/s in both graphs. When compared to Fig. 4.13, the large gravity-driven raindrops ($d=3$ mm) seem to be less affected by the change in the direction of the wind than the small ones.

Based on these graphs, as well as other numerical tests, it has been concluded that almost the entire facade receives both small ($d=0.5$ mm) and large ($d=3$ mm) raindrops when subject to winds with angles from 0° to 45° . Under oblique winds, nonetheless, the small drag-driven raindrops are deposited with a higher concentration around the windward edge ($z=-5$). By increasing the wind angle to $\theta=60^\circ$, a different effect is observed. While the deposition pattern of the large raindrops remains more or less unchanged, the smaller raindrops are driven away from the facade. Under the 60° wind, half of the facade is almost untouched by the 0.5 mm raindrops. This observation can explain the shift of the maximum catch ratio lines in Figs. 4.6A and 4.6B towards to the $z=+5$ edge as the wind angle exceeds 45° . Similar behaviour has been reported by Blocken [31]. As discussed in the review of the literature, such observations show the weakness of the cosine projection technique, *i.e.* calculating catch ratio for oblique winds by multiplying the values from normal winds by the cosine of the wind angle.

The indirect effects of the overhang are more influenced, than the directly shaded area beneath the overhang, by the wind angle since the structure of the flow around the building is dependent upon the approaching angle. As the wind angle increases, the blocking effect of the building on the wind decreases and the wind would flow over the windward facade more easily. A larger wake would also form over the windward facade. As mentioned previously, the large drag force in the regions of the wind flow field with high velocity gradients, such as wakes, significantly accelerates the raindrops, especially the smaller ones. This acceleration can result in changes in

both magnitude and direction of the particle velocity. Consequently, raindrops are more easily carried away by the winds with large angles.

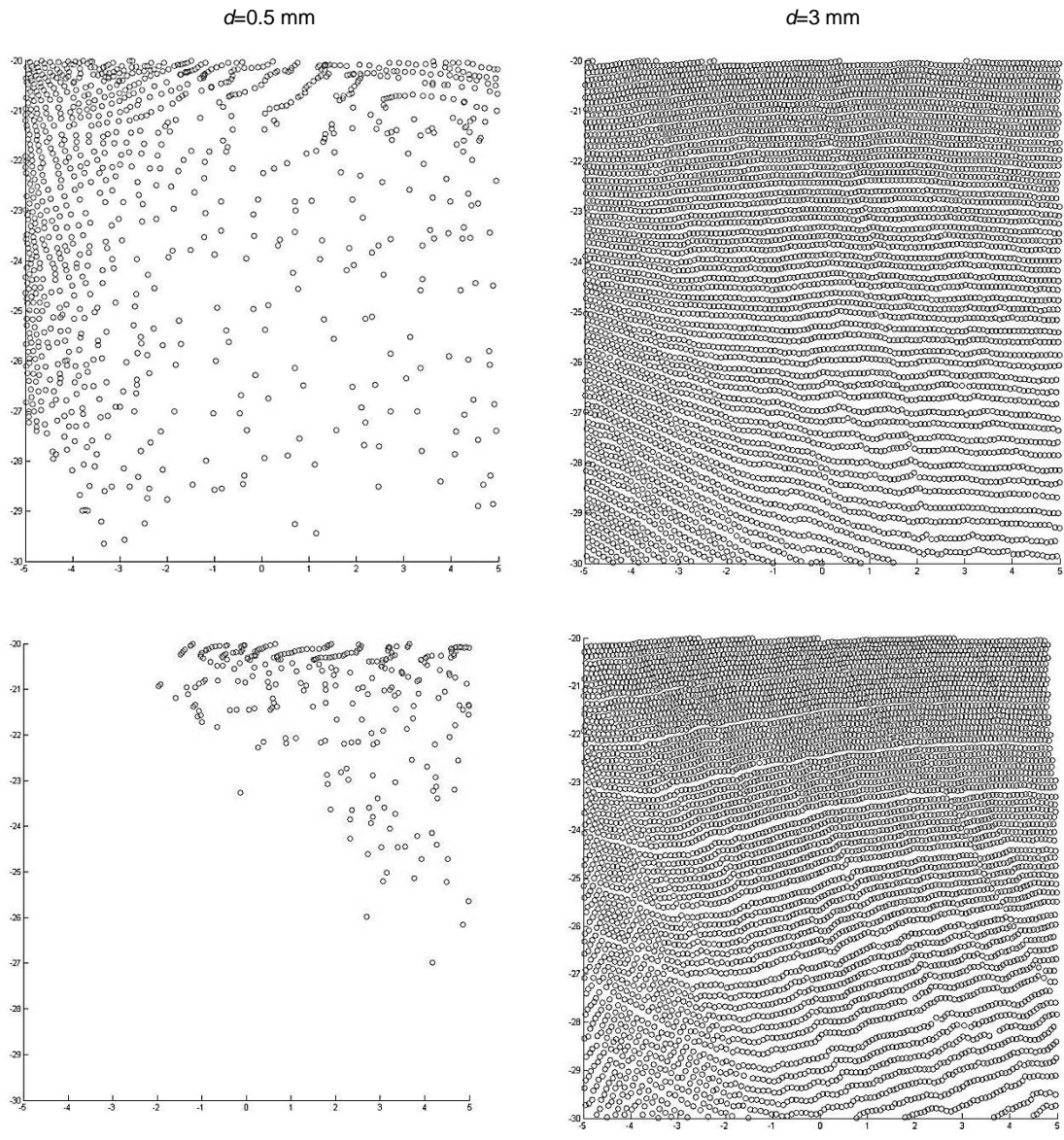


FIGURE 4.19 – DISTRIBUTION OF SMALL (LEFT) AND LARGE (RIGHT) RAINDROPS ON THE WINDWARD FACADE OF THE CUBIC BUILDING WITHOUT AN OVERHANG UNDER TWO OBLIQUE WINDS
TOP: $\theta=45^\circ$, BOTTOM: $\theta=60^\circ$ ($U_{10}=5$ m/s)

Under oblique winds, raindrops are also likely to get *trapped* underneath the overhang around the top corner of the windward edge. This is clearly shown in Fig. 4.15. Such trapped raindrops

lead to a reduction in the effectiveness of the overhang and might even cause adverse effects, *i.e.* increased catch ratio values.

Adverse Effects of Overhangs

As previously mentioned, the presence of the overhang can lead to an increase in the catch ratio at some locations and under certain wind conditions. Such *adverse* effects are observed when 60 cm overhangs are studied under oblique ($\theta=30^\circ$ and 45°) and high speed ($U_{10}=10$ m/s, [70]) winds. Different reasons, including raindrops being *trapped* underneath a wide overhang, are suggested for these observations. It is, nevertheless, doubtless that the addition of an overhang helps protect the upper portions of the facade from WDR loads overall. Recall that these portions are most vulnerable to WDR loads and thus most critical to protect.

In addition, it is suspected that when a time-averaged evaluation of the performance of the overhang is performed, such adverse effects would vanish. Recall that all cases presented in this study are under fixed steady wind and rain conditions. The adverse effect of an overhang at a certain point on the facade might be *averaged out* under realistic wind and rain conditions, *i.e.* varying wind speed, wind angle and rainfall intensity. Hence, in spite of the cases where the addition of an overhang has led to intensified exposure to WDR, firm conclusions about such effects cannot be made before a more comprehensive study under transient wind and rain is performed.

The Effectiveness Evaluation Area

As shown, and briefly discussed, in the results section, the area on the facade over which the performance of the overhang is being studied and evaluated can affect the effectiveness index, and accordingly, the observations on the performance of the overhang. Assessments based on areas over the upper half of the facade seem to be more reliable because *i)* as mentioned the results section, these areas are more vulnerable to WDR loads and *ii)* the uncertainty of the results of the numerical simulation is larger in the regions close to the ground. The presence of the upstream standing vortex, neglecting the turbulent dispersion of the raindrops, treatment of the turbulent boundary layer with wall functions and uncertainties associated with the representative values of surface roughness are some of the reasons of this uncertainty.

4.2. The Cassier Building

With the original target of this study being mid- and high-rise buildings, the performance of an overhang is studied when added to the *Cassier* building (the test building used for validation of the numerical simulation). Only the effects of a 90 cm overhang added to the North and East sides are studied. WDR is simulated when a moderate wind ($U_{10}=5$ m/s) approaches the North and East facades in the normal direction. The wind angle is measured clockwise with $\theta=0^\circ$ being normal to the North facade. A schematic of the building is shown in Fig. 4.20. The building is 20.06 m high (y).

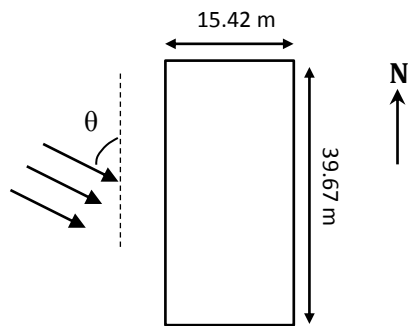


FIGURE 4.20 – SCHEMATIC OF THE CASSIER BUILDING (TOP VIEW)

Information on the computational domain size and discretization is summarized in Table 4.5. Note the slight difference in the grid size between the current simulations and those presented in Chapter 3.

TABLE 4.5 - COMPUTATIONAL DOMAIN SIZE & DISCRETIZATION FOR THE CASSIER BUILDING

Domain Length (x)		430 m	
Domain height (y)		100 m	
Domain Width (z)		190 m	
Surface Mesh	Size	Domain sides	3 m
		Building walls	0.275-0.3 m
	Type	Quadrangle	
Volume Mesh	Number of CV's		$\sim 1.67 \times 10^6$
	Type		Tetrahedral

The boundary conditions, however, are the same as those used in the validation study presented in Chapter 3 (see Appendix C) except for the exponent of the wind speed profile (α_p) that has been replaced by 0.3 to represent a larger obstruction of wind by the surroundings of the building.

4.2.1. Catch Ratio Contours

In this section, catch ratio contours over the windward facade of the Cassier building are presented for the cases without and with the 90 cm overhang. In these contours, horizontal and vertical axes are in z- and y-direction respectively. The x-direction is normal to the windward facade. All catch ratio calculations are performed for 0.3 m \times 0.3 m cells. As in the previous section, contours are generated after smoothing catch ratio data using algorithms such as *Negative Exponential* and *Losses* [69].

Figure 4.21 shows the catch ratio distribution on the North facade of the Cassier building. In these contours, the wind has a moderate speed of $U_{10}=5$ m/s and approaches the facade in the normal direction. Wetting patterns of the facade of the building without and with a 90 cm overhang under different rainfall intensities are shown. Without the overhang, the catch ratio increases as the rainfall intensity increases. Note that for the cubic building, the top corners of the windward facade received higher WDR loads under low rainfall intensities (Fig. 4.4). WDR deposition on the lower parts of the facade is almost independent of the rainfall intensity. Similar to case of the cubic building, the addition of the 90 cm overhang has created a *saddle point* in the distribution of catch ratio. At around half the height of the facade ($y\sim 10$), the addition of the overhang has increased catch ratio values. This increase is slight in the center parts ($z\sim 0$) and pronounced near the edges ($|z|>5$). These adverse effects are smaller under the high intensity rainfall ($R_h=10$ mm/hr).

Catch ratio contours on the East facade of the Cassier building under different rainfall intensities are shown in Fig. 4.22. The wind is approaching normal to the facade with a speed of $U_{10}=5$ m/s. Contours are shown for the cases without and with a 90 cm overhang. Similar to the North facade, and unlike the cubic building, as the rainfall intensity increases, the catch ratio values increase as well, even close to the top corners. The saddle point created by the overhang can be

seen in these contours too. The overhang has decreased the catch ratio values at the upper half and in the center parts of the facade ($y > 10$ and $-10 < z < 10$) especially. Note how the *directly* protected area on the top of facade is the same as the one on the North facade. The lower parts of the facade receive almost the same amount of WDR under different rainfall intensities. This region is hardly affected by the 90 cm overhang. Top corners of the facade are either adversely affected ($R_h = 2$ mm/hr) or not affected ($R_h = 5$ and 10 mm/hr) by the overhang.

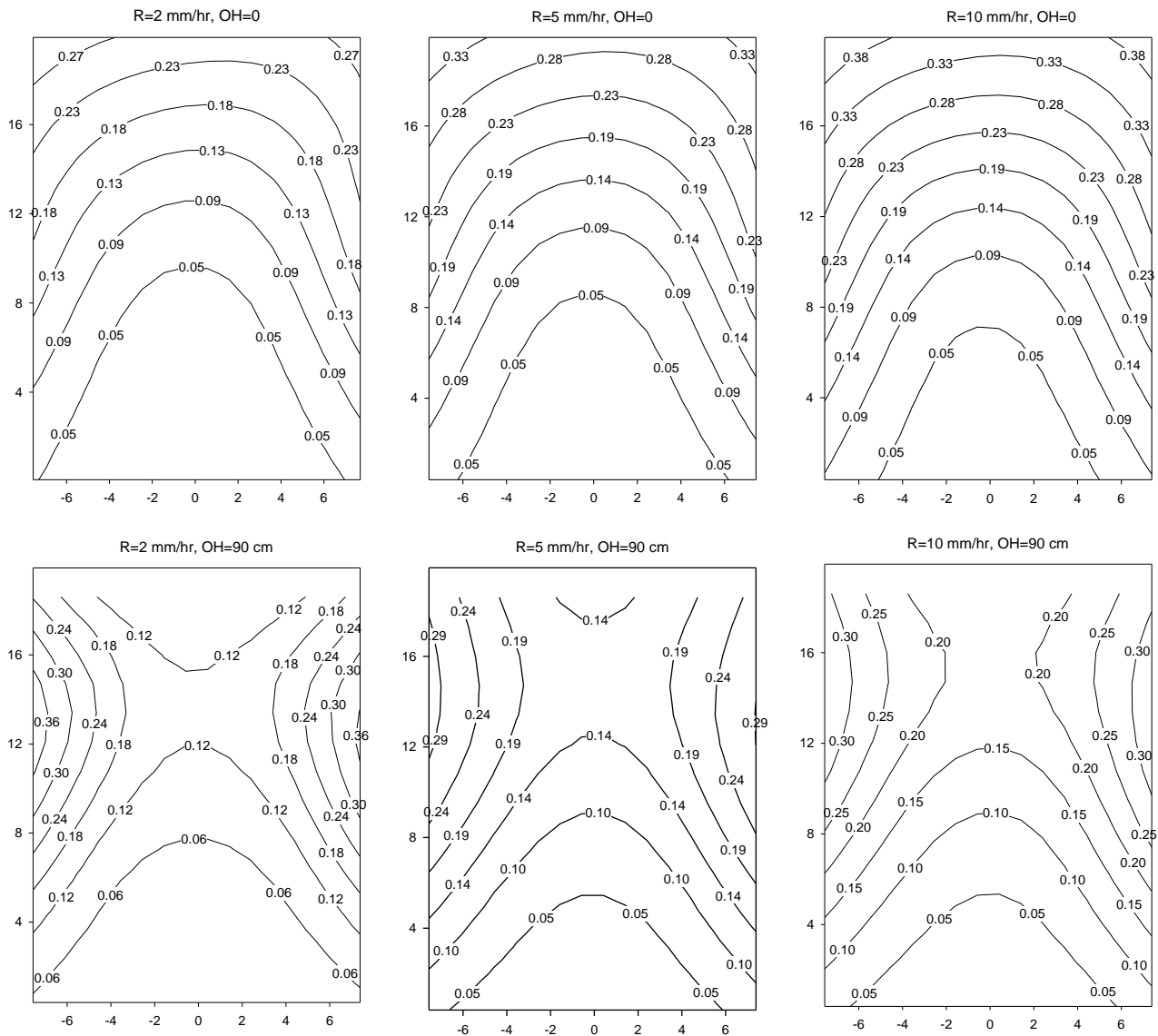


FIGURE 4.21 - CATCH RATIO CONTOURS ON THE NORTH FACADE OF THE CASSIER BUILDING UNDER DIFFERENT RAINFALL INTENSITIES, WITHOUT (TOP) AND WITH (BOTTOM) THE 90 cm OVERHANG ($\theta = 0^\circ$, $U_{10} = 5$ m/s)

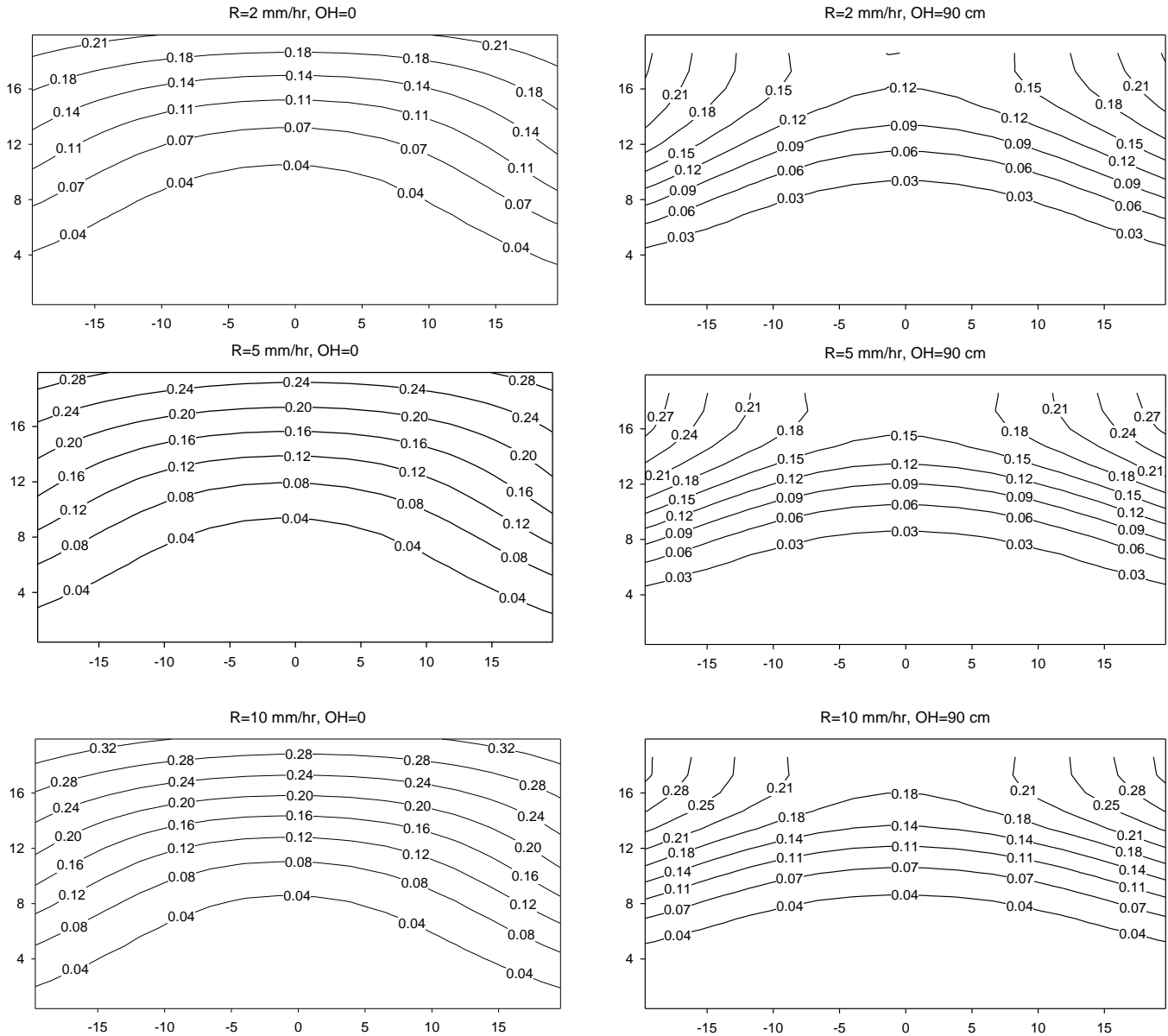


FIGURE 4.22 – CATCH RATIO CONTOURS ON THE EAST FAÇADE OF THE CASSIER BUILDING UNDER DIFFERENT RAINFALL INTENSITIES, WITHOUT (LEFT) AND WITH (RIGHT) THE 90 cm OVERHANG ($\theta=90^\circ$, $U_{10}=5$ m/s)

4.2.2. Effectiveness Index

The effectiveness index introduced in section 4.1.2 is calculated over a number of areas over both North and East facades. These areas are shown in Fig. 4.23. The adverse effects of the 90 cm overhang, especially near the edges of the North facade are clearly reflected in the reported indices. Areas N5 to N7 are equal to N2 to N4 respectively in height, but cover half of

the facade in width. Areas E5, E6 and E7 have widths equal to 70% of the total width of the facade and heights equal to those of E2 to E4.

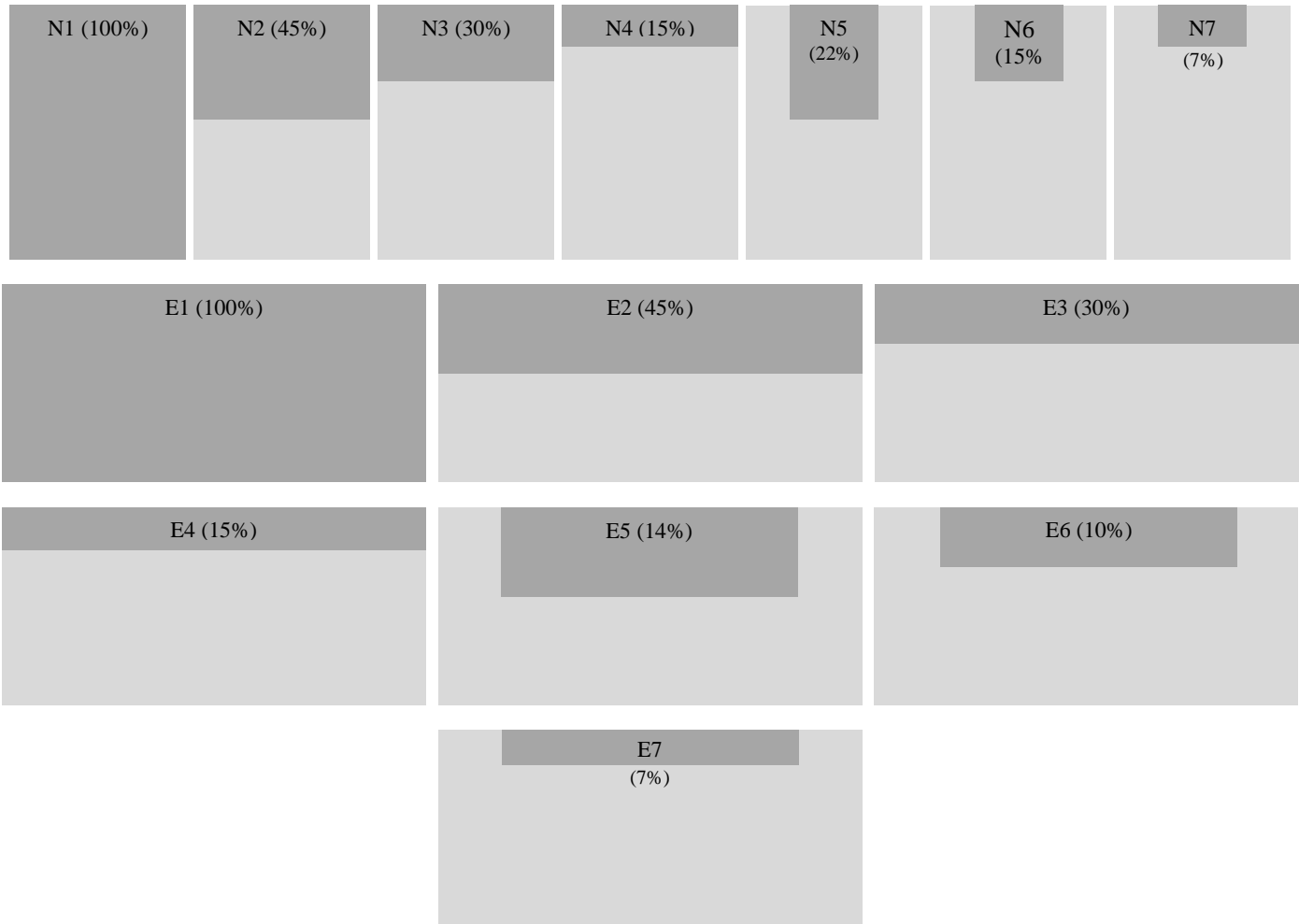


FIGURE 4.23 – EFFECTIVENESS INDEX CALCULATION AREAS ON THE NORTH (N1-N7) AND EAST (E1-E7) FACADES OF THE CASSIER BUILDING

The diagrams of Fig. 4.24 show the effectiveness indices of the 90 cm overhang over the North facade under different rainfall intensities. A comparison of the indices over areas N1 to N4 shows that, regardless of the intensity of the rainfall, only a small upper portion of the facade is protected by the overhang. Adding the overhang, the total catch ratio averaged over the whole facade has increased by factors of 3, 2.4 and 2 for the low, moderate and high rainfall intensities respectively. However, the center parts of the facade (N6 and N7) are well protected by the overhang ($\delta \sim 30\%$ and $\sim 60\%$) and the negative values of δ over N3 and N4 are due to the increased catch ratios around the edges. This is in agreement with the observations made from

the contours of Fig. 4.21. Based on the diagrams of Fig. 4.24, the performance of the overhang has a relatively high dependency upon the rainfall intensity. Under the low intensity rainfall ($R_h=2$ mm/hr), the overhang has larger effects, either adverse or protective. The absolute value of δ (over all the areas) decreases as the rainfall intensity increases.

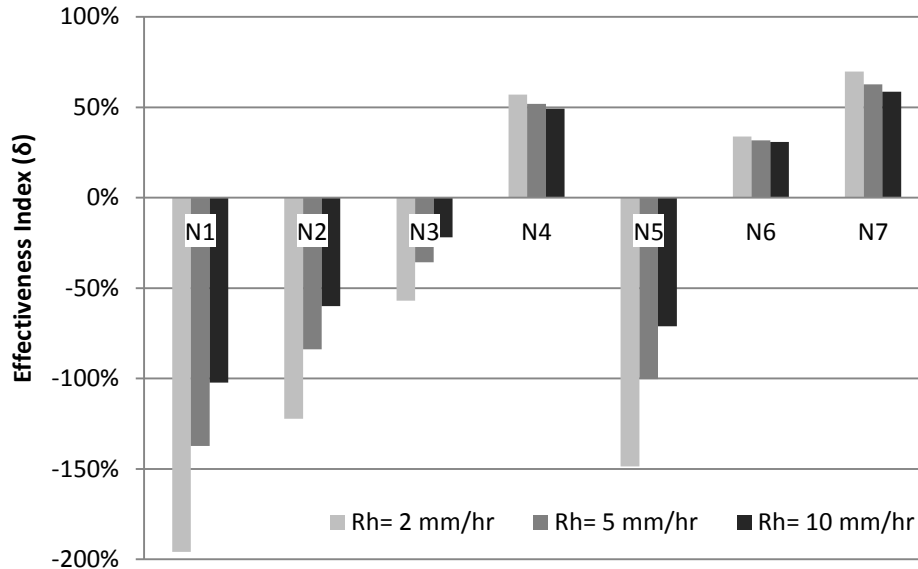


FIGURE 4.24 – EFFECTIVENESS INDEX OF THE 90 cm OVERHANGS OVER DIFFERENT PORTIONS OF THE NORTH FACADE OF THE CASSIER BUILDING UNDER DIFFERENT RAINFALL INTENSITIES ($\theta=0^\circ$, $U_{10}=5$ m/s)

Figure 4.25 shows the effectiveness index of the 90 cm overhang over different parts of the East facade of the Cassier building. Although the overhang has significantly adverse effects over the whole facade, and for all the studied rainfall intensities, its effectiveness index is positive over all the *partial* areas (E2 to E7). This observation implies that the adverse effects of the overhang are concentrated on the lower half of the facade. The 90 cm overhang has better performance in protecting the East facade from WDR in comparison to the North facade. The performance of the overhang is not influenced very much by the intensity of rainfall. For example, the effectiveness index of the overhang over E2, where it seems to be most dependent upon the rainfall intensity, is 12%, 18% and 15% for low, moderate, and high intensities respectively. The index is 98% over E4 and E7, independent of the intensity of rainfall. Moreover, the small difference between the values of δ over the full width (E2 to E4) and 70% width (E5 to E7) areas implies that the adverse effects of the overhang around the edges (as can be seen in the contours of Fig. 4.22) are not significant in comparison to the protection it provides at the center of the facade.

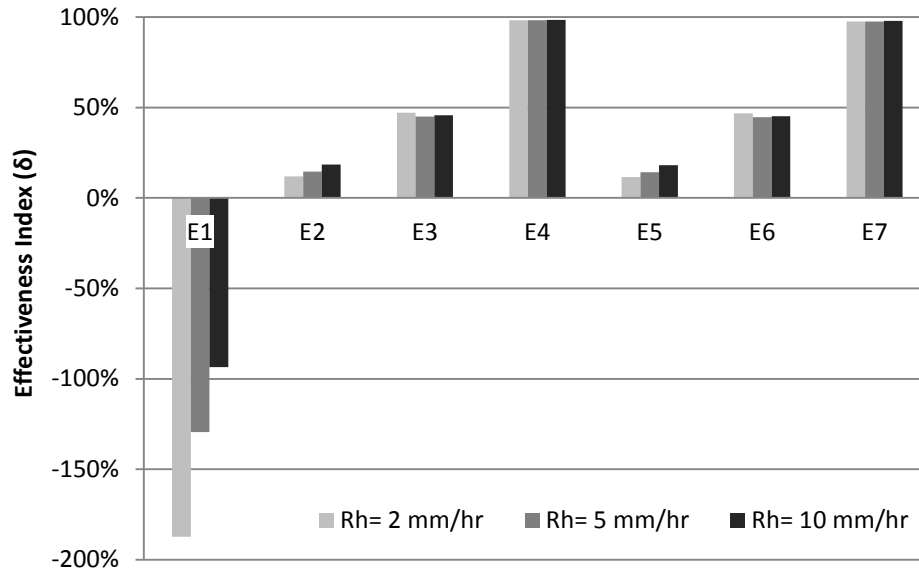


FIGURE 4.25 – EFFECTIVENESS INDEX OF THE 90 cm OVERHANGS OVER DIFFERENT PORTIONS OF THE EAST FACADE UNDER DIFFERENT RAINFALL INTENSITIES ($\theta=0^\circ$, $U_{10}=5$ m/s)

The performance of the 90 cm overhang over the East facade is more similar to the performance of the overhangs which were added to the cubic building (section 4.1), than to its performance on the North facade. Overall, the 90 cm overhang is found to be more effective in protecting the wider (East) facade.

4.2.3. Discussion

In this section, similar to what was presented in section 4.1.3, the results presented in sections 4.2.1 and 4.2.2 are discussed based on raindrop trajectories and other physical observations.

Figure 4.26 shows the deposition patterns of small ($d=0.5$ mm) and large ($d=3$ mm) raindrops on the North facade of the Cassier building, without and with the 90 cm overhang. The influence of the overhang is obviously more pronounced for the small raindrops. Almost 60% of the facade is fully protected by the 90 cm overhang from 0.5 mm raindrops, whereas this overhang protects only 5% of the facade from the 3 mm raindrops. Also, note how the overhang leads to a higher concentration of 0.5 mm raindrops at around half height of the facade, close to the edges. This observation can partly explain the adverse effects of the overhang, reported in the previous sections as increased values of catch ratio and negative effectiveness indices. Lower parts of the facade are almost not influenced at all by the presence of the overhang. Note, also, how no 0.5

mm raindrop is deposited on small regions at the top corners of the facade. Similar regions on the windward facade of the cubic building received considerable accounts of WDR, especially small raindrops.

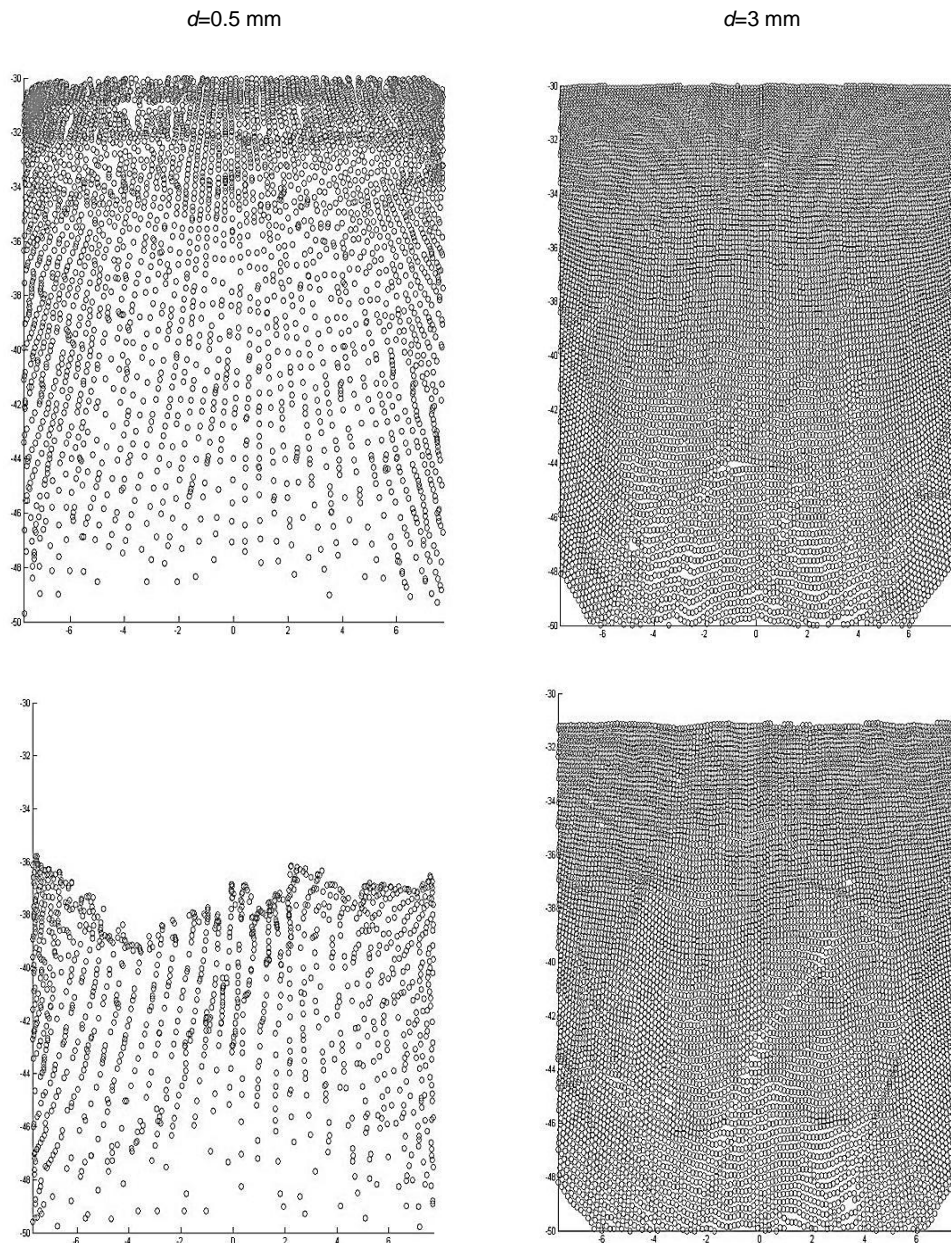


FIGURE 4.26 – DISTRIBUTION OF SMALL (LEFT) AND LARGE (RIGHT) RAINDROPS ON THE NORTH FACADE OF THE CASSIER BUILDING WITHOUT (TOP) AND WITH (BOTTOM) THE 90 cm OVERHANG ($U_{10}=5$ m/s)

Figure 4.27 shows the distribution of the same raindrops ($d=0.5$ mm and 3 mm) on the East facade of the building, without and with the 90 cm overhang. The overhang is significantly

effective in protecting this facade from the small ($d=0.5$ mm) raindrop. The facade has remained almost entirely untouched by these raindrops after the overhang was added. There is no significant change in small areas near the edges. Recall that similar positions on the North facade receive more WDR after the overhang is added (see Figs 4.21 and 4.26). On the other hand, and similar to the North facade, the 90 cm overhang can protect only about 10% of the top of the facade from 3 mm raindrops. Deposition of the large raindrops ($d=3$ mm) on the lower parts of the facade is almost not influenced at all by the overhang. The raindrop distribution pattern on the East has more similarity to that on the cubic building, expect for the top corner points which do not receive small raindrops. As mentioned, the top corners of the windward facade of the cubic building receive large WDR loads, specifically from small raindrops.

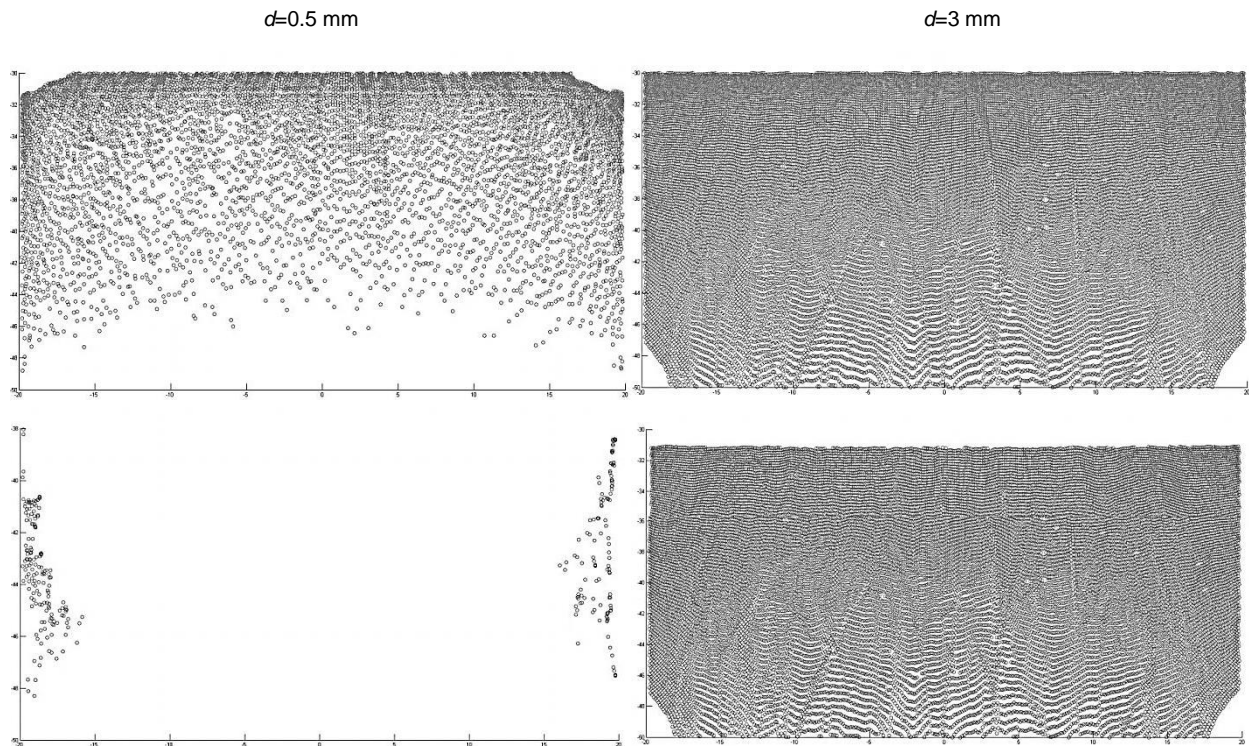


FIGURE 4.27 – DISTRIBUTION OF SMALL (LEFT) AND LARGE (RIGHT) RAINDROPS ON THE EAST FACADE OF THE CASSIER BUILDING WITHOUT (TOP) AND WITH (BOTTOM) THE 90 cm OVERHANG ($U_{10}=5$ m/s)

Generalization of the Results

Considering the scope of this study, it would be useful to provide generalized conclusions on the effectiveness of overhangs based on the examined cases. Nonetheless, the validity of such generalizations by, for instance, reporting the overhang width as its ratio to the height of the building is questionable. The substantial difference between the performance of the 90 cm overhang on the two buildings that have been studied here as well as the different facades of the Cassier building reveal the need for further investigation. The building geometry (most importantly, the ratio between its height and width) is known to have significant effects on the flow patterns [25]. Due to the differences in the structure of the flow around different buildings, a certain overhang would have different effects on the WDR wetting. This difference is obviously pronounced for the indirect effects of overhangs. Note how the windward facade of the cubic building and both North and East facades of the Cassier building are similarly protected from large ($d=3$ mm) raindrops by the 90 cm overhang, while this overhang has had very different impacts on the deposition of the small ($d=0.5$ mm) raindrops.

CHAPTER 5

Conclusions & Recommendations

As discussed in the review of the wind-driven rain (WDR) literature in Chapter 1, the effects of overhangs on the wind-driven rain wetting of building facades have not been studied in detail. To the knowledge of the author, this study has been the first of its kind. It has succeeded in revealing some of the effects of the influential factors, specifically, the overhang size and wind and rain conditions, on the performance of the overhang in protecting the facade from WDR loads. A new global measure is introduced to quantify the effects of overhangs. A fundamental understanding of the effects of overhangs on WDR wetting of the buildings is achieved on fluid mechanics grounds. In this closing chapter, the results of the study are summarized and concluded.

In the second part of this chapter, recommendations for the continuation of this study in the future are presented, so that general conclusions with a higher level of confidence can be made. The results of the current study, once supplemented by further investigations, could be used to develop practical principles regarding the design of effective roof overhangs.

5.1. Conclusions

The motivation behind this study has been the numerous cases of envelope failure in the coastal climate of British Columbia, Canada due to moisture loads and mainly WDR. Overhangs are a classical solution to the problem of extensive exposure of the facades to WDR. Nevertheless, their influence on WDR and how their performance is affected by different factors, such as size, wind speed and rainfall intensity, are not known to the designer. Despite the long history of research on wind-driven rain, at least to the knowledge of the author, the protective effects of overhangs against WDR had not been studied in detail. Understanding the effects of different overhangs on the wind-driven rain (WDR) loads on building facades under different wind and rain conditions has been the main purpose of this work.

Numerical simulation based on Computational Fluid Dynamics (CFD) has been used as the primary tool of investigation. The commercial CFD package ANSYS FLUENT is used to solve the wind flow around buildings using the realizable $k-\epsilon$ turbulence model and calculate the

raindrop trajectories. A MATLAB code has been developed to post-process the CFD results and calculate WDR parameters such as catch ratio. The numerical solution of the wind flow around the buildings and the computational code developed for the calculation of catch ratio are validated by comparison to previously published numerical studies and field measurements of wind-driven rain. These comparisons have shown the current results to be in good agreement with measurements as well as other numerical studies. Different sources of numerical and modeling errors are also discussed. Modeling errors associated with modeling the wind flow upstream of the building and turbulence have been the primary source of error in the simulations of the present study.

Two different buildings have been studied in this thesis. The first one is a low-rise cubic building. Results of various numerical tests on this building show that the presence of a roof overhang is, in general, effective in protecting the windward facade from exposure to WDR. The protection provided by the overhang increases as the overhang width increases. The influence of an overhang, nonetheless, varies under different wind and rain conditions and for different sizes of raindrops. All the examined overhangs have shown better performance, in terms of decreasing WDR loads on the facade, under low wind speeds. In one instance, under high wind speed, local adverse effects have been observed due to the presence of the overhang, *i.e.* the addition of the overhang has led to increased values of catch ratio (WDR exposure) at certain points. The relationship between the overhang performance and the wind angle varies with the location on the facade. Averaged over the whole facade, overhangs lead to larger relative reductions of WDR exposure under oblique winds. The performance of the overhang seems to be almost independent of the rainfall intensity as all the examined overhangs have more or less the same effectiveness under low, moderate, and high rainfall intensities.

The second building studied in this work is a mid-rise rectangular building. Comparison between the results of numerical tests on this building and the cubic building shows that the performance of the overhang is highly dependent upon the geometry of the building. Moreover, a certain overhang can have a different impact on different facades of the same building. For the rectangular building, a tested overhang has had clearly better performance in protecting the wider facade against WDR under similar wind and rain conditions. This dependency upon geometry has been attributed to the different flow structures that would form around different geometries, mainly the size of the wake past the roof and the facade edges.

In order to provide a fundamental understanding of the effects of the overhang on the WDR wetting of facades, two mechanisms are proposed. The overhang affects the deposition of raindrops on the facade by directly obstructing them as well as through the disturbance it would introduce to the wind flow upstream of the building. The latter is called the indirect effect. In the discussion of the results in Chapter 4, explanations of the different observations made from the results of the numerical tests have been given based on these two mechanisms. These mechanisms are shown to be capable of describing the effects of overhangs under different wind and rain conditions.

An effectiveness index is also introduced in order to provide a basis for quantifying the effects of overhangs. This index is calculated for different overhang widths and under different wind and rain conditions. When compared to the raindrop distribution graphs and catch ratio contours, this index appears consistent and seems to provide a meaningful measure of the effects of the overhang. By calculating the effectiveness index over different areas of the facade, it has also been shown that the protective effect of the overhang over the facade varies with position. Generally, upper portions of the facade, which suffer from higher intensities of WDR, are better protected by overhangs. The effectiveness of the overhang decreases when moving from the upper edge of the facade towards the ground.

5.2. Recommendations for Future Work

This study has been a first step in a network project with the final purpose of providing recommendations that would help the architect design effective overhangs. In order to achieve this goal, further examination of the involved variables is required. The suggestions made in this section for the continuation of the study include the cases and the variables that have not been examined in this work as well as different approaches to the problem. Each item is briefly discussed to show its significance.

5.2.1. Other Building Geometries

The focus of this work has been on a low-rise cubic building. The limited scenarios that have been examined for the mid-rise building reveal the need for further examination of mid- and high-rise buildings. The effects of building (and facade) geometry on the effectiveness of overhangs need to be studied in more depth.

5.2.2. Pitched Overhangs

All the cases studied in the present thesis include overhangs with zero pitch angles. It is, however, interesting from both practical and fundamental perspectives to examine the effects of pitched overhangs. The disturbance introduced to the upstream flow is suspected to be pronounced, and of course more complex, in the case of a pitched overhang.

5.2.3. Transient Wind and Rain

As mentioned in the previous section, all the cases presented in this work are under steady wind and rain conditions. A realistic estimation of the overall performance of an overhang cannot be made unless it is studied under realistic weather conditions, *i.e.* under varying wind and rain. Due to the complexity and high computational cost of a fully transient simulation of WDR, it is recommended to start with the pseudo-transient time averaging technique proposed by Blocken [10]. Transient simulations based on the a transient solution of the wind flow could be a next step.

5.2.4. Different Turbulence Models

The solution obtained for the wind flow field around the building is the most important element of the numerical simulation technique used in this work. It is known, from fluid mechanics and CFD experience, that such fine-scale geometric details as overhangs can have potentially significant influences that might be hard to capture in a numerical solution. Considering the recent advances in the non-RANS turbulence modeling techniques, such as Large Eddy Simulation (LES), as well as the growth of computational resources available to the researcher, numerical simulation of WDR based on improved turbulence models is becoming increasingly feasible.

5.2.5. Eulerian Tracking of the Raindrops

The most time-consuming part of the numerical simulation is the tracking of the raindrops in the Lagrangian framework. As discussed by Blocken et al. [47], and tested by Huang and Li [40], an Eulerian particle tracking technique along with non-RANS modeling of the turbulence can improve the accuracy of simulation in a computationally efficient way.

5.2.6. The WDR Database and Generalized Integrated Codes

As discussed by Blocken and Carmeliet [7] and reconfirmed by the present study, with the complexity of WDR and the various parameters involved on one hand, and the high computational cost of the simulations on the other hand, moving towards a comprehensive “WDR database” seems to be the best option at the moment. Developing generalized post-processing codes for determining raindrop and catch distributions on the facades, *optimization* of the computational codes to reduce computational effort, and integrating them into the current commercial CFD packages can significantly help the researcher build such a database.

APPENDIX A

Volume & Mass Fractions of WDR

As discussed in Chapter 2, the rainwater volume fraction in the air is the key factor that determines the *one-way coupling* regime of interaction between the raindrops and the wind. In this appendix, details of the calculation of this fraction are presented.

The WDR volume fraction is defined by Eq. (A.1) as

$$\Phi = \frac{\mathcal{V}_{wdr}}{\mathcal{V}_{air}} = \frac{1}{\mathcal{V}_{air}} \int_d \mathcal{V}(d) dd \quad (\text{A.1})$$

This relation can be rearranged as

$$\Phi = \int_d \mathcal{V}'(d) dd \quad (\text{A.2})$$

where $\mathcal{V}'(d)$ is the specific volume, *i.e.* the volume of the raindrop sizes with diameter d in a unit volume of air.

This specific volume can be calculated as

$$\mathcal{V}'(d) = N(d) \left(\frac{\pi d^3}{6} \right) \quad (\text{A.3})$$

with $N(d)$ being the specific number of raindrops with diameter d in unit volume of air.

$$N(d) = f(d)N \quad (\text{A.4})$$

In Eq. (A.4), N is the total number of raindrops in unit volume of air and f is the volume-based probability density function of the raindrops.

Based on an average spacing of 10 cm, as given by reference [49], N would be in the range of 860~1000. The limits are computed based on a homogenous distribution of raindrops with a minimum spacing of 10 cm in unit volumes of spherical and rectangular shape respectively.

Since both the size distribution and the spacing of raindrops are given for rectangular unit volumes of air, the upper limit of 1000, which is more conservative too, is used in the next steps.

Using Eqs. (A.2) to (A.4), the volume fraction Φ can be rewritten as

$$\Phi = \int_d N(d) \left(\frac{\pi d^3}{6} \right) dd = \int_d f(d) N \left(\frac{\pi d^3}{6} \right) dd \quad (\text{A.5})$$

Or

$$\Phi = \frac{\pi}{6} N \int_d f(d) (d^3) dd \quad (\text{A.6})$$

The probability density function f , which is the derivative of the cumulative density function given in reference [60], is a function a rainfall intensity, and of course raindrop diameter d

$$f(d) = \frac{d}{dd} \left[1 - \exp \left(- \left(\frac{d}{b} \right)^m \right) \right] \quad (\text{A.7})$$

where b is a constant and m is a function of the rainfall intensity. Thus, for fixed rainfall intensity, the expression on the RHS of Eq. (A.6) would be a simple integral over the range of raindrop diameters (0.3 – 6 mm).

For rainfall intensities from 1 mm/hr to 10 mm/hr, the volume fraction calculated from Eq. (A.6) will be in the $1.4\text{-}6.8 \times 10^{-6}$ range.

Once the volume fraction is known, the mass fraction α can be easily calculated by multiplying the volume fraction by the density ratio

$$\alpha = \frac{m_{wdr}}{m_{air}} = \frac{\rho_w \mathcal{V}_{wdr}}{\rho \mathcal{V}_{air}} = \frac{\rho_w}{\rho} \Phi \quad (\text{A.8})$$

Based on the calculated values of volume fraction, the mass fraction of WDR will be in the 1.13- 5.55×10^{-3} range for rainfall intensities of 1-10 mm/hr.

Thus, comparing the calculated volume and mass fractions to the limits given in reference [48] (see section 2.1), treating the wind-driven rain as a dilute discrete phase proves to be valid.

APPENDIX B

Number & Location of Particle Injections in Discrete Phase Modeling of Rain

The trajectories of the raindrops, consequently their distribution on the facade, and thus catch ratio values, are sensitive to the initial position in the computational domain from which the raindrops are released. In this appendix, the sensitivity of catch ratio values (the final output of the calculations) to the initial injection position of the raindrops is examined.

Numerical tests have revealed that local values of catch ratio are sensitive to the initial conditions of the raindrops, *i.e.* their injection positions. The initial injection position is expected not to affect the particle trajectories significantly. Nonetheless, a change in the trajectory of a raindrop, however small, can change its *final destination*, *i.e.* whether it hits the facade at all or not. The sensitivity to initial conditions is pronounced for small raindrops and around edges and corners.

As mentioned in section 2.3, the injection planes for each raindrop size are determined under each wind angle and speed by trial and error so that the windward facade of the building (without an overhang) is fully covered by the raindrops. However, the spacing of the raindrops within that plane, or, equivalently, their initial coordinates, can vary when different total numbers of raindrops are released from the plane. Although there are experimental measurements of the average spacing between the raindrops in actual rainfalls, for instance reference [49], these values are appropriate not for WDR simulations in general. The measurements are performed for horizontal rainfalls, *i.e.* in the absence of significant *sweeping* of the raindrops by wind. Moreover, these measured values could be too large to provide catch ratio results with desired resolutions. Applying such mean values to all the raindrops and at different altitudes could be questionable too.

Through a perturbation study, it is shown that, despite the sensitivity of the local catch ratio values to the initial conditions, the overall distribution of catch ratio on the facade (the wetting pattern) remains more or less the same with initial conditions slightly changed. In the first part of this study, catch ratio values on the windward facade of the cubic building were calculated with

the number and the initial positions of the raindrops slightly perturbed. Wind and rain conditions were fixed for all the cases. Figure B1 shows the value of catch ratio at the center of the cubic building (2m×2m cell) calculated with different numbers of raindrops injected from the same planes. Further numerical tests show that the variation of the catch ratio with the number of injected raindrops is close to *asymptotic* convergence behavior.

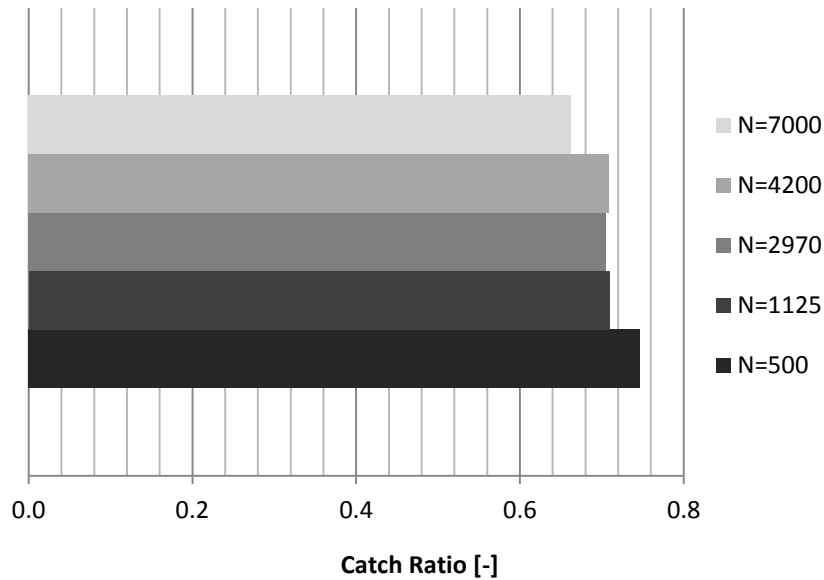


FIGURE B1 - VARIATION OF CATCH RATIO AT THE CENTER OF THE CUBIC BUILDING WITH DIFFERENT NUMBERS OF INJECTED RAINDROPS ($\theta=0^\circ$, $U_{10}=10$ m/s, $R_h=5$ mm/hr)

In the second part, with the total number of the injected raindrops fixed, the whole injection plane was slightly perturbed. The effects of this perturbation on both specific and total catch ratios have been examined. Figures B2 and B3 show the variation of the specific catch ratio for small and large raindrops ($d=0.5$ mm and 3 mm respectively) after the injection planes was translated +10 cm in the z-direction. Specific catch ratio values are reported at the top center (1,3), top corner (1,5) and the center (3,3) points of the windward facade of the cubic building. As clearly seen in these graphs, the small raindrops are more sensitive to the initial conditions.

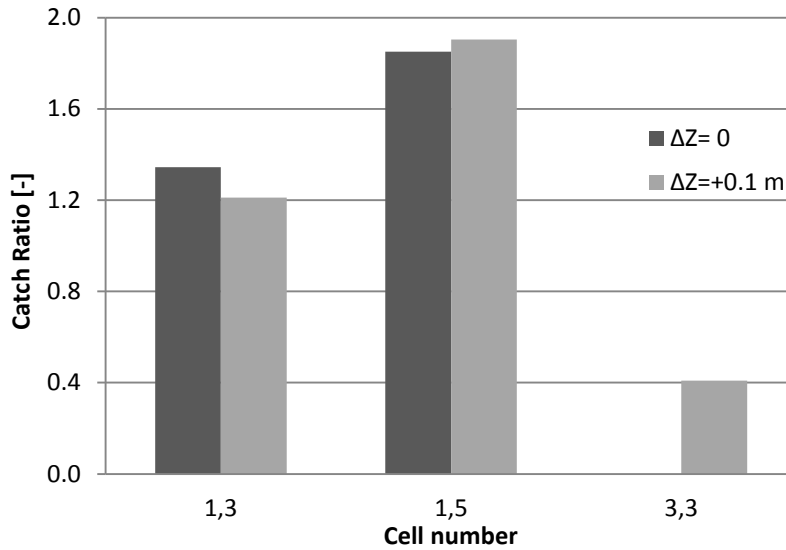


FIGURE B2 – SPECIFIC CATCH RATIO ($d=0.5$ mm) VALUES AT DIFFERENT LOCATIONS WITH 10 cm PERTURBATION OF THE INJECTION PLANE IN THE z-DIRECTION ($\theta=0^\circ$, $U_{10}=10$ m/s)

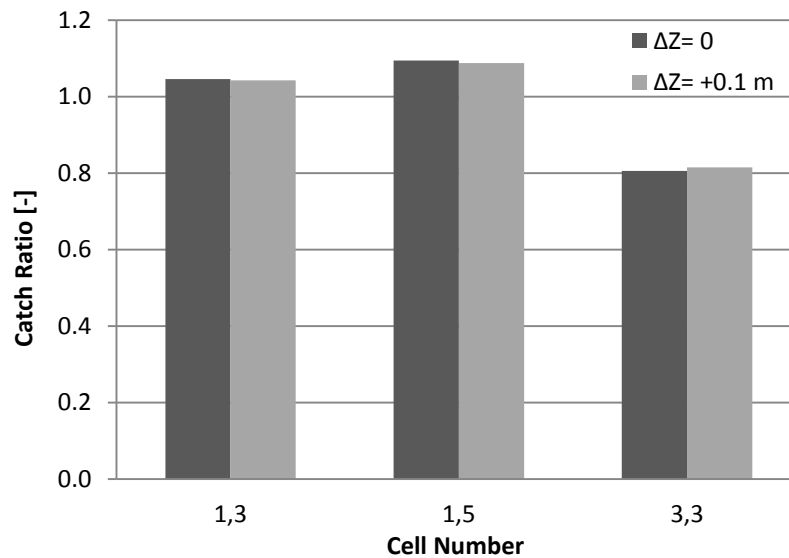


FIGURE B3 – SPECIFIC CATCH RATIO ($d=3$ mm) VALUES AT DIFFERENT LOCATIONS WITH 10 cm PERTURBATION OF THE INJECTION PLANE IN THE z-DIRECTION ($\theta=0^\circ$, $U_{10}=10$ m/s)

In Fig. B4, total catch ratio values at the center of the facade are shown under three rainfall intensities and with a +10 cm perturbation of the injection plane. It can be seen that under low rainfall intensities (*e.g.* $R_h=2$ mm/hr) the sensitivity to the initial conditions is pronounced.

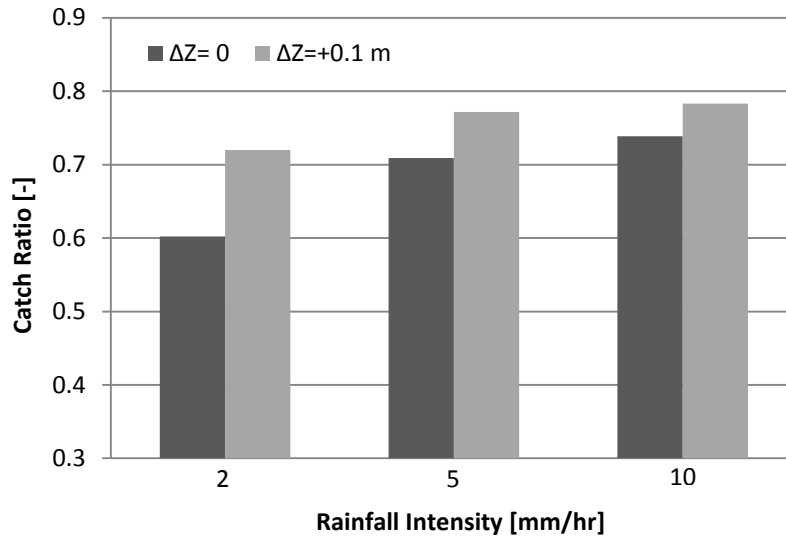


FIGURE B4 - CATCH RATIO (CENTER) vs. RAINFALL INTENSITY WITH 10 cm PERTURBATION OF THE INJECTION PLANE IN THE z-DIRECTION ($\theta=0^\circ$, $U_{10}=10$ m/s)

Numerical tests show that the effects of a perturbation of the injection plane (with fixed number of injection points) on the catch ratio values varies with the cell size too. For instance, a 5 cm perturbation of the injection plane in the z-direction, leads to average changes of -13%, -2% and 1% in the total catch ratio values over the whole facade when calculations are done over $0.1\text{m}\times 0.1\text{m}$, $0.2\text{m}\times 0.2\text{m}$ and $0.25\text{m}\times 0.25\text{m}$ cells respectively.

Therefore, spacing of the raindrops on the injection plane should be also proportional to the size of the cells on the facade. If higher resolution results are desired, raindrops must be injected with finer spacing on the injection plane. It is deduced from many trial-and-error-based examinations that, to obtain reasonable results, the cell size, on average, should be at least twice the spacing between injection points.

On the other hand, there is an *upper limit* for this sensitivity. If the number of raindrops is sufficient to correctly form the largest possible *convex hull*, or equivalently *streamtube* (see section 2.4), for each cell, further increasing the injected raindrops should not affect the catch ratio results. The additional raindrops would move within the same streamtubes and, thus, create the same *wetted areas*. Figure B5 shows the 0.5 mm raindrops ending up in an arbitrary cell, with the injection spacing decreased by factors of 2.1, 1.14 and 1.2 in each two successive steps

(from left to right). Note how the area of the convex hull (the circumscribing polygon containing all the raindrops) remains almost unchanged after the first refinement.

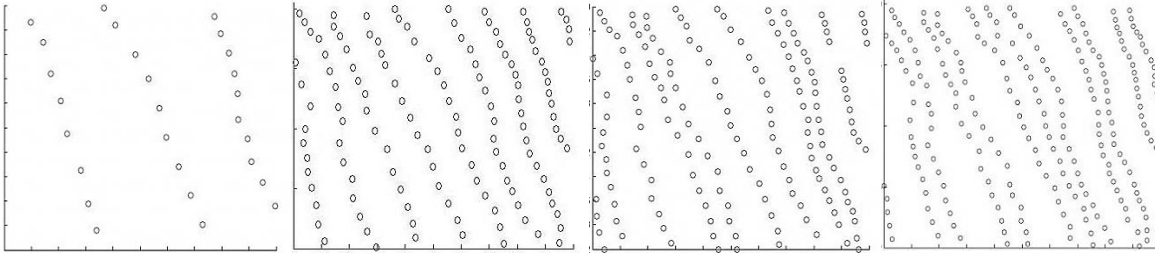


**FIGURE B5 – 0.5 mm RAINDROPS IN A CELL ON THE FACADE, INJECTED AT DIFFERENT SPACINGS
(REFINEMENT FACTOR FROM LEFT TO RIGHT: 2.1, 1.14 & 1.2)**

As a final remark, it is worth mentioning that due to technical programming reasons, and in favour of computational time, the same total number of injected raindrops is used for all the raindrop diameters. However, the injection plane that would lead to a complete coverage of the facade will vary in size from raindrop to raindrop and, therefore, the injection spacing will not be the same for all the raindrops. Based on perturbation studies with total catch ratio as the monitored output, a total number of 8500 raindrops is used for the cubic building. For the Cassier building, 15000 and 40000 raindrops are injected to cover North and East facades respectively.

APPENDIX C

Details of the Validation Study Based on Field Measurements

In this appendix, details of the validation study presented in Chapter 3 are discussed. This study has been performed based on a large set of field measurement data on a test building in Vancouver, Canada from 2007-2009 [64]. The experimental data include wind speed, wind angle and horizontal rainfall intensity from a weather station on the roof and the amount of driving rain on the east facade of the building. The data are recorded at a 5 minute time step. Figure C1 shows a side view of the test building. The arrangement of WDR gauges on the facades of this building is shown in Fig. C2.



FIGURE C1 – THE SOUTH AND EAST FACADES OF THE TEST BUILDING (CASSIER) [64]

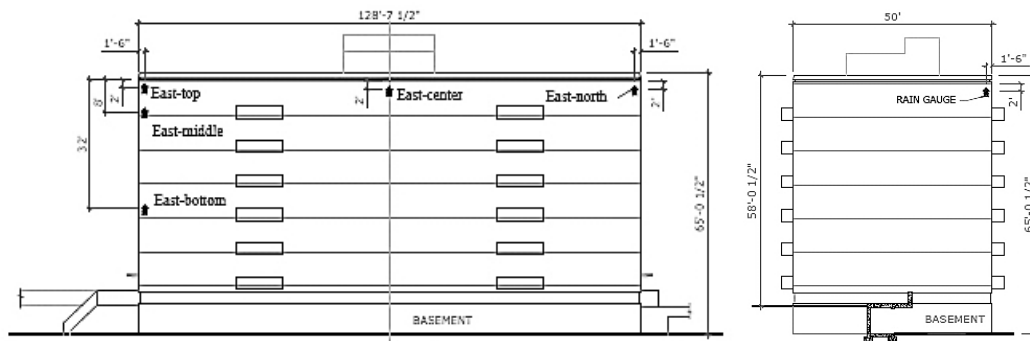


FIGURE C2 - WDR GAUGES ON THE TEST BUILDING
LEFT: EAST FACADE, RIGHT: NORTH FACADE [64]

All the numerical simulations of this work are performed in steady state. However, due to the highly fluctuating nature of wind, it is difficult to find a period of a few hours of relatively steady wind (speed and angle) within the measured data. To find such a period, 5 minute data are first averaged and converted to hourly data. In this manner, the rainwater accumulation data (S_h) [mm] are also converted into rainfall intensity [mm/hr]. Afterwards, a MATLAB code, developed for this purpose, searches the hourly data to find a number of successive hours with wind angles within a specified tolerance of the desired value, *e.g.* $90^\circ \pm 15^\circ$. Wind speed and rainfall intensity (horizontal and WDR) are then averaged using the technique proposed by Blocken [10]. In this technique, meteorological data are time-averaged with the accumulated rainwater as the weighting function. Hence, the averaged wind speed (\bar{U}) and horizontal rainfall intensity (\bar{R}_h) are calculated as

$$\bar{U} = \frac{\sum_i U_i S_{hi}}{\sum_i S_{hi}} \quad (C.1)$$

And

$$\bar{R}_h = \frac{\sum_i R_{hi} S_{hi}}{\sum_i S_{hi}} \quad (C.2)$$

where S_{hi} , R_{hi} and U_i are the horizontal rainwater, horizontal rainfall intensity and wind speed respectively, recorded at the time step i .

Blocken discusses the need to average measured data to periods longer than a few minutes, mentioning that “meteorological data, especially in building physics, are usually provided on an hourly basis” [10]. In the same reference, he has first shown that a time step of 10 minutes would lead to “time representative” (catch ratio) results. Then, he shows that catch ratio results calculated based on averaged wind and rain conditions are in a good agreement with the averaged catch ratio results computed based on high resolution (small time step) wind and rain data. Blocken has shown that this close agreement is achieved when the weighted averaging performed with the horizontal rainfall (not the *intensity*) as the weighting function for both wind speed and rainfall intensity.

It is noteworthy, however, that this discussion is based on the assumption that the relation between catch ratio and rainfall intensity and wind speed is linear. Blocken himself has argued that where the nonlinearity of this dependency is pronounced, *e.g.* for regions protected by roof overhangs, the representative character of this averaging technique must be further examined. The other circumstance under which the assumption linear relationship is not quite valid, as stated in reference [10], is under low rainfall intensities. (Note that in a low intensity rainfall, the majority of the raindrops are small drag-driven ones that are highly affected by the local features of turbulence).

The selected 6 hour period (from November 2008 data) and the averaged wind speed and rainfall intensity values calculated based on the method discussed above are summarized in Table C1.

**TABLE C1 – HOURLY AVERAGED WIND AND RAIN DATA USED IN THE VALIDATION STUDY
(RAW DATA FROM REFERENCE [64])**

Hour	Wind Angle θ [°]	Wind Speed U [m/s]	Horizontal Rainfall Intensity R_h [mm/hr]
1	91	1.67	0.0
2	88	3.27	1.7
3	101	7.29	3.5
4	82	5.16	2.1
5	90	4.48	0.6
6	100	2.78	1.1
Average	93	5.29	2.3

Wind angle is measured clockwise with 0 as normal to the North facade, *i.e.* a 90° wind angle corresponds to wind approaching normal to the East facade. Wind speed is measured by a wind mast located on the roof, almost 25.3 m above the ground.

Table C2 shows catch ratio values based on the WDR gauge readings in the same period of six hours. These values are calculated directly from the rainwater accumulation data from the WDR gauges.

To validate the used numerical scheme, catch ratio values at the same locations as the three WDR gauges mentioned in Table C2 are calculated under the average wind and rainfall conditions corresponding to this period. The building is modeled in full scale as a simple

rectangle, without the design details such as balconies and windows. For a schematic of the computational domain, see Fig. 2.2 on page 31.

**TABLE C2 – CATCH RATIO VALUES CALCULATED
BASED ON FIELD MEASUREMENTS (CASSIER BUILDING)**

Gauge		Average WDR Intensity [mm/hr]	Catch Ratio
Location	Number		
East-top	1	1.3	0.57
East-middle	2	0.8	0.37
East-bottom	3	0.5	0.21

The boundary conditions are the same as the ones discussed in Chapter 2. For the inlet velocity profile, an exponent of $\alpha_p=0.25$ is chosen to represent moderate obstruction in the neighbourhood of the building. U_H is adjusted by trial and error so that the same speed as the average of the measurements (see Table C1) is reproduced at the tip of the wind mast. The roughness height of the bottom of the domain (ground) is set as $K_S=1$ m to represent the surrounding terrain of an urban area [56]. Tables C3 and C4 have the information concerning the computational domain and the boundary conditions used in this validation study.

**TABLE C3 – COMPUTATIONAL DOMAIN SIZE & DISCRETIZATION
FOR THE CASSIER BUILDING**

Domain Length (x)		430 m	
Domain height (y)		100 m	
Domain Width (z)		190 m	
Surface Mesh	Size	Domain sides	3 m
		Building walls	0.15 m
	Type	Quadrangle	
Volume Mesh	Number of CV's	$\sim 1.67 \times 10^6$	
	Type	Tetrahedral	

**TABLE C4 – SUMMARY OF BOUNDARY CONDITIONS
FOR THE CASSIER BUILDING**

Boundary	Condition		
	Momentum	Turbulence	DPM
Inlet	<i>Direction:</i> Normal to boundary <i>Magnitude:</i> [Eq.(2.4)] $U_{10}= 4.5 \text{ m/s}, \alpha_p = 0.25$	k : Eq. (2.5) ε : Eq. (2.6)	-
Sides	Symmetry		-
Top	Symmetry		-
Bottom	No slip, impermeable	Roughness height $K_s=1 \text{ m}$	Trap
Outlet	Backflow pressure ($p_0=0$, gauge)	$k_{\text{backflow}}=1 \text{ m}^2/\text{s}^2$ $\varepsilon_{\text{backflow}}=1 \text{ m}^2/\text{s}^3$	-
Building	No slip, impermeable	Roughness height $K_s=0$	Trap

To save computational time and effort, the raindrop diameter spectrum is divided to 8 segments only (0.3, 0.9, 1.4, 1.8, 2.6, 3.8, 4.8 and 5.8 mm raindrops). However, considering all the other uncertainties associated with both the measurements and the numerical simulation, the catch ratio results predicted by numerical simulation based on CFD are in very good agreement as discussed in Chapter 3.

REFERENCES

- [1] Hazleden, D. G., and Morris, P.I., 1999, “Designing for durable wood construction: The 4 Ds”, *8th International Conference on Durability of Building Materials and Components*.
- [2] Morrison Hershfield, 1996, “Survey of building envelope failures in the coastal climate of British Columbia”, Canadian Mortgage and Housing Corporation, Ottawa.
- [3] Morris, P.I., 2006, “Damp coastal weather field issues and improving performance”, *Wood Protection 2006*.
- [4] Karagiozis, A., and Salonvaara, M., 2001, “Hygrothermal system-performance of a whole building”, *Building and Environment*, **36**(6), pp. 779-787.
- [5] Karagiozis, A., and Desjarlais, A., 2000, “Integrated Hygrothermal Performance of Building Envelopes and Systems in Hot and Humid Climates”, *Symposium on Improving Building Systems in Hot and Humid Climates*.
- [6] Straube, J., and Burnett, E., 2001, “Overview of Hygrothermal (HAM) Analysis Methods”, ASTM MNL40: Moisture analysis and condensation control in building envelopes, Chapter 5.
- [7] Blocken, B., and Carmeliet, J., 2004, “A Review of Wind-Driven Rain Research In Building Science”, *Journal of Wind Engineering and Industrial Aerodynamics*, **92**(13), pp. 1079-1130.
- [8] Blocken, B., and Carmeliet, J., 2007, “Validation of CFD simulations of wind-driven rain on a low-rise building facade”, *Building and Environment*, **42**(7), pp. 2530-2548.
- [9] Blocken, B., and Carmeliet, J., 2006, “On the Accuracy of Wind-Driven Rain Measurements on Buildings”, *Building and Environment*, **41**(12), pp. 1798-1810.
- [10] Blocken, B., 2004, “Wind-driven rain on Buildings”, Ph.D. Thesis, *Katholieke Universiteit Leuven*, Leuven, Belgium.

- [11] Lacy, R.E., 1965, “Driving-Rain Maps and the Onslaught of Rain on Buildings”, *Proceedings of RILEM/CIB Symposium on Moisture Problems in Buildings*, Helsinki.
- [13] Straube, J. F., 1998, “Moisture Control and Enclosure Wall Systems”, PhD Thesis, *University of Waterloo*, Waterloo, ON, Canada.
- [13] Kumaraperumal, A., Sanders, C.H., Baker, P.H., and Galbraith, G.H., and Don McGlinchey, 2007, “Analyzing Wind-Driven Rain on a Building Facade Using The Laser Precipitation Monitor (LPM)”, *The 6th International Conference on Indoor Air Quality, Ventilation & Energy Conservation in Buildings (IAQVEC 2007)*, Oct. 28 - 31 2007, Sendai, Japan
- [14] Flower, J.W., Lawson, T.V., 1972, “On the laboratory representation of rain impingement on buildings”, *Atmospheric Environment*, **6**, pp. 55–60.
- [15] Rayment, R., Hilton, M., 1977, “The use of bubbles in a wind tunnel for flow-visualisation and the possible representation of raindrops”, *Journal of Industrial Aerodynamics*, **2**, 149–157.
- [16] Surry, D., Inculet, D. R., Skerlj, P. F., Lin, J.-X., and Davenport, A. G., 1994, “Wind, rain and the building envelope: a status report of ongoing research at the University of Western Ontario”, *Journal of Wind Engineering and Industrial Aerodynamics*, **53**(1-2), pp. 19-36.
- [17] Hoppestad, S., 1955, “*Slagregn i Norge*” (in Norwegian), Rapport No. 13, Norwegian Building Research Institute, Oslo.
- [18] Rodgers, G.G, Poots, G, Page, J.K., Pickering, W.M., 1974, “Theoretical Predictions of Raindrop Impaction on a Slab Type Building”, *Building Science*, **9**, pp. 181-190.
- [19] Choi, E.C.C., 1991, “Numerical Simulation Of Wind-Driven-Rain Falling Onto A 2-D Building”, *Asia Pacific Conference on Computational Mechanics, Hong Kong*, pp. 1721–1728.
- [20] Choi, E.C.C., 1993, “Simulation of Wind-Driven-Rain around A Building”, *Journal of Wind Engineering and Industrial Aerodynamics*, **46-47**, pp. 721-729.

- [21] Choi, E.C.C., 1994, “Determination of wind-driven-rain intensity on building faces”, *Journal of Wind Engineering and Industrial Aerodynamics*, **51**(1), pp. 55-69.
- [22] Choi, E.C.C., 1997, “Numerical modeling of gust effect on wind-driven rain”, *Journal of Wind Engineering and Industrial Aerodynamics*, **72**, pp. 107–116.
- [23] Choi, E.C.C., 1999, “Wind-driven rain on building faces and the driving-rain index”, *Journal of Wind Engineering and Industrial Aerodynamics*, **79**(1-2), pp. 105-122.
- [24] Hangan, H., 1999, “Wind-driven rain studies. A C-FD-E approach”, *Journal of Wind Engineering and Industrial Aerodynamics*, **81**(1-3), pp. 323-331.
- [25] “2009 ASHRAE Handbook – Fundamentals (I-P Edition)”, 2009, American Society of Heating, Refrigerating and Air-Conditioning Engineers Inc., Chap. 24.
- [26] Blocken, B., and Carmeliet, J., 2000, “Driving Rain on Building Envelopes—I: Numerical Estimation and Full-Scale Experimental Verification”, *Journal of Thermal Envelope and Building Science*, **24**(1), pp. 61–85.
- [27] Blocken B., and Carmeliet J., 2000, “Driving Rain on Building Envelopes—II: Representative Experimental Data For Driving Rain Estimation”, *Journal of Thermal Envelope and Building Science*, **24**(2), pp. 89–110.
- [28] Choi, E.C.C., 2001, “Wind-driven rain and driving rain coefficient during thunderstorms and non-thunderstorms”, *Journal of Wind Engineering and Industrial Aerodynamics*, **89**, pp. 293-308.
- [29] Blocken, B., and Carmeliet, J., 2002, “Spatial and temporal distribution of driving rain on a low-rise building”, *Civil Engineering*, **5**(5), pp. 441-462.
- [30] Blocken, B., and Carmeliet, J., 2005, “Computational Fluid Dynamics simulations of wind-driven rain on a low-rise building : new validation efforts,” *Proceedings of the 7th Symposium on Building Physics in the Nordic Countries*, pp. 428-435.

- [31] Blocken, B., and Carmeliet, J., 2006, “On the validity of the cosine projection in wind-driven rain calculations on buildings”, *Building and Environment*, **41**(9), pp. 1182-1189.
- [32] Blocken, B., and Carmeliet, J., 2007, “Validation of CFD Simulations of Wind-Driven Rain On A Low-Rise Building Facade”, *Building and Environment*, **42**(7), pp. 2530–2548.
- [33] Abadie, M. O., and Mendes, N., 2008, “Numerical assessment of turbulence effect on the evaluation of wind-driven rain specific catch ratio”, *International Communications in Heat and Mass Transfer*, **35**(10), pp. 1253-1261.
- [34] Abuku, M., Blocken, B., Nore, K., Thue, J. V., Carmeliet J., and Roels S., 2009, “On the validity of numerical wind-driven rain simulation on a rectangular low-rise building under various oblique winds”, *Building and Environment*, **44**(3), pp. 621-632.
- [35] Abuku, M., Blocken, B., and Roels S., 2009, “Field measurement and numerical analysis of wind-driven rain absorption and evaporation on building facades”, 5th *European-African Conference on Wind Engineering*, Florence, Italy.
- [36] Blocken, B., Defraeye, T., Derome, D., and Carmeliet J., 2009, “High-resolution CFD simulations for forced convective heat transfer coefficients at the facade of a low-rise building”, *Building and Environment*, **44**, pp. 2396-2412.
- [37] Briggen, P. M., Blocken, B., and Schellen, H. L., 2009, “Wind-driven rain on the facade of a monumental tower: Numerical simulation, full-scale validation and sensitivity analysis”, *Building and Environment*, **44**(8), pp. 1675-1690.
- [38] Blocken, B., Stathopoulos, T., Carmeliet, J., and Hensen, J.L.M., 2009, “Application of CFD in building performance simulation for the outdoor environment”, 11th *International Building Performance Simulation Association Conference*, Glasgow, Scotland, pp. 489-496.
- [39] Blocken, B., Dezsö, G., Beeck, J. V., and Carmeliet, J., 2009, “The mutual influence of two buildings on their wind-driven rain exposure and comments on the obstruction factor,” *Journal of Wind Engineering*, **31**(1999), pp. 1-21.

- [40] Huang, S.H., and Li, Q. S., 2010, “Numerical Simulations Of Wind-Driven Rain On Building Envelopes Based On Eulerian Multiphase Model”, *Journal of Wind Engineering and Industrial Aerodynamics*, **98**(12), pp. 843-857.
- [41] Blocken, B., Carmeliet J., 2005, “High-resolution wind-driven rain measurements on a low-rise building—experimental data for model development and model validation”, *Journal of Wind Engineering and Industrial Aerodynamics*, **93**(12), 905–928.
- [42] Blocken, B., Dezsö, G., van Beeck, J., and Carmeliet, J., 2010, “Comparison of calculation models for wind-driven rain deposition on building facades”, *Atmospheric Environment*, **44**(14), pp. 1714-1725.
- [43] “Hygrothermal performance of buildings – Calculation and presentation of climatic data – Part 3: Calculation of a driving rain index for vertical surfaces from hourly wind and rain data”, 2009, ISO 15927-3.
- [44] Straube, J.F., Burnett, E.F.P., 2000, “Simplified prediction of driving rain on buildings, *Proceedings of the International Building Physics Conference*, Eindhoven, The Netherlands, pp. 375–382.
- [45] Blocken, B., and Carmeliet, J., 2010, “Overview of three state-of-the-art wind-driven rain assessment models and comparison based on model theory”, *Building and Environment*, **45**(3), pp. 691-703.
- [46] van Hooff, T., Blocken, B., and van Harten, M., 2011, “3D CFD simulations of wind flow and wind-driven rain shelter in sports stadia: Influence of stadium geometry”, *Building and Environment*, **46**(1), pp. 22-37.
- [47] Blocken, B., Abuku, M., Nore, K., Briggen, P. M., Schellen, H. L., Thue, J. V., Roels, S., and Carmeliet, J., 2011, “Intercomparison of wind-driven rain deposition models based on two case studies with full-scale measurements”, *Journal of Wind Engineering and Industrial Aerodynamics*, **99**(4), pp. 448-459.

- [48] Elghobashi, S., 1994, “On predicting particle-laden turbulent flows”, *Applied Scientific Research*, **52** (4), pp. 309-329
- [49] Lovejoy, S., and Lilley, M., Desaulniers-Soucy, N., and Schertzer, D., 2003, “Large particle number limit in rain”, *Physical Review*, **68**, 25301.
- [50] Csanady, G. T., 1963, “Turbulent Diffusion of Heavy Particles in the Atmosphere”, *Journal of Atmospheric Science*, **20**, 201–208.
- [51] Wilcox, D. C., 1994, “Turbulence Modeling for CFD”, DCW Industries, California ISBN 0-9636051-0-0
- [52] Jimenez, J., 2004, “Turbulence and Vortex Dynamics”, Lecture notes, Stanford University.
- [53] “FLUENT® 6.2 Tutorial Guide”, 2005, FLUENT Inc.
- [54] Shih, T.-H, Liou, W. W., Shabbir, A., Yang, Z., and Zhu. J., 1995, “A New k- ϵ Eddy-Viscosity Model for High Reynolds Number Turbulent Flows - Model Development and Validation”, *Computers & Fluids*, **24**(3), pp. 227-238.
- [55] Hansen, F.V., 1993, “Surface Roughness Lengths”, Report No. ALR-TR-61, Army Research Laboratory, Adelphi, Maryland, USA.
- [56] Wieringa, J., Davenport, A.G., Grimmond, C.S.B., and Oke, T. R., 2001, “New Revision of Davenport Roughness Classification”, *The 3rd European and African Conference on Wind Engineering*, Eindhoven, The Netherlands.
- [57] Gunn, R., and Kinzer, G. D., 1949, “The Terminal Velocity of Fall for Water Droplets in Stagnant Air”, *Journal of Atmospheric Sciences*, **6**(4), pp. 243-248.
- [58] Beard, K. V., Bringi, V. N., and Thurai, M., 2010, “A new understanding of raindrop shape”, *Atmospheric Research*, **97**(4), pp. 396-415.
- [59] Morsi, S. A., and Alexander, A. J., 1972, “An investigation of particle trajectories in two-phase flow systems”, *Journal of Fluid Mechanics*, **55** , pp. 193-208.

- [60] Best, A. C., 1950, “The Size Distribution of Raindrops”, *Quarterly Journal of the Royal Meteorological Society*, **76**(327), pp. 16–36.
- [61] de Berg, M., Cheong, O., van Kreveld, M., and Overmars, M., 2008, “*Computational Geometry; Algorithms and Applications* (3rd Ed.)”, Springer-Verlag, Heidelberg, Chaps. 1 & 11.
- [62] Roy, C.J., 2004, “Verification of Codes and Solutions in Computational Simulation”, *ICHMT International Symposium on Advances in Computational Heat Transfer*, Norway.
- [63] “ANSYS Fluid Dynamics Verification Manual”, 2011, ANSYS Inc.
- [64] Ge, H., and Krpan, R., 2009, “Wind-driven Rain Study in the Coastal Climate of British Columbia”, Final Report, Prepared for Homeowner Protection Office, BC.
- [65] Richardson, L. F., 1910, “The Approximate Arithmetical Solution by Finite Differences of Physical Problems Involving Differential Equations, With an Application to the Stresses in a Masonary Dam”, *Philosophical Transactions of the Royal Society, Ser. A*, **210**, pp. 307–357.
- [66] “Procedure for Estimation and Reporting of Uncertainty Due to Discretization in CFD Applications” [Announcement], 2008, *Journal of Fluids Engineering*, **130**(7).
- [67] Roache, P. J., 1994, “Perspective: A Method for Uniform Reporting of Grid Refinement Studies”, *Journal of Fluids Engineering*, **116**, pp. 405-413.
- [68] Blocken, B., Stathopoulos, T., and Carmeliet, J., 2007, “CFD simulation of the atmospheric boundary layer: wall function problems”, *Atmospheric Environment*, **41**(2), pp. 238-252.
- [69] “SigmaPlot® 10 User’s Manual”, 2006, Systat Software Inc.
- [70] Mohaddes Foroushani, S.S., Naylor, D., and Ge, H., 2012, “Numerical Investigation of the Effects of Different Overhang Configurations on the Wind-Driven Rain Wetting of Building Facades”, *Proceedings of ASME 2012 International Mechanical Engineering Congress & Exposition (IMECE2012)*, Houston, USA.